SISSA

INTERNATIONAL SCHOOL FOR ADVANCED STUDIES

---

PHD COURSE IN THEORY AND NUMERICAL SIMULATION OF CONDENSED MATTER

# TRANSIENT DYNAMICS OF UNCONVENTIONAL SUPERCONDUCTORS

## d-WAVE SYMMETRY AND STRONG CORRELATIONS


THESIS SUBMITTED FOR THE DEGREE OF

*Doctor Philosophiae*

CANDIDATE:
Francesco Peronaci

SUPERVISOR:
Prof. Massimo Capone

---

ACADEMIC YEAR 2015 – 2016

# CONTENTS

# ABSTRACT

This thesis is about unconventional superconductors out of equilibrium. More precisely, it summarizes our theoretical efforts in addressing a few questions related to the real-time evolution in models displaying unconventional superconductivity.

Apart from the purely theoretical interest, the motivation for these studies comes from the recent achievement in the field of ultrafast time-resolved spectroscopy on correlated materials, such as the high-temperature copper-oxide superconductors. The task of describing such systems in nonequilibrium is a very difficult one. In this thesis we attack the problem from two different points of view:

- the anisotropic unconventional d-wave symmetry,
- the strong electron-electron correlations.

The thesis is organized as follows:

The first part introduces the basic concepts which lay at the foundation of the work presented in the other two parts. In Chapter 1, the concept of unconventional superconductivity is briefly introduced. This mainly includes the high-temperature copper-oxide superconductors and their phenomenology: d-wave symmetry of the superconducting gap and strong electron-electron interaction. Chapter 2 is devoted to a review of the recent experimental advances in the field of ultrafast spectroscopy of high temperature superconductors and correlated materials, with a particular focus on time- and angle-resolved photoemission spectroscopy. Finally, Chapter 3 is a short review of some works in the field of cold-atom Fermi gases.

In the second part we address the physics of the d-wave superconductor after a sudden excitation. First, in Chapter 4 we introduce in some detail a model of mean-field superconductor with a d-wave symmetry. The principal feature of this model is the anisotropy of the gap and the *nodal lines* along which the gap vanishes. The results concerning the dynamics of the gap after a "quantum quench" are exposed in Chapter 5 where we compare our model to the s-wave superconductor. This comparison allows to identify the consequences of the unconventional symmetry. In Chapter 6 we discuss the spectral features of the transient nonequilibrium state of the d-wave superconductor. This is particularly important to move a first step towards photoemission experiments.

In the third part we concentrate on the attractive Hubbard model as a prototype of strongly correlated superconductor. In Chapter 8 we discuss the superconducting state at equilibrium with the use of dynamical mean-field theory. In Chapter 9 we discuss the extension

of this technique to systems out of equilibrium. In particular it is described the implementation in the superconducting phase.

At the end of the thesis two appendices give some details of the calculations.

# Part I

# INTRODUCTION

# 1 UNCONVENTIONAL SUPERCONDUCTORS

Superconductivity is a quantum phase of matter characterized by zero electrical resistance and perfect diamagnetism [1]. It was first observed in 1911 by Kamerling Onnes and since then many materials were found to superconduct below some critical temperature $T_c$. Until 1986 superconductivity was however limited to elemental metals and binary alloys with critical temperatures which could hardly exceed a few K. The discovery by Bednorz and Müller [2] of superconductivity in doped Mott insulators changed completely the field, not only because of the significantly larger critical temperatures, but also because the strong correlation effects of the high-$T_c$ superconductors lead to remarkably new properties including the d-wave symmetry of the order parameter, which features lines with gapless excitations. The landscape of superconducting materials then extended in different directions, including alkali-metal doped fullerides, $MgB_2$, iron pnictides and chalcogenides and pressurized sulfur hydrides.

This evolution of the field led to a conceptual dualism between *conventional* and *unconventional* superconductivity, with the former defined essentially by the possibility to explain it in terms of the Bardeen-Cooper-Schrieffer (BCS) theory.

In this chapter we discuss the main aspects of unconventional superconductors. Emphasis is put on the high temperature copper-oxide superconductors, in particular on those characteristics – d-wave symmetry and strong correlations – which are the subject of the thesis.

## 1.1 CONVENTIONAL AND UNCONVENTIONAL SUPERCONDUCTORS

The first satisfactory theory of superconductivity was formulated by Bardeen, Cooper and Schrieffer in 1957 [3]. The BCS theory is based on the intuitively surprising fact that, despite the Coulomb repulsion, two electrons in a solid may experience a net mutual attraction. This attractive interaction is mediated by the oscillations of the underlying lattice of positively charged ions and is therefore retarded, as opposed to the non-relativistic instantaneous Coulomb repulsion which is considered in the solid state context.

A fundamental result due to Cooper [4] is that, for a metal with a finite density and in three dimensions, no matter the strength of this net attraction, two electrons form a singlet bound state which is known as a *Cooper pair*. The superconducting phase of matter than emerges when a macroscopic number of Cooper pairs form a single

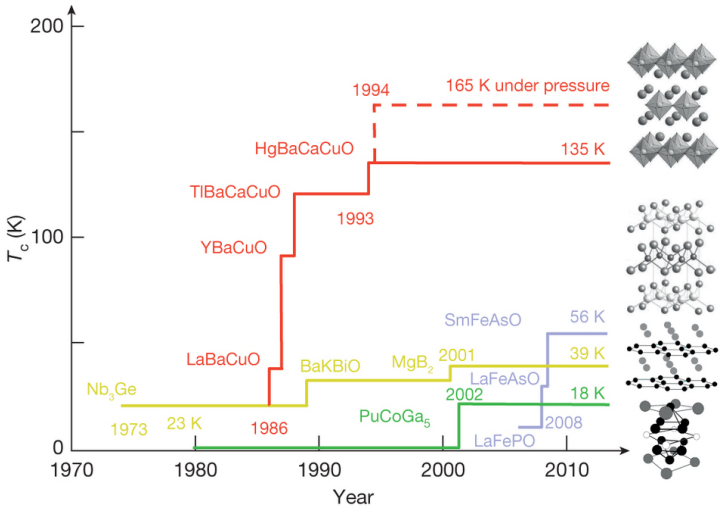


Figure 1: Superconducting transition temperatures versus year of discovery for various classes of superconductors. The images on the right are the crystal structures of representative materials. The established record for conventional electron–phonon superconductors (yellow) is 39 K in $MgB_2$. The record holders are found in the copper oxide family (red), with a maximum $T_c$ of 165 K found in a "mercury" copper oxide under pressure (dashed red line). (From Ref. [5])

coherent quantum state, giving rise to a spectacular "macroscopic manifestation of quantum mechanics".

Within the standard BCS theory the pairing "glue" which leads to Cooper pair formation is provided by the electron-phonon interaction which leads to an effective overscreening of the repulsive Coulomb interaction at low energy. The phonon-mediated pairing leads to the isotope effect of the critical temperature, which is indeed one of the clearest experimental evidences in favour of the theory.

The BCS theory has been successful in explaining the fundamental mechanisms and the material trends of elemental superconductors and binary alloys. Its strong coupling extension due to Midgal and Eliashberg [6, 7] makes the agreement to some extent quantitative. With the term *conventional superconductors* are indicated all those materials which display a superconducting phase which can be described by these theories.

As we anticipated, there are however materials which display superconducting properties but are not described by the above theories. These are collectively known as *unconventional superconductors* and comprise heavy-fermion compounds, organic superconductors, copper-oxide superconductors and iron-based superconductors (FIGURE 1). We mention in passing that alkali-metal doped fullerides defy this distinction because the pairing is driven by phonons, yet superconductivity takes place in proximity of a Mott insulating state [8].

The unconventional superconductors of course share the main phenomenology of superconductivity, namely they have zero resistance

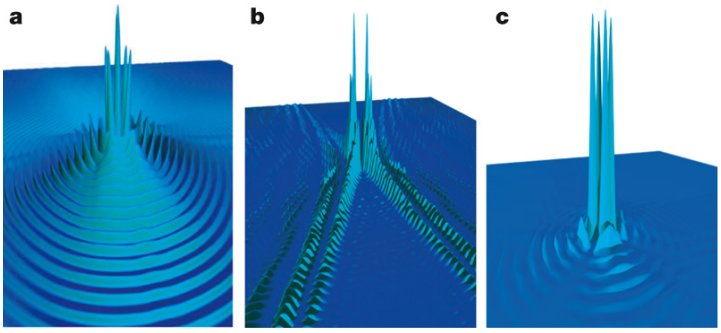


Figure 2: Representation of the absolute value of the Cooper pair wave function in two spatial dimensions. This is proportional to the probability of finding one quasiparticle in a Cooper pair state given that its partner is at the origin. The isotropic form in (a) is characteristic of a s-wave spin-singlet state. The two-fold symmetry in (b) of p-wave spin-triplet states, whereas the four-fold symmetry in (c) is characteristic of a d-wave spin-singlet state. (From Ref. [10])

and expel the magnetic flux from their interior (Meissner effect) and there is no doubt that the superconducting state arises from coherent Cooper pairs.

However, the net attraction responsible for Cooper pairing is almost certainly not mediated by phonons, in sharp contrast with BCS superconductors. This results in different characteristics of the Cooper pairs and of the superconducting state as a whole. For example, proposals have been made in favor of an attraction mediated by spin fluctuations [9]. Among the different characteristics, the symmetry of the wave function associated to the Cooper pair may vary and even be anisotropic, as opposed to the isotropic wave function typical of BCS pairing (FIGURE 2).

## 1.2 HIGH-TEMPERATURE CUPRATE SUPERCONDUCTORS

The copper-oxide family of superconductors – or cuprates – play a central role in the field of superconductivity not only because they show the largest critical temperatures, but also as paradigmatic examples of unconventional superconductivity which emerges upon doping a strongly correlated Mott insulator with antiferromagnetic ordering. Moreover, even though they were discovered three decades ago, in 1986 [2], and despite the huge effort of the community, a fully satisfactory theory is still lacking.

The cuprate family is composed by a large number of layered materials all sharing $CuO_2$ planes, typically separated by insulating spacer layers, which are generally believed to act as charge reservoirs, while the main microscopic phenomena leading to superconductivity and to the complex phase diagram of these materials are widely believed to occur in the $CuO_2$ planes. The electronic structure of these planes

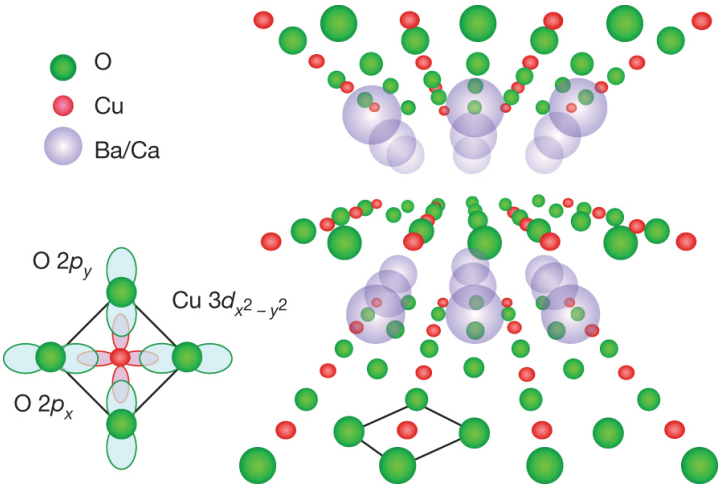


Figure 3: Layered copper oxides are composed of $CuO_2$ planes, typically separated by insulating spacer layers. The electronic structure of these planes primarily involves hybridization of a $3d_{x^2-y^2}$ hole on the copper sites with planar-coordinated $2p_x$ and $2p_y$ oxygen orbitals. (From Ref. [5])

primarily involves hybridization of a hole on the copper sites with planar-coordinated $2p_x$ and $2p_y$ oxygen orbitals (FIGURE 3). This leads to a single band crossing the Fermi surface, which can be described either with a microscopic model involving all the above orbitals, or with a single-band Hubbard model, in which the oxygen degrees of freedom do not appear explicitly.

In this work we can not review the rich and debated phenomenology of the cuprates, for which we can refer to a large number of review papers. Instead, we focus on the effect of strong correlations in determining the overall shape of the phase diagram and on the d-wave symmetry of the superconducting order parameter. A review may be found for example in Ref. [11].

The celebrated phase diagram of cuprates in the doping *vs.* temperature plane is usually interpreted in terms of the doping of a Mott insulator. In the absence of doping, these materials are antiferromagnetic Mott insulators with critical temperatures of several hundreds of K. The antiferromagnetic ordering is a standard G-type three-dimensional order despite the strong anisotropy of these materials.

When holes are doped into these materials by chemical substitution the antiferromagnetic order rapidly decreases and disappears at small concentrations (around 3% doping). Then at some material-dependent doping concentration a superconducting phase with d-wave symmetry establishes. Superconductivity survives for a finite window of doping and its critical temperature has a dome-shaped behavior with a maximum around 20% doping, which is usually called the "optimal doping" $x_c$. The optimal doping roughly defines also

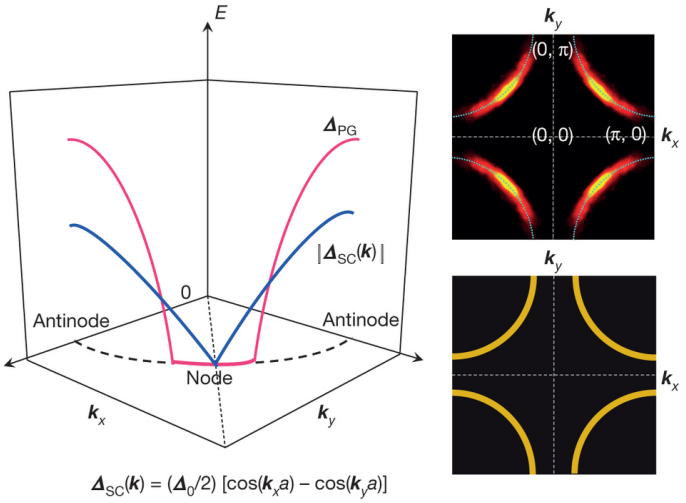


Figure 4: For large doping a large Fermi surface is observed (bottom right). At smaller doping the antinodal regions of the Fermi surface are gapped out, giving rise to the Fermi arcs characteristic of the pseudo-gap state (top right). This is reflected (left) in the angle dependence of the energy $E_k$ of the superconducting gap $\Delta_{SC}$ (blue line) and pseudogap $\Delta_{PG}$ (red line) as functions of the momenta $k_x$ and $k_y$. (From Ref. [5])

two regions with completely different properties in the normal state above the critical temperature. While the "overdoped" region $x > x_c$ has a normal state which obeys the standard Fermi-liquid theory, in the "underdoped" region $x < x_c$ we observe a strange metallic behavior and the existence of a "pseudogag" at relatively high temperatures. The pseudogap region remains one of the most debated and elusive aspects of the cuprate phase diagram. From a purely phenomenological point of view, the pseudogap is characterized as a gap-like depletion of low-energy spectral weight, more pronounced in the antinodal regions where also the superconducting gap is maximum, which essentially connects smoothly with the superconducting gap as the temperature is reduced below $T_c$.

Interpretation of the pseudogap physics range from a precursor of superconductivity, in which the system developes a modulus of the order parameter, but it is not able to establish macroscopic phase coherence, to a different ordered phase (candidates include charge ordering, stripes, loop currents, ...) which may be associated with a hidden quantum critical point.

## 1.3 SUPERCONDUCTIVITY IN STRONGLY CORRELATED MODELS

Immediately after the discovery of high-temperature superconductivity, P. W. Anderson [12] pointed out the Mott character of the insulating state of the undoped cuprates, and proposed that the same correlation effects responsible for the insulating behavior were the

most likely explanation of the superconducting state and the driving force behind the whole phase diagram.

*Normal phase*

A Mott insulator is a quantum state of matter in which the carriers are localized by the strong electron-electron interaction, despite the filling of the band would lead to a metallic state according to the band theory of solids. The simplest model to describe a Mott insulator and the Mott transition connecting the insulator to a metal is the (single-band) repulsive Hubbard model:

$$\mathcal{H} = \sum_{ij\sigma} c^{\dagger}_{i\sigma} c_{j\sigma} + U \sum_{i} n_{i\uparrow} n_{i\downarrow}, \tag{1}$$

where $c_{i\sigma}$ creates electrons at site $i$ with spin $\sigma$ and hopping amplitude to another site $j$ given by $t_{ij}$. The interaction is parametrized by a screened Coulomb interaction $U > 0$ which measures the energy cost of having two electrons at the same time on the same lattice site.

We can picture the existence of a Mott transition by describing the model in the two extreme limits of vanishing interaction (non-interacting limit) and of vanishing hopping (atomic limit). We consider the situation in which the number of electrons equals the number of lattice sites $N_s$.

In the former limit, we can easily diagonalize the Hamiltonian in momentum space, which leads to a single band of dispersion $\varepsilon(k) = \sum_{ij} t_{ij} e^{k(R_i - R_j)}$, where $R_i$ is the coordinate of site $i$. The band can host up to $2N_s$ electrons due to the spin degeneracy. Hence in the case of $N_e = N_s$ the band is half-filled and it describes a metal according to band theory. Hence this regime is usually referrred to as half-filling.

In the opposite limit of vanishing hopping, the system is obviously dominated by the Coulomb term, which favours configurations without doubly occupied sites. In the half-filling condition, all the configurations with one electron per site have the lowest energy, thus leading to an exponentially ($2^N$) degenerate groundstate. If we relax the zero-hopping approximation, but we remain with a large $\frac{U}{t}$ ratio, then we can show that, at the leading order, the Hubbard model can be mapped onto a Heisenberg model $\frac{t^2}{U} \sum_{ij} S_i \cdot S_j$ (where $S_i$ is the spin carried by the electrons on site i). Therefore the system is antiferromagnetic at zero temperature and it orders at finite temperature at least in three or more dimensions. There will therefore be a critical (Néel) temperature for the magnetic ordering which at strong coupling will vanish as $\frac{t^2}{U}$, the only energy scale in our Heisenberg model. Therefore at strong coupling the model describes an insulating system with antiferromagnetic ordering.

Since the model is metallic for $U = 0$ and insulating for large $U/t$ a metal-insulator transition is expected to occur at zero temperature as a function of the ratio $U/t$. We remind, for completeness, that in the case where the hopping is limited to nearest-nighbouring sites, the metallic state is unstable towards antiferromagnetism for any non-zero $U$, as it can easily be shown by means of a Hartree-Fock decoupling of the interaction. However, as soon as the hopping acquires longer-range components, or the lattice is not bipartite, a critical value for magnetic ordering is found. Furhermore, even in the case where the system is magnetically ordered at zero or low temperature, a genuine finite temperature metal-insulator transition takes place. The theoretical study of this transition requires intrinsically non-perturbative approaches, among which the dynamical mean-field theory (DMFT) occupies a central role nowadays.

If we extend the strong-coupling analysis out of half-filling, we can approximate the effective strong-coupling model with the popular $t - J$ model, in which the electronic hopping is restored, but it is constrained by the projectors $P_i$ to processes which do not create doubly occupied sites:

$$\mathcal{H} = -t \sum_{ij\sigma} P_i c^{\dagger}_{i\sigma} c_{j\sigma} P_j + \frac{J}{4} \sum_{ij} (\hat{\sigma}_i \cdot \hat{\sigma}_j - n_i n_j) - \mu \sum_i n_i. \qquad (2)$$

A striking characteristic of this model – which can actually be obtained also starting from a three-band picture of the $CuO_2$ planes in which the copper and oxygen orbitals are explicitly taken into account – is that its mean-field phase diagram contains a superconducting phase with d-wave symmetry [13, 14].

*Superconducting phase*

The common wisdom about the high-temperature superconductors is that the superconducting state is less "anomalous" with respect to the normal state. This should not be taken as an argument in favour of a standard BCS mechanism, but just as a suggestion that the phenomenological understanding of the properties of the superconducting state, including its non-equilibrium dynamics, does not necessarily require a solution of the microscopic correlated models, at least as far as qualitative aspects are concerned.

For this reason in this thesis we will focus on two different strong simplifications of the problems, namely:

- A mean-field model for a d-wave superconductor, in which we retain the correct symmetry of the order parameter, but we neglect all the effects of the interaction beyond static mean-field as well as the competition with any other instability;
- An attractive Hubbard model as model of superconductor with strong correlations which, treated beyond mean-field via the

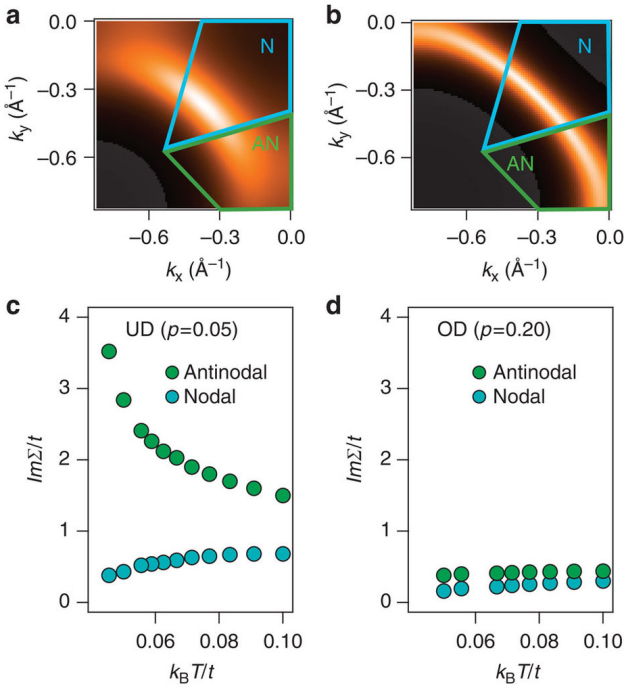


Figure 5: The single-band Hubbard model and cluster-DMFT. (a,b) Fermi surface for underdoped (UD) and overdoped (OD) system. (c,d) The imaginary parts of the self energy as a function of temperature. The underdoped system displays two different behaviors: insulating at the antinode and conducting at the node [15].

extension of DMFT to nonequilibrium, fully accounts the local quantum fluctuations, but cannot describe any anisotropic structure of the gap.

The time-dependent mean-field theory of the d-wave superconductor is the subject of the second part of the thesis. This model has the advantage of highlighting the effect of an anisotropic gap in the simplest configuration, and it allows a straightforward comparison with analogous models with isotropic gap. In this way, we will be able to disentangle the effect of the anisotropic gap.

### d-*wave symmetry*

Since the first years after the discovery of high-temperature superconductivity in cuprates, one of the most debated issue has been the question regarding the symmetry of the pairing state. Indeed the determination of the order-parameter symmetry is clearly a crucial step in identifying the pairing mechanism and therefore in the development of a microscopic theory. Although the mechanism responsible for this attraction is still under debate, there is now general consensus that the resulting gap function has a symmetry of the type $d_{x^2-y^2}$.

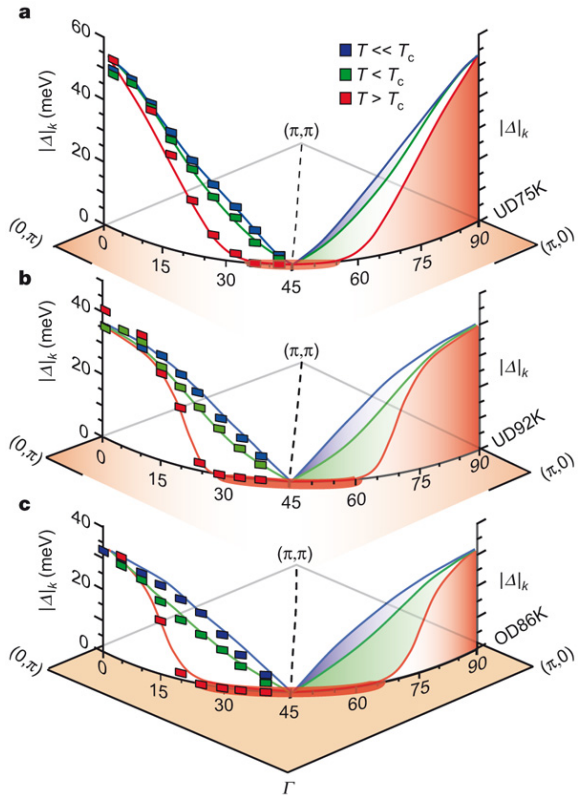


Figure 6: Schematic illustrations of the gap function evolution for three different doping levels (indicated on the right) and three different temperatures. (From Ref. [17])

This conclusion is supported by many experimental observations and is also indicated as the most probable by theoretical calculations.

Pheraps the most important characteristic of a gap with $d_{x^2-y^2}$ symmetry is that it exhibits nodal lines, thus leading to excitations at zero-energy. This is in sharp contrast with the conventional superconductors which have a constant gap which therefore represents the minimum excitation energy. The presence of these low-energy excitations has been firmly estabilished by a variety of transport experiments as well as measurements of thermodynamics quantities [16]. These experiments confirm that, although there is substantial evidence for electron pairing, there are also extensive experimental data that show that the energy gap is not fully formed or, in other words, it vanishes for some momenta.

In the case of conventional superconductors, the energy gap in the excitation spectrum manifests itself in exponentially activated temperature dependences of a wide variety of transport coefficients and thermodynamic quantities at low tempertaures. On the other hand, the low-energy excitations of superconductors with nodal lines usually give power-law temperature dependences. One example is the temperature dependence of the London penetration depth $\lambda(T)$, which is a measure of the penetration of the electromagnetic field inside the

superconductor and at low temperature reflects changes in the superfluid density [18]. Microwave techniques for measuring $\lambda(T)$ most commonly measure the temperature dependence of the deviation of $\lambda(T)$ from its zero temperature value, $\delta\lambda(T) = \lambda(T)—\lambda(0)$. In s-wave BCS theory this quantity is given by an exponential expression which is a consequence of the energy gap. In the cuprate $YBa_2Cu_3O_{7-\delta}$ it was found that the penetration depth has a power-law behavior in temperature, thus confirming its non-conventional character [19]. This power-law behavior can only be explained admitting the existence of nodal lines in the superconducting gap function.

Further evidence is given by tunneling measurements, which display a non-vanishing density of states for energies below the gap, with the current *vs.* voltage characteristic exhibiting power-law rather than exponential temperature dependence at low temperature. This increased excitation density over that expected for a fully-gapped superconductor has been documented by countless experiments since the discovery of the cuprates, and is now generally accepted to be an intrinsic property of these materials.

Finally, a striking and direct experimental evidence for the d-wave symmetry of cuprates is given by angle-resolved photoemission spectroscopy (ARPES) experiments [20, 21] which can directly map the energy dispersion of the material as a function of momentum. These experiments showed that the gap in the spectrum depends on the momentum and is maximum along the $x$ and $y$ axes of the Brillouin zone and vanishing along its bisectrices (FIGURE 6).

While the above experiments can detect the *magnitude* of the order parameter – or gap-function – it is crucial to measure also its *phase*. Indeed, the phase of a function with $d_{x^2-y^2}$ symmetry changes from $0$ to $\pi$ upon rotation of $\frac{\pi}{2}$. A class of experiments was therefore designed to determine the pairing-state symmetry by looking at the phase coherence of tunnel junctions and SQUID devices incorporating high-temperature superconductors. These experiments are based on the Josephson effect at the junction between the high-$T_c$ superconductor and a conventional superconductor. The key feature of these experiments is their sensitivity to the anisotropy of the phase of the order parameter rather than to its magnitude. This enables a direct test of the most unique and characteristic feature of the proposed d-wave state: the sign change in the order parameter in different k-space directions. These experiments have provided an incontrovertible evidence for a pairing state with at least a large component of d-wave symmetry [22].

It is worth to mention that also time-resolved experiments on the relaxation of quasiparticles in excited states (which are the subject of the next CHAPTER 2) are consistent with a pure d-wave gap [23].

On the theoretical ground, the d-wave state is implied by a number of different possible pairing mechanisms, including in particular

the exchange of spin-fluctuations [9]. Also at an intuitive level it is possible to understand why a gap-function with nodal lines may be energetically favorable in systems with strong electron correlations. Indeed, the repulsive electron-electron interaction is very strong at short distances and decay at long distances. Since the gap function, or pairing function, $\Phi(r)$ is related to the probability of finding one quasiparticle in a Cooper pair state given that its partner is at the origin, the repulsive electron-electron interaction favours pairing functions which are zero for zero distance $\Phi(r = 0) = 0$. In momentum space this condition reflects in the vanishing of the integral $\int \Phi(k)\, dk$ so that to satisfy both this condition and to have a finite pairing function there must be regions where $\Phi(k)$ is positive and regions where it is negative, with the nodal lines separating them.

*Strong correlations*

In the third part of the thesis we will study the non-equilibrium dynamics of the attractive Hubbard model using a non-perturbative approach. The attractive Hubbard model is known to have a superconducting groundstate with s-wave symmetry at any value of the interaction in dimensionality equal or larger than two. For weak interactions, a static mean-field is expected to work, which implies that the critical temperature (in three or more dimensions) and the order parameter are exponential in the coupling strength. In strong coupling, instead, superconductivity can be understood in terms of a Bose-Einstein Condensate (BEC) of preformed pairs. In this regime, Cooper pairs can form at very high temperature because of the large energetic gain, but phase coherence can establish only at much lower temperatures. As we will discuss in the following, the critical temperature actually decreases like $1/U$ for large values of the interaction. As a result, in the crossover region that separates these two limiting regimes, $T_c$ has a maximum for intermediate coupling strengths The continuous evolution between a standard BCS superconductor and a BEC superconductor is usually referred to as the BCS-BEC crossover, and it has been extensively studied in different contexts.

Before discussing the relevance of the BCS-BEC crossover for superconductivity in the cuprates, we recall a simple mathematical relation between the attractive and the repulsive Hubbard models which is particularly useful to extract some basic properties of the attractive Hubbard model.

The key observation is that the unitary transformation:

$$c_{i\uparrow} \to c_{i\uparrow}, \tag{3a}$$

$$c_{i\downarrow} \to (-1)^i c^\dagger_{i\downarrow}, \tag{3b}$$

maps the repulsive Hubbard model onto an attractive one. The details of the transformation are not necessary for the present discussion, but

we mention that the mapping essentially inverts the roles of density and uniform magnetization and of the conjugated variables, chemical potential and magnetic field. More precisely, the magnetization maps onto the doping with respect to half-filling and viceversa. In particular the two models map exactly one onto the other if taken at half-filling and zero magnetization. Furthermore, the three components of the staggered magnetization of the repulsive model map onto a staggered density wave ($z$-component) and $s$-wave superconductivity ($x$- and $y$- components, which correspond to the complex superconducting order parameter).

Therefore all the information we gain from one model can be used to understand the other. In this light, for example the decrease of the Neel temperature for large $U$ that we discussed before implies the $1/U$ decrease of the superconducting critical temperature that we introduced in the previous paragraph.

Moreover, the mapping can help us to understand the normal state of the attractive Hubbard model as soon as the critical temperature is exceeded. In weak coupling, as soon as superconductivity disappears, we expect to recover a normal Fermi liquid, while in the strong coupling limit, we can understand the normal state of the attractive model starting from the Mott insulating state of the repulsive model. In the latter, we have a collection of singly occupied sites, either with spin up or spin down. Under the particle-hole transformation, this state becomes a collection of doubly occupied and empty sites, which we can call a "pairing insulator" [24, 25]. In this state all the electrons are paired-up because of the strong attraction. This state is however insulating because the pairs are completely localized and they are unable to establish phase coherence. As a matter of fact the kinetic energy of the pairs is so small that they can not "talk" one another leading to a single condensate. This can only happen at $T_c$, which is small for large values of $U$ and corresponds precisely to the energy scale associated with phase coherence, in turn proportional to the superfluid stiffness [26].

Therefore, increasing the interaction from weak to strong one moves from a Fermi-liquid normal state to a paired state which is nothing but a collection of "preformed pairs". If we interpret the pseudogap region of the underdoped cuprates as a precursor of superconductivity, this evolution of the attractive Hubbard model can be compared with the evolution of the normal state of the cuprates when the doping is reduced from the Fermi-liquid overdoped samples to the pseudogapped underdoped companions. At the same time, the critical temperature has a maximum in the intermediate region in both cases. This parallelism defines the range in which we can use the attractive Hubbard model in the context of high-temperature superconductivity.

Of course this description does not imply that the attractive model is by any means an accurate microscopic model for the cuprates, but it helps to highlight and disentangle all the features of the experimental phase diagram which can be attributed to an evolution from weak to strong coupling superconductivity. Notice that a similar evolution is expected in any theory in which the superconducting pairing itself originates from the Mott insulator, and it is for example features in resonating valence bond theories and in numerical studies of the repulsive Hubbard model. However, the approach completely neglects the d-wave symmetry of the order parameter and the possibility of other competing instabilities characteristic of the repulsive model or of more accurate and complete models.

# 2

# TIME-RESOLVED SPECTROSCOPY OF CORRELATED MATERIALS

High-temperature superconductors are only a part of a broader family of materials displaying spectacular properties – the "strongly correlated systems". Most of these materials are transition-metal oxide compounds and are characterized by very rich phase diagrams with different phases proximal to each other. Moreover, their behavior is not rarely in disagreement with the paradigms of the early solid state theory, for instance the standard band theory. For these reasons, their study constitutes an intellectual and technological challenge which attracts enormous effort in the condensed matter community nowadays. The challange is to understand the mechanism behind their behavior, which is not an easy task because it often appears that this is the consequence of the interplay of many interacting degrees of freedom – charge, spin, lattice, orbital.

In recent years, new and exciting results are being achieved by the use of new methods based on *time-resolved* spectroscopy. The development of these techniques opened up a wealth of information unavailable to conventional *time-averaged* spectroscopies and triggered a growing interest in the theoretical investigation of the transient dynamical behavior of strongly correlated systems. In this chapter we illustrate the basis of these techniques and review a few recent results directly related to the following parts of the thesis.

## 2.1 PUMP-PROBE EXPERIMENTS

Time-resolved spectroscopies are based on the ability to track the time evolution of the system under study. In this respect, they are fundamentally different from the conventional time-averaged spectroscopies. The latter are founded on the concept and ability of measuring the properties of the *unperturbed* system. Of course, any real experiment inevitably perturbs the object of the observation. However, under certain circumstances and assumptions, one can applies theoretical concepts such as the linear response theory and the fluctuation-dissipation theorem, which allow a direct connection of the observations to the unperturbed *equilibrium* properties.

However, if one has the ability to track the time evolution of the system, in particular with a time resolution of the order of its basic microscopic processes, one could think of much more general experiments, in which one deliberately perturbs the system from its equilibrium state to a *nonequilibrium* state and subsequently observes the

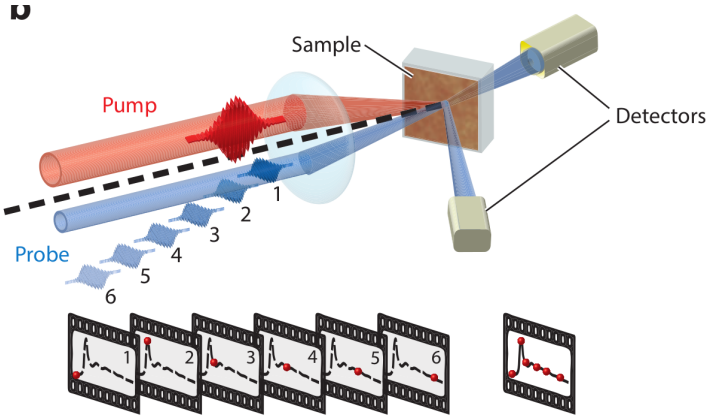


Figure 7: Ultrafast optical spectroscopy. A pump pulse (red) creates a nonequilibrium state. By sweeping the probe pulses (blue) at different delays (labeled with numbers) snapshots of the transient state are taken to temporally resolve the nonequilibrium dynamics. The pump beam may be in the visible, the mid-IR, or the terahertz and determines mode selectivity. Even greater selectivity exists for the probe and may also include UV, X-rays, or electrons (From Ref. [27]).

properties of the system during its dynamics, which will eventually relax to the original state. The gain by doing so is that the coupling between the above cited degrees of freedom – charge, lattice, spin – may lead to various different non-equilibrium processes whose observation in real-time may lead to learn something about the mechanism of their interplay [28, 29].

Since the relevant electronic energy scales in solids are of the order of the electronvolt, the time scale of the electronic processes is of the order of $\frac{\hbar}{eV} \simeq 4\,10^{-15}$ s, i. e. of the order of the femtosecond. Therefore one needs extremely short pulses to address this physics, hence the name of "ultrafast" time-resolved spectroscopy [30–32].

These ultrafast spectroscopies are based on the basic pump-probe setup skatched in FIGURE 7. By shining the sample with a first, intense laser pulse – *pump* – one brings the system in a nonequilibrium transient state. A second, usually weaker, laser pulse – *probe* – hits the sample with a given time delay and records the relaxation dynamics.

In practice, most of the times one uses a single source of laser pulses, whose beam is split in two: one directly shines the sample, exciting electrons in the lattice, and the other probes the induced transient changes. However, before reaching the sample, the probe beam is sent through a different path, usually of a variable lenght, via for example a movable mirror. This provides a variable path length, and hence a time delay, relative to the absorption of the pump beam. One therefore collects snapshots of the system's dynamics by repeating

the experiment for various time delays and finally gets the whole time-resolved picture of its relaxation.

The pump-probe scheme is quite versatile, as one can modify each of the single components to achieve different measurements. Indeed, beside changing the probe delay by varying its optical path, one can also to some extent tune the frequency of the pulses, which is originally the frequency of the pulsed laser, usually a Ti:sapphire laser of frequency 1.5 eV. By the use of nonlinear optical crystals, via a process known as optical rectification, one can produce far-infrared pulses which can selectively probe low-energy modes, such as phonons and other low-energy collective excitations. On the other hand, one can also obtain ultra-violet pulses to realize a time-resolved photoemission experiment.

The developing of these techniques had to wait for some fundamental technological advances, the main challenge consisting in the generation of short and stable laser pulses. That is why these techniques have become popular in the field of strongly correlated materials only in relatively recent times.

## 2.2 TIME-RESOLVED OPTICAL SPECTROSCOPY

Since the early times of ultrafast spectroscopy on correlated materials, experiments showed how this technique can provide new insight into the physics of these systems. The first pioneriing experiments were performed using pulses at a single frequency – *single-color* – and detecting the change in reflectivity. Even with this minimal setup, which is rather limited if compared to modern broadband supercontinuum – *multi-color* – or ARPES experiments, it was soon realized how it became possible to shed light on a number of interesting phenomena unaccessible to the conventional time-averaged spectroscopy. This is consequence of the ability to track the dynamics with a time resolution faster than the basic electronic relaxation times.

Time-resolved experiments are complementary to the conventional time-averaged experiments. In particular, they can provide new pieces of evidence in support to observations done at equilibrium. This is the case of the presence of a gap, which in equilibrium manifests itself in virtually all transport coefficients and thermodynamics quantities, whereas out-of-equilibrium manifests itself in the quasiparticle relaxation rate. In turn, the quasiparticle relaxation rate is related to the change in reflectivity, so that measuring the change in reflectivity one can infer about the presence of a gap in the spectrum [15]. In this way it is also possible to investigate the character of the gap, e. g. its symmetry and temperature dependence.

Even more interesting is the possibility to access information not available at all to equilibrium spectroscopies. Notable examples are the possibility to disentangle the various bosonic contributions to the

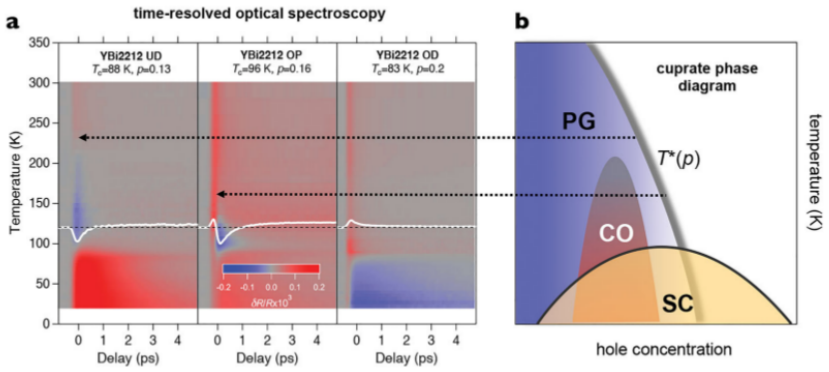


Figure 8: The pseudogap state unveiled by non-equilibrium techniques. Left: The relative reflectivity variation measured in the single-color configuration for three different hole concentrations. Right: The generic phase diagram of cuprates. The pseudogap boundary $T^*(p)$ (grey curve) is determined reporting the temperature at which a negative component in the reflectivity signal appears. (From Ref. [15])

quasiparticle scattering [28] or the dynamics of coupled order parameters [33]. Moreover, the recent advances in ultrafast spectroscopy, such as the use of multi-color pulses and time-resolved ARPES, have made these techniques even more powerful.

*Relaxation across a gap*

The pioneering works on single particle relaxation in cuprates was performed on the yttrium barium copper oxide $YBa_2Cu_3O_{7-\delta}$ (YBCO). Early experiments detected the appearance of a transient reflectivity below the superconducting critical temperature $T_c$, therefore related to the quasiparticle dynamics in the superconducting state. In general, all the time-resolved optical measurements evidence a slowing down of the relaxation dynamics of the optical signal, whose time constant rapidly changes from 100 to 200 fs in the normal phase to several picoseconds in the superconducting phase.

The transient change of reflectivity can be interpreted in terms of transient dielectric constant and Drude response, which arise from quasiparticles excited by the pump pulse. Phenomenological models, such the one of Rothwarf and Taylor [34], describe the quasiparticle relaxation in gapped systems as a function of various variables and parameters of the system, such as temperature, gap amplitude and quasiparticle recombination rate. Then one can extract these parameters by fitting the experimental change in reflectivity.

Apart from temperature and doping one can also study this relaxation as a function of fluence, i. e. the energy per unit surface of a single pump pulse. In this way it is possible to verify that the dynamics of quasiparticles is consistent with the Rothwarf–Taylor model, in

which the gap-energy bosons emitted during the recombination of quasiparticles into Cooper pairs act as a bottleneck for the recombination dynamics.

In this way, it was recorded the simultaneous presence of the superconducting gap and the pseudogap in all parts of the phase diagram, with distinct relaxation times and temperature dependences. Strictly speaking, the system is in the pseudogap phase only for temperatures $T_c < T < T^*$. However, in the literature one often refers to the terms "pseudogap" to indicate the gap at the antinode also for $T < T_c$, and "superconducting gap" for the gap closer to the nodes. This terminology clearly originates from the fact that the gap at the antinodes survives above the critical temperature, in the proper pseudogap phase, whereas the gap closer to the nodes is present only in the superconducting phase.

These experiments showed a very consistent picture of a multicomponent response in which the recombination dynamics across the superconducting gap is quite distinct from that across the pseudogap. In particular the recombination time across the superconducting gap vanishes sharply at the critical temperature, as a consequence of the closing of the gap. In the normal state, the pseudogap response gradually diminishes until it vanishes at a temperature $T^*$ , which is consistent with the "pseudogap temperature" measured by other techniques which measure a charge gap.

It is therefore confirmed a two-gap scenario: a picosecond recovery of the superconducting condensate in underdoped and optimally doped material and, in underdoped samples, an additional subpicosecond component related to pseudogap correlations.

*Electron-boson interaction in correlated materials*

Since the discovery of high-temperature superconductivity in copper oxides, a reliable measurement of the electron–phonon coupling function has been considered crucial for the understanding of the physical mechanisms responsible for the pair formation. Nonetheless, the interplay of different bosonic degrees of freedom on similar energy scales makes it difficult to single out the electron–phonon constant and to estimate its strength.

More in general, one of the most genearal issues regarding correlated materials is the relaxation of excited quasiparticles in correlated insulators, i. e. in materials which can be in first approximation described by models such as the Hubbard model described in CHAPTER 1 which are characterized by the presence of a gap due to electron-electron correlations. This is of course also related to cuprates since the parent compounds belong to this class.

In conventional systems described by band theory, one has very different responses in the cases of gapped semiconductors and un-

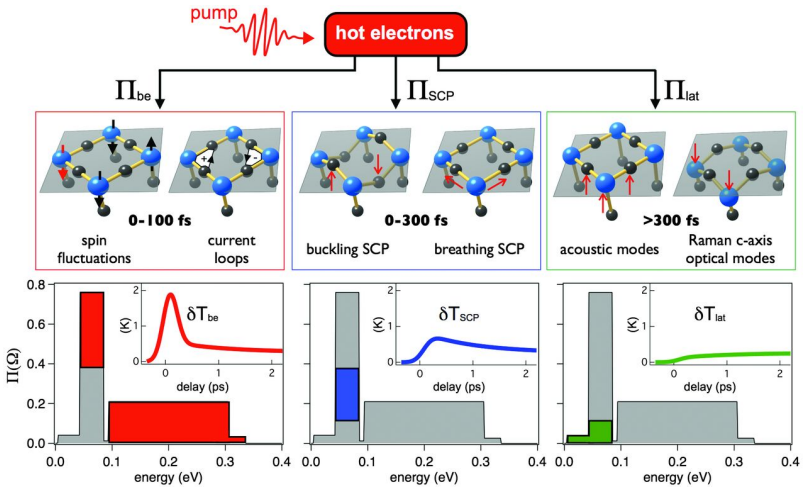


Figure 9: Disentangling the contributions to the total bosonic function. The electronic ($\Pi_{be}$, red areas), strongly coupled phonon ($\Pi_{SCP}$, blue area), and lattice ($\Pi_{lat}$, green area) contributions to the total bosonic function are shown. The insets display the temporal evolution of the temperatures $T_{be}$ (red line), $T_{SCP}$ (blue line), and $T_{lat}$ (green line). Sketches of the possible microscopic mechanisms at the base of the different contributions to the total $\Pi(\Omega)$ are shown in the upper panels. (From Ref. [28])

gapped metals. While in metals the continuum of the electronic levels allows a prompt relaxation in fractions of picosecond, in semiconductors the gap is usually larger than the spectral width of the bosonic excitations available in the system. Considering the phonons, the cutoff of the maximum energy that can be transferred in a single scattering process is on the order of 100 meV. As a consequence, a non-thermal population is rapidly accumulated on the bottom of the conduction band, until radiative decays or multi-phonon processes eventually lead to the complete relaxation on a relatively longer timescale, of the order of the nanosecond.

At first sight, the relaxation process in correlated insulators should be similar to that observed in semiconductors. Since the correlation gap is large (1.5 eV) and robust, the expectation is that the impulsive photo-excitation would create a long-lived metastable state. Pioneering measurements on charge-transfer insulators soon evidenced a more complex picture than that which was naively expected for conventional systems [35].

The role of the excitation process has been also addressed by studying the ultrafast dynamics of quasi-particles in the parent compound $La_2CuO_4$ [36]. While the above-gap excitation injects electron–hole excitations that subsequently exchange energy with the boson baths (antiferromagnetic fluctuations, phonons), the sub-gap excitation drives the formation of itinerant quasi-particles, which are suddenly dressed by an ultrafast reaction of the bosonic field. This result evidences that,

in the case of sub-gap excitation, the interaction between electrons and bosons manifests itself directly in the photo-excitation processes.

Time-resolved optical spectroscopies also open new scenarios in the study of the electron–boson coupling in copper oxides. Indeed, the electron relaxation rate is directly related to the frequency-integral of the coupling function $\Pi(\Omega)$, which describe the electron-boson scattering also in equilibrium situations [37]. Moreover, in some circumstances it is possible to describe the relaxation process in terms of "effective temperatures" associated to the various components in play: electrons, phonons, bosons of different nature. As far as the underdoped region of the phase diagram and the pseudogap state are avoided, the concepts underlying the effective temperature model can be extended to interpret the dynamics of moderately doped cuprates and other correlated materials.

From the experimental standpoint, the experimental resolution did not allow, until recently [29], to directly follow, in the time domain, the coupling with bosons of electronic origin. Nevertheless, the combination of the ultrafast time-resolution with the broad spectral window accessible by the supercontinuum-based time-resolved spectroscopies has been a turning-point in the study of the electron–boson coupling in copper oxides. By measuring the dynamics of a broad part of the reflectivity around the dressed plasma frequency, it has been suggested that the reflectivity variation is directly proportional to the electron–boson scattering rate [28]. Therefore, by monitoring reflectivity variations, it is possible to reconstruct the dynamics of the average boson density and estimate the electron–boson coupling within the effective temperature model, as pictorially shown in FIGURE 9. This technique evidenced that on a timescale faster than the electron–phonon coupling, that is of the order of 100 fs, the charge carriers are already effectively coupled with bosons of electronic origin.

## 2.3 TIME-RESOLVED PHOTOEMISSION

We now turn our attention on a particular type of ultrafast time-resolved spectroscopy, namely the time- and angle-resolved photoemission spectroscopy (trARPES). Rather generally, angle-resolved photoemission spectroscopy (ARPES) is based on the photoelectric effect by which, when a material is irradiated with light, an electron can absorbe a photon and escape in the vacuum – so-called "photon-in electron-out" [20]. The basic principle of the technique is that, by detecting the kinetic energy and angle of expulsion of the photoejected electron, one can determine to some extent its binding energy and crystal momentum prior to the photon absorption. Indeed, to assure the energy conservation of the photoelectric process, the kinetic energy of the electron has to be equal to $E_{kin} = E_B + \hbar\nu - \phi$, $\hbar\nu$ being the quantum of energy of the incident ligth, $E_B$ the binding energy of

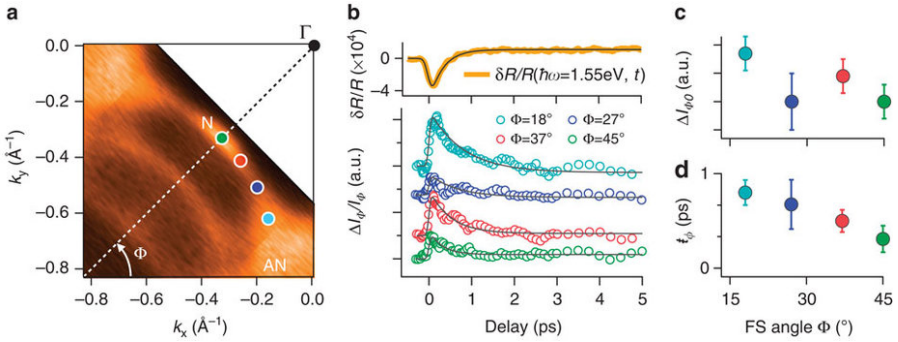


Figure 10: Equilibrium and non-equilibrium photoemission. (a) Fermi surface measured by conventional ARPES at 100 K. (b) Variation of the time-resolved ARPES intensity for different points along the Fermi arcs. (c,d) Maximum intensity variation and decay time of the non-equilibrium transient population (From Ref. [15]).

the electron and $\phi$ the work function of the sample. The latter is the energy difference between the vacuum and the highest occupied electronic state in the material and in metals is typically in the range of a few electronvolts. Clearly, the work function is the minimum energy we have to provide to the system to photoeject an electron.

A complete description of the photoemission process is a rather challenging task, therefore the interpretation of the experimental data often relies on certain simplifications. First, the photoelectric effect is decomposed in three independent steps: (i) optical excitation between two electronic states in the solid, (ii) travel of the excited electron to the surface, and (iii) escape of the photoelectron into vacuum after transmission through the surface potential barrier. Then, one usually makes the "sudden approximation" of neglecting the relaxation of the system during the photoemission itself.

A great advantage of ARPES is that one can measure not only the energy but also the angle of the trajectory of the ejected electron relative to the sample surface. From this, one can infer not only the binding energy but also, to some extent, the crystal momentum of the electron in the solid. However this is not an easy task, since while the component parallel to the surface of the sample is conserved, the perpendicular component is not, and one needs further assumptions in order to determine it. Fortunately, layered materials, such as cuprates, are characterized by a strong anisotropy and an almost vanishing dispersion along one direction, which makes this limitation much less severe. In these cases, the ARPES signal as a function of probed energy and momentum can be directly related to the density of states of the electrons in the material – spectral function – weighted by their average occupation.

The information contained in the ARPES signal $I(k_x, k_y, \omega)$ as a function of momentum $(k_x, k_y)$ and photon energy $\hbar\omega$ can be visualized in different ways. For instance, one can visualize the intensity for a

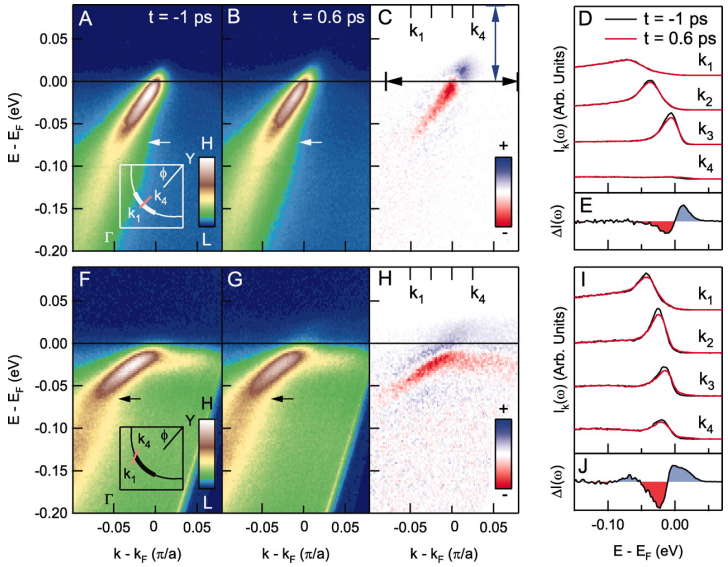


Figure 11: Typical ARPES dispersions before and after pumping for nodal ($\phi = 45°$) and gapped ($\phi = 31°$) regions of k-space. (A) Equilibrium and (B) transient (time delay of 0.6 ps) energy-momentum maps for the nodal state. (C) Subtraction between (A) and (B). Blue indicates intensity gain and red intensity loss. (D) Energy distribution curves (EDCs) shifted vertically for ease of comparison. (E) Difference between transient and equilibrium EDCs, integrated across the double black arrow in (C). (F to J) Same as (A to E) but for a gapped (off-nodal) momentum cut. (From Ref. [38])

given $\omega$ on the $(k_x, k_y)$ plane, as in FIGURE 10. Another way is to fix some direction in k space and visualize the ARPES intensity as a function of momentum along this line and energy. These are the so-called energy-momentum maps as depicted in FIGURE 11. Yet another possibility is to plot the intensity against the energy for a given momentum, these are the so-called energy-distribution curves also shown in FIGURE 11. Finally, a common way to visualize the trARPES intensity is to integrate around some region in k-space and some energy window and plot the result against time, as in FIGURE 10.

*Meltdown of nodal quasiparticles*

Here we discuss a series of trARPES experiments on the optimally doped cuprate $Bi_2Sr_2CaCu_2O_{8+\delta}$ ($T_c = 91$ K) which measured the quasiparticle relaxation times and to some extent the gap dynamics in different sector of k-space [38, 39]. It was demonstrated how the nodal lines and the anisotropy of the superconducting cuprates deeply affect the dynamics. In FIGURE 11 the trARPES intensity at $T = 18$ K is visualized in two energy-momentum maps for two representative directions: the nodal line and a line farther from the node, generically indicated as off-nodal. The figures on the left are the equilibrium sig-

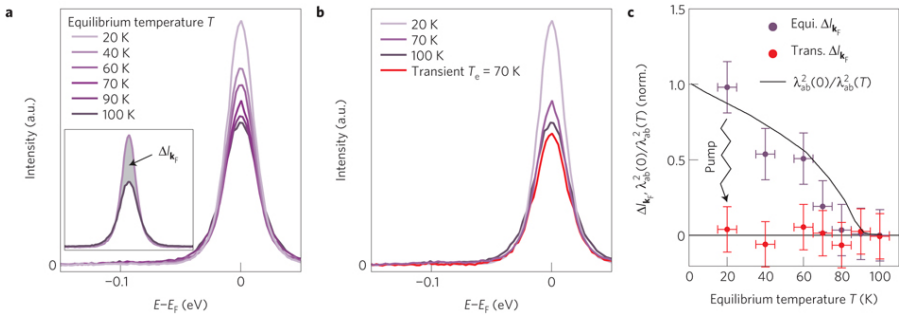


Figure 12: Comparison between temperature-driven and pump-driven spectral-weight suppression. (a) energy distribution curve (EDC) along the nodal direction at several temperatures. (b) Selected EDCs at equilibrium compared with the nonequilibrium EDC. (From Ref. [39])

nal, sometimes denoted as "negative time" since the measurements is done before the pump hits the sample. The d-wave structure of the superconducting gap is evident, since the off-nodal spectrum is gapped and the one at the node is not. The spectra on the right are measured a few hundreths of femtoseconds after the pump pulse and show marked differences with the equilibrium data, which are more evident if one takes the difference of the two sets of data.

In particular it is evident an overall transfer of spectral weight across the Fermi energy, which indicates the creation of transient quasiparticles, and a shift of the spectral peak toward the Fermi energy along the off-nodal line, indicating a partial closure of the superconducting gap.

As discussed above, the energy-momentum maps are obtained fixing a direction in the Brillouin zone. If one fixes also a point along this direction, then the momentum is completely determined and one can plot the ARPES intensity against the energy in the energy distribution curve (EDC) as in FIGURE 12. In particular, from the EDC taken on the Fermi surface one can extract the value of the gap.

A second experiment on the same material revealed an unexpected link between nodal quasiparticles and superconductivity. It was indeed observed a strong suppression of the nodal quasiparticle spectral weight, that is of the trARPES signal, following pump laser excitation, and its recovery dynamics was measured. This suppression was somehow unexpected, as nodal quasiparticles are believed to be robust and do not change much in going from below $T_c$ to above $T_c$ at equilibrium. However, out of equilibrium the dynamics is much changed, with the "melting" of the nodal quasi particles greatly enhanced in the superconducting state.

In FIGURE 12 in particular it is shown how this effect can not be ascribed to a raise in temperature due to the pump pulse. Indeed, from the shape of the Fermi edge one can extract an "electronic tem-

perature" of 70 K, while from the loss of spectral weight one would deduce a temperature of more than 100 K.

## 2.4 THEORY OF TIME-RESOLVED PHOTOEMISSION

The theory of ARPES needs to be extended to cope with the interpretation of these newly available experiments. In particular, as discussed above, at equilibrium the occupation of the single-electron energy levels is given by the Fermi-Dirac distribution $f(\omega) = (1 + e^{\beta\omega})^{-1}$ where $\beta$ is the inverse temperature. Therefore, denoting with $A(k_x, k_y, \omega)$ the spectral function one has:

$$I(k_x, k_y, \omega) = f(\omega) A(k_x, k_y, \omega). \tag{4}$$

Actually, the product on the right hand side of the equation is proportional to the Fourier transform of the so-called lesser Green's function which is indeed a measure of the occupation of single-particle energy levels $G(t', t) = i\langle c^\dagger(t') c^\dagger(t)\rangle$. On the other hand, the spectral function $A(k_x, k_y, \omega)$ is directly related to the so-called retarded Green's function. It is an important result of many-body theory that these two functions are not independent in equilibrium situations.

In trARPES however, the system is not at equilibrium therefore the relation between the lesser and the retarded Green's function ceases to be applicable. Morevoer, whereas at equilibrium the physics is invariant for time translation, this does not hold in time-resolved experiments as in this case the system is evolving in time. In practice, the Green's functions are no more functions of the difference of the two times but instead depend on two times separately. This poses the problem of defining the right time-frequency transform to compare with the experiments, in which one measures *directly* a signal as a function of energy, that is to say, frequency.

A full theory taking into account these aspects was developed in recent years [41–43]. It was demonstrated that the trARPES signal is given by the following expression:

$$I_k(\omega, t_0) = \mathrm{Im} \int dt \int dt'\, s_{t_0}(t) s_{t_0}(t') e^{i\omega(t-t')} G^<_k(t, t'), \tag{5}$$

where now the intensity depends on the time $t_0$ at which the probe pulse is centred. The function $s_{t_0}(t)$ describes the finite-time width of the probe pulse and can be be taken for example to be a gaussian centred in $t_0$. The nonequilibrium expression Eq. (5) reduces to the expression at equilibrium Eq. (4) if two conditions are satisfied. First, if the lesser Green's function depends only on the difference of its two arguments – that is, either at equilibrium or in a stationary steady state. Second, if we can take $s_{t_0}(t) = 1$ as it is appropriate for equilibrium measurements which are performed with a continuos beam. It is also interesting to consider the opposite, unphysical

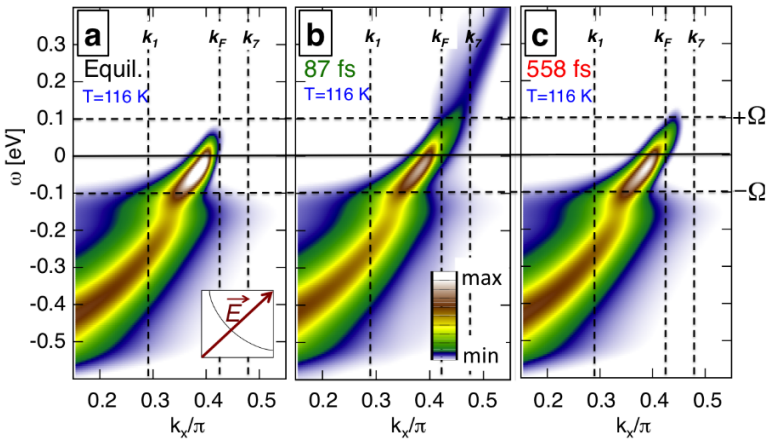


Figure 13: trARPES spectra at various times: in equilibrium (a), just after the pump (b) and long after the pump (c). (From Ref. [40])

extreme of an infinitely narrow probe pulse $s_{t_0}(t) = \delta(t - t_0)$. In this case Eq. (5) gives $I_k(\omega, t_0) = G^<_k(t_0, t_0)$, i. e. the occupancy at a given time of the electron with momentum k, independently of its energy. This is clearly due to the fact that an infinitely narrow pulse has a flat spectrum of frequencies.

After the first applications of this theory on toy models such as the Falikov-Kimball model [42] it is now becoming possible to use this formalism to perform realistic simulations of the experimental spectra [44], as shown in FIGURE 13.

## 2.5 AMPLITUDE MODE IN SUPERCONDUCTORS

Beside the use as a tool to investigate the basic interaction processes in solids, these ultrafast time-resolved techniques may be used to trigger macroscopic coherent oscillations of specific modes. Particularly important in this context is the possibility of directly observing the collective amplitude – or *Higgs* – mode of the superconducting order parameter. This mode corresponds to the oscillation of the modulus of the order parameter $|\Delta|$ [45].

In principle, two main obstacles should impede the excitation and the observation of this mode: (i) its frequency resonates with the energy necessary to break Cooper pairs, resulting in a strong damping of the mode itself and (ii) it does not couple directly to electromagnetic fields in the linear response regime. A special case is when the superconductivity coexists with the charge-density-wave (CDW) order, as in this case the effective energy necessary to inject electron–hole excitations is larger than $2\Delta$, avoiding the strong overdamping of the Higgs mode. Indeed, a collective mode attributed to the Higgs was recently measured in $NbSe_2$ through Raman scattering [47].

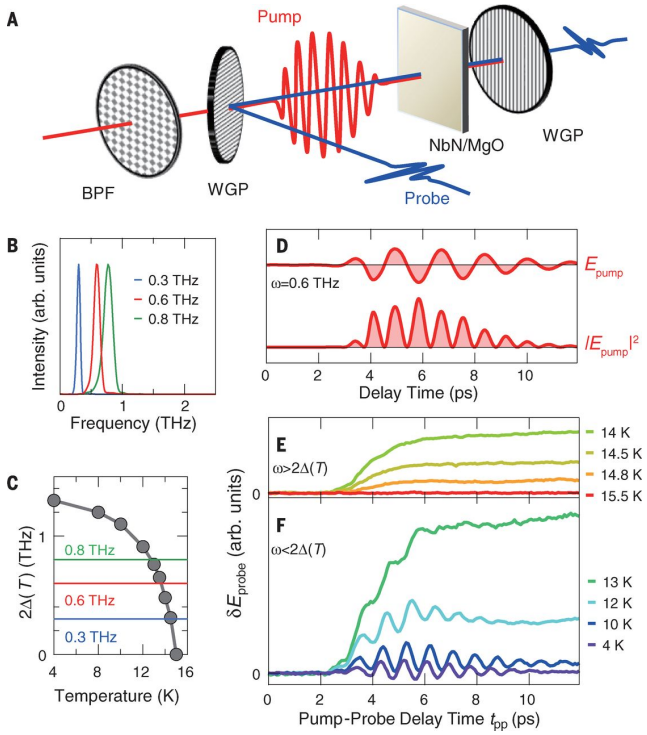


Figure 14: Schematic experimental setup for the observation of the amplitude mode in conventional superconductors.(From Ref. [46]

These results triggered an effort toward the time-domain investigation of the amplitude mode in conventional s-wave superconductors, whose hallmark should be an oscillation of the gap edge at twice the gap frequency. The direct detection of this mode could be achieved via either trARPES or optical spectroscopy in the gap energy range (THz). Moreover, the collective oscillatory response in the optical conductivity can be resonantly enhanced by tuning the frequency of the order-parameter oscillations to the energy of an optical phonon mode that is coupled to the superconducting amplitude mode.

Unfortunately, the main problem in designing such a time-domain experiment is related to the excitation process. This problem was recently solved by employing a sub-gap THz excitation scheme, in which the intensity of the pump pulse is strong enough to non-linearly couple to the superconducting condensate, thus exciting the amplitude mode beyond the linear response regime. In this way, time-domain oscillations at the frequency $2\Delta$ were reported in films of the conventional superconductor $Nb_{1-x}Ti_xN$ [48]. Moreover, it was demonstrated the resonant excitation of collective modes in NbN via non-linear excitation. The superconducting nature of the resonance has been demonstrated by the occurrence of a large third-harmonic generation when the frequency of the pulse matches the value of the superconducting gap [46].

# 3

# NONEQUILIBRIUM PAIRING IN COLD ATOMS

The developments in the field of ultracold atoms have rejuvenated the field of nonequilibrium superconductivity in the last few years, in parallel with the advances of time-resolved spectroscopies. Systems of ultracold atoms trapped by light can play the role of quantum simulators [49] because they can safely be assumed as isolated quantum systems and they can be described in terms of simple Hamiltonians, whose parameters can be controlled and manipulated with an unprecedented accuracy. This allows to simulate paradigmatic models in which the constituents only experience controlled short-ranged interactions, in the absence of undesired defects or other interactions which are inevitably present in actual materials.

The field has achieved countless milestones, starting from the observation of a condensate of bosons (BEC) and the realization of BCS pairing in fermions [50], which is particularly relevant for the subject of the present thesis. Of course, since the constituents of these systems are neutral atoms, their pairing gives rise to a "superfluid" – more than "superconducting" – states of matter.

What makes cold-atom systems so appealing is also the possibility to tune their inter-particle interactions via Feshbach resonance. For example, this makes possible to study the BCS to BEC crossover, by varying continuously the strength of the mutual interaction of a system of fermions [51]. Moreover, this control can be also used to change the interaction at a given time, thus performing in a real system the theoretical scheme known as "quantum quench": an abrupt change of the interaction from some initial to some final value. This is one of the simplest ways to study a system driven out of equilibrium. As we mentioned above cold atoms allow to study quantum quenches for almost perfectly isolated systems in the absence of impurities. Last, but not least, the characteristic timescales are much longer than in solids and typically in the range of milliseconds, making it much easier to track the time evolution and to study the quantum dynamics.

Here we review some recent activity on the quantum quench of s-wave superfluids, which are clearly important for the rest of the thesis. Indeed in the following we will compare these results with our calculations for a superconductor with d-wave symmetry in order to highlight the role played in the relaxation dynamics by its unconventional symmetry and the resulting nodal lines.

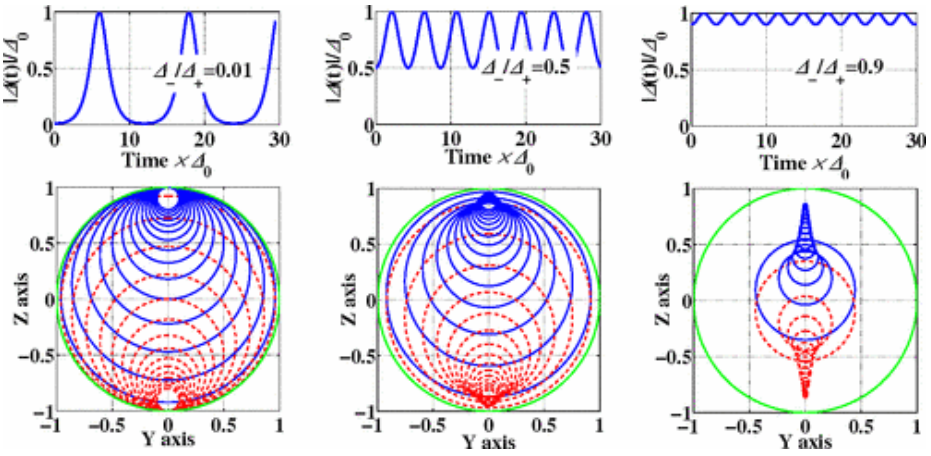


Figure 15: Coherent BCS dynamics. Above: the soliton solutions for the dynamics of the order parameter $\Delta$. Below: trajectories on the projected Bloch sphere for selected momenta. On the $z$ axes the average occupation of the states with the given momentum ($z$ component of the Anderson pseudospin), and on the $x$ axes the anomalous component ($x$ component of the Anderson pseudospin) (From Ref. [53]).

### QUANTUM QUENCHES IN COLD-ATOM FERMI GASES

In recent years there have been a renewed interest on the subject of a BCS condenstate perturbed from its equilibrium state. Early works on the subject include the important result of Volkov and Kogan (1974) [52] who studied the small deviations from equilibrium using linearized equations of motion and found that the gap of a slightly perturbed superconductor recovers with an oscillatory dynamics damped by a characteristic power law $\frac{1}{\sqrt{t}}$ [52].

This was followed much more recently by a considerable amount of new results [53–56]. A first important work by Barankov et al. (2004) [53] addressed the problem of an abrupt raise of the attractive interaction in an otherwise very weakly paired system. It was found that the system responds with characteristic anharmonic, solitonic oscillations of the gap (FIGURE 15). Theoretical analysis, supported by numerical simulations, predicts a stage of exponential growth, described by BCS instability of the unpaired Fermi gas, followed by periodic oscillations described by collisionless nonlinear BCS dynamics.

In the so-called collisionless approximation, the appropriate Hamiltonian to describe these systems is the BCS Hamiltonian:

$$\mathcal{H} = \sum_{k} \epsilon_{k\sigma} c^{\dagger}_{k\sigma} c_{k\sigma} - \lambda \sum_{kp} c^{\dagger}_{k\uparrow} c^{\dagger}_{-k\downarrow} c_{-p\downarrow} c_{p\uparrow}, \tag{6}$$

and a crucial result is that this model Hamiltonian is integrable, in the sense that it admits a number of integrals of motions which is equal to the number of its degrees of freedom. These integrals of motion can be explicitly obtained via a mathematical construction based on the

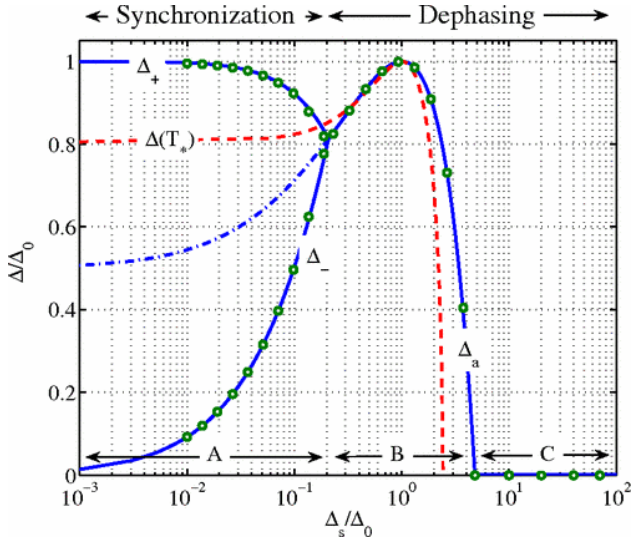


Figure 16: Three regimes of the pairing dynamics as a function of the gap parameter (in the figure denoted $\frac{\Delta_s}{\Delta_0}$. In the phase A (synchronization) the time-dependent gap oscillates indefinitely between the curves marked with $\Delta_+$ and $\Delta_-$, the dotted curve being their average. In the other two phases it reaches a non-zero (B) or a vanishing (C) stationary value. The red curve represents the thermal value given by the energy of the corresponding excited state. (From Ref. [55]).

so-called "Lax vector" [56]. This mathematical property is reflected on a physical effect: an effective reduction in the number of degrees of freedom which, in certain circumstances, results in an oscillatory time dependence with predictable characteristics.

The mean-field character of the Hamiltonian (6) is not a sufficient condition to be able to exactly predict its dynamical behavior. A major role is also played by the effective one-dimensionality of the problem, i. e. the possibility of rewriting the Hamiltonian in terms of operators labeled by only one continuos variable – the energy $\epsilon$ in this case. The isotropic interaction makes this possibility evident in Eq. (6). However, it is interesting that the same property can indeed be shown to be valid for other symmetries than s-wave, such as $p + ip$ and $d + id$-wave [57, 58]. The key-point in these cases is that despite their unconventional symmetry, the *modulus* of the superconducting order parameter is isotropic.

In the case of $d_{x^2-y^2}$ the modulus of the order parameter is not isotropic, this makes the Hamiltonian intrinsically multi-dimensional and, while still a mean-field Hamiltonian, the construction of the integrals of motion cannot proceed as a straightforward generalization of the previous symmetries. As we are going to see in the next chapters, this has important consequences on the dynamics of such an anisotropic model.

The approach based on the integrability of the *s*-wave model can be extended to the whole range of possible quenches from interaction $\lambda_i$ to interaction $\lambda_f$. This results in a predictability of the state of the system at large times based on the integrability of the underlying BCS model. This allows to map out the full quantum quench "phase diagram" for weakly coupled *s*-wave BCS superconductors (see FIGURE 16). Remarkably, it was found that as long as we stay in the weak-coupling regime $W \ll \Delta$ then the general feature of the dynamics are determined by the ratio $\frac{\Delta^i}{\Delta^f}$ between the *equilibrium* values of the gap for the given interactions. In particular, it was found that, depending on this value, the system may display three different "dynamical regimes":

1. Persistent oscillations,
2. Damped oscillations,
3. Exponential decay.

It was also possible to find analytical expressions for the "critical" values of the quench parameters. The first regime was found up to $\frac{\Delta^i}{\Delta^f} = e^{-\frac{\pi}{2}} \simeq 0.2$. When $\frac{\Delta^i}{\Delta^f}$ is larger, but still less than $e^{\frac{\pi}{2}} \simeq 4.8$ the system has damped oscillations which asymptotes to a stationary value different from zero. It was found that these oscillations have a power-law decay of $\frac{1}{\sqrt{t}}$ therefore extending the result of Ref. [52]. While in the regime of persistent oscillations the phases of the single sectors in $k$ space are locked to a same value, in this regime the phases are different, in particular they evolve from zero to finite and time-dependent values. Because of the particle-hole symmetry of the problem, which is assured in the weak-coupling regime, the imaginary part of these oscillations cancel out when summing over all the momenta. However, this sum leads also to dephasing and ultimately to the decay of the oscillations. Finally, the third regime was found for $\frac{\Delta^i}{\Delta^f} > e^{\frac{\pi}{2}} \simeq 4.8$ with an exponentially fast decay of the initial gap to zero, similar to a switch-off of the BCS interaction.

A common and important feature is that, even if the gap reaches a stationary value, the whole system persists in a nonequilibrium state and does not relax. This is particularly relevant for example in the third regime in which the zero gap does not mean that the system is in the unpaired state. Indeed, in the absence of collisions the system is trapped in a nonthermal state. With this respect, it is remarkable the appearance of a small window of quenches around $\frac{\Delta^i}{\Delta^f} \simeq e^{\frac{\pi}{2}}$ for which the steady value of the gap is finite and its thermal value, which is expected to be obtained in presence of collisions, is zero. This means that the system is trapped in a nonthermal broken-symmetry phase, as also pointed out in other similar studies [59].

Another remarkable example of this is given in the context of the topological $p + ip$ superfluid [57]. In this case the dynamics of the

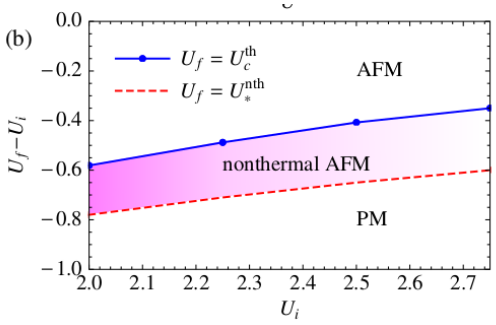


Figure 17: Nonthermal antiferromagnetic state [59].

order parameter is also exactly solvable and the three regimes similar to Fig. (16) are found. This is because the $p + ip$ symmetry can be basically obtained by a phase $e^{i\phi_k}$ which in some treatments can be gauged away therefore retrieving a s-wave like Hamiltonian. The point of this work is that for this system there exists a quantum phase transition between a topologically non trivial BCS state and a topologically trivial BEC state. This means that in the former phase there are gapless edge states which are absent in the latter phase. Ultimately, this is due to the spin-triplet nature of the $p + ip$ superfluid phase.

It was shown that there are two so-called "winding numbers" which describe this topology, one is associated with the pseudo-spin texture and the other with the retarded Green's function. When the system is at equilibrium these two coincide. When the system is driven out of equilibrium they do not in general. In particular, the pseudo-spin texture depends of course on the initial condition and it is found that the winding number associated with it is a conserved quantity. On the other hand the retarded Green's function depends only on the effective Hamiltonian, being related to the spectral function and not to the occupancies. In particular, when the system reaches a stationary state for the mean-field and therefore for the mean-field Hamiltonian, then the retarded Green's function is again time translational invariant and exactly the same of a system at equilibrium with that Hamiltonian. Hence, this is a clear example of how two coinciding concepts at equilibrium may become quite different when studied out of equilibrium, and how one should be careful in generalizing concepts and relations which are known to be valid for equilibrium quantities.

# Part II

# d-WAVE SYMMETRY

# 4

# TIME-DEPENDENT MEAN-FIELD DYNAMICS OF SUPERCONDUCTORS

As discussed in the first part, the subject of d-wave superconductivity is intimately related to the high-temperature cuprate superconductors which, however, display many other "unconventional" properties with respect to normal metals and superconductors. It is clear that the complex response of high-temperature superconductors driven out of equilibrium will be influenced by the many intertwined aspects of the physics of these materials. Precisely for this reason, we find it important to disentangle as much as possible the contributions of the different "uncoventional" properties. Therefore in this part we focus on the consequences of the d-wave symmetry in the overall dinamycs and in the different quasiparticle properties in the nodal and antinodal regions. This is why, to highlight these effects, we choose a minimal model for a d-wave superconductor which does not include any other ingredient of the cuprate physics such as: pseudogap, Mott physics, spin fluctuations, deviations from Fermi-liquid.

As we shall discuss, our simplified model can indeed help to discuss some features of pump and probe photoemission experiments, suggesting that the key ingredient behind this physics is the very existence of nodal lines for the gap function.

In the following we discuss the main properties of the Hamiltonian under study, and underline the similarities and the differences with analogous models with isotropic gap.

## 4.1 MODEL HAMILTONIAN

We consider a BCS model with an attractive interaction separable in the space of momenta. This means that the interaction term only depends on two momenta, as opposed to the three independent momenta of a generic interaction, and that this dependence is factorized and described by a single function with a given momentum dependence $\gamma_k$, which we will call the "structure factor" of the interaction. The Hamiltonian therefore reads:

$$\mathcal{H} = \sum_{k\sigma} \epsilon_k c^\dagger_{k\sigma} c_{k\sigma} - \lambda \sum_{kp} \gamma_k \gamma^*_p c^\dagger_{k\uparrow} c^\dagger_{-k\downarrow} c_{-p\downarrow} c_{p\uparrow}, \tag{7}$$

where $c^\dagger_{k\sigma}$ is the creation operator of electrons with momentum $k$, spin projection $\sigma$ and kinetic energy $\epsilon_k$, and the strenght of the interaction is $\lambda > 0$.

A well known characteristic of this model is that, in the thermodynamic limit we are interested in, it is indeed equivalent to the mean-field Hamiltonian:

$$\mathcal{H}_{\mathrm{MF}} = \sum_{k\sigma} \epsilon_k c^\dagger_{k\sigma} c_{k\sigma}, - \sum_k (\Delta_k c^\dagger_{k\uparrow} c^\dagger_{-k\downarrow} + \Delta^*_k c_{-k\downarrow} c_{k\uparrow}), \tag{8a}$$

$$\Delta_k = \lambda \gamma_k \sum_p \gamma^*_p \left\langle c_{-p\downarrow} c_{p\uparrow} \right\rangle, \tag{8b}$$

where the brackets $\langle\rangle$ indicate the quantum average of the enclosed operators and $\Delta_k$ is the superconducting gap parameter, which is non-zero in the superconducting phase and whose absolute value sets the minimum energy of a quasi-particle excitation with momentum $k$.

If $\Delta_k$ depends only on the modulus $|k|$, the gap is said to be *isotropic* whereas if it depends also on the orientation of momentum it is said to be *anisotropic*. Moreover, a *nodal line* in momentum space is a curve along which $\Delta_k = 0$ even if the system is in the superconducting phase.

In the case $\gamma_k = 1$, Eq. (7) is the original BCS model whose ground state describes a superconductor with isotropic gap [3]. This Hamiltonian, in particular the attractive interaction, may be derived starting from an electron-phonon interaction, as in the original BCS work, or from the attractive Hubbard model with a mean-field decoupling in the particle-particle channel. Moreover, both Hamiltonians (7) and (8) are indeed used in many other theoretical physics contexts, going often under the name of Richardson model [60], especially when taken in the case of finite systems, for which a solution in terms of Bethe ansatz is possible [61, 62].

Here we are interested in the case $\gamma_k$ is a function with a symmetry of the $d$ type. This means that $\gamma_k$ belongs to some irreducible representation of the point group symmetry of the Hamiltonian with a $d$ character. Examples of such functions are $\gamma_k = \cos k_x - \cos k_y$ on a square lattice and $\gamma_k = k_x^2 - k_y^2$ on the two dimensional plane. The latter actually belongs to the set of the spherical harmonic functions, which describe the angular dependence of the orbitals of hydrogenic atoms and whose classification in $s$, $p$, $d$-wave states and so on is borrowed in this context.

An example of Hamiltonian with $d$-wave symmetry, much used in the context of cuprates [11, 13, 14], is the $t - J$ model:

$$\mathcal{H} = -t \sum_{ij\sigma} P_i c^\dagger_{i\sigma} c_{j\sigma} P_j + \frac{J}{4} \sum_{ij} (\hat{\sigma}_i \cdot \hat{\sigma}_j - n_i n_j) - \mu \sum_i n_i, \tag{9}$$

which describes electrons hopping on a square lattice in such a way to avoid the contemporary presence of two of them on the same site, and interacting with a spin-spin antiferromagnetic ($J > 0$) interaction

acting on neighbouring sites. Among the terms obtained expressing the interaction term of Eq. (9) in momentum space, we focus on:

$$\sum_{kpq} V_{k-p} c^{\dagger}_{k\uparrow} c^{\dagger}_{p+q\downarrow} c_{k+q\downarrow} c_{p\uparrow}, \tag{10}$$

where $V_k$ is proportional to $\cos k_x + \cos k_y$, reflecting the nearest-neighbour character of the interaction. The possible gap symmetries are given by the decomposition of $V_{k-p}$ in irreducible representations of the point group symmetry of the square:

$$\begin{aligned} V_{k-p} = & \\ & \underbrace{(\cos k_x + \cos k_y)(\cos p_x + \cos p_y)}_{\Gamma_s} + \\ & \underbrace{(\cos k_x - \cos k_y)(\cos p_x - \cos p_y)}_{\Gamma_{d1}} + \\ & \underbrace{(\sin k_x + i \sin k_y)(\sin p_x - i \sin p_y) + \text{c.c.}}_{\Gamma_p} \end{aligned} \tag{11}$$

The system can in principle have superconducting instabilities in these different channels. In the absence of other interaction terms, the dispersion selects the dominant instability through the corresponding density of states. It can be shown that the d-wave instability is the leading one as long as the density of states has not peculiar energy structures. Under these generic circumstances, after a simple mean-fied decoupling one finally obtains the Hamiltonian (8).

In the following we will consider the simplest realization of such d-wave symmetry in a continuum system. This is motivated by our interest in the general consequences of an anisotropic gap with nodal lines, rather than on the specific realizations. We have explicitly verified that the results do not depend on this choice by comparing with a lattice version of the same Hamiltonian, which can be obtained through the above mentioned mean-field decoupling of the Heisenberg term of the $t - J$ model.

In the calculations we present, we consider the Hamiltonian (8) on the two dimensional plane with a parabolic dispersion characteristic of electrons in free space:

$$\epsilon_k = t|k|^2 - \mu \qquad \gamma_k = \frac{k_x^2 - k_y^2}{|k|^2} = \cos 2\phi_k, \tag{12}$$

where $\mu$ is the chemical potential, $\phi_k$ is the polar angle and $|k|$ is the modulus of the momentum, bounded by a certain cut-off $\Lambda$ which mimicks the existence of a lattice.

It can be practically convenient to impose particle-hole symmetry, which is simply realized by choosing the value of the chemical potential to make the density of states $D(\epsilon) = \sum_k \delta(\epsilon - \epsilon_k)$ symmetric

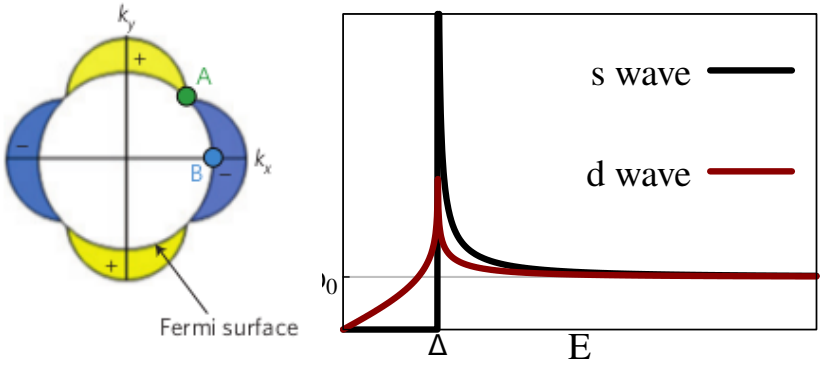


Figure 18: Left: Two dimensional k-space with the circular Fermi surface and the schematic of the d-wave gap, which vanishes at the node (A), is maximum at the antinode (B) and changes sign by rotation of $\frac{\pi}{2}$. (Fig. from Ref. [63]). Right: DOS of quasiparticle excitations. For a fully gapped system, as the s-wave superconductor, the DOS is zero below the gap (black curve). On the other hand, the d-wave superconductor has non-zero DOS for arbitrary low energies (red).

around the chemical potential itself. This implies $\mu = \frac{t\Lambda^2}{2} = W$. The value of $\Lambda$ has no influence as long as the weak-coupling condition $\lambda \ll W$ is satisfied. Since the band energy $\epsilon_k$ depends only on $|k|$ it is useful to use the angle and the amplitude of the momentum vector $(\epsilon, \phi)$ as independent variables instead of $(k_x, k_y)$.

The structure factor $\gamma_k$ vanishes for $\phi_k = (2n+1)\frac{\pi}{4}$ with integer $n$, i. e. along the bisectrices of the four quadrants of the momentum space ($k_x = \pm k_y$, see FIGURE 18). These are the characteristic nodal lines we discussed above.

The solution of this model follows exactly the standard solution of the s-wave BCS model, and we detail it in APPENDIX A. The basic result is that we obtain a gapped quasiparticle dispersion $E_k = \sqrt{\epsilon_k^2 + |\Delta_k|^2}$, where $\Delta_k \propto \gamma_k$. This implies that, in contrast with the s-wave case, where $\Delta_k$ is a constant in momentum space, a vanishing excitation energy is found when $\epsilon_k = \Delta_k = 0$, i.e., when the Fermi surface crosses the nodal lines $k_x = \pm k_y$. In other words the superconductor has gapless excitations in a few points of the Fermi surface.

The existence of zero- (and low-) energy excitations is reflected in the form of the density of states shown in FIGURE 18, where the sharp gap of s-wave superconductors in replaced by a linear dependence $D(\epsilon) \propto \epsilon$ for small energies, even if sharp features still survive at the gap edges $\pm\Delta$. The existence of nodal lines and low-energy excitations clearly influences the response of the system to external stimuli. In the next chapter we will show that their effect on the non-equilibrium dynamics can be important both from a quantitative and a qualitative point of view.

However, before tackling the direct study of the dynamics, we find it important to review some general properties of the Hamiltonians (7) and (8) regardless of the isotropic or anisotropic interaction.

## 4.2 COLLISIONLESS APPROXIMATION

In this section we review the relation between a general model of interacting particles and our BCS Hamiltonian. As we discussed above, the BCS Hamiltonian Eq. (7) has a mean-field character, which can be derived from a generic interaction in the so-called "collisionless approximation", whose nature and meaning is discussed here. In our context this is an important point because the absence of collisions is referred to: no collision *but* between pairs of electrons forming the Cooper pairs, the ubiquitos elements of superconductors.

More precisely, the BCS model of Eq. (7) is equivalent to its mean-field formulation (8) in the thermodynamic limit. Without entering an extremely vast field [61] we present a pictorial argument to highlight the phsyical content of this observation. Indeed Eq. (8) can be rewritten:

$$\mathcal{H} = \sum_{k\sigma} \epsilon_k c^\dagger_{k\sigma} c_{k\sigma} - \lambda \Phi^\dagger \Phi, \tag{13}$$

where $\Phi = \sum_k \gamma_k c_{-k\downarrow} c_{k\uparrow}$ is a *macroscopic* operator in the sense that it is the sum of a macroscopic number of operators and therefore its average is less subject to quantum fluctuations and we can replace it with its average. This is clearly a consequence of the factorized form of the interaction.

Another way to visualize the mean-field nature of the problem is to perform an inverse Fourier transform to express Eq. (7) in real space obtainina:g

$$\mathcal{H} = -t \sum_{ij\sigma} c^\dagger_{i\sigma} c_{j\sigma} - \lambda \sum_{ijmn} \gamma_{im} \gamma^*_{jn} c^\dagger_{i\uparrow} c^\dagger_{m\downarrow} c_{j\downarrow} c_{n\uparrow}, \tag{14}$$

where $\gamma_{ij} = \sum_k \gamma_k e^{ik(R_i - R_j)}$. In Eq. (14) while the first sum is restricted as usual to nearest neighbours, the second sum is unrestricted, therefore describing an infinitely long ranged interaction not decaying with distance. It is well known from statistical mechanics that such kind of models are actually mean-field models where the constituents interact with an infinite number of partners, which implies in turn that each of them interacts with an average field created by the others. In the s-wave case $\gamma_{ij} = \delta_{ij}$ and this assumes the inspiring picture of a long-ranged pair hopping term. In the case of d-wave these long-ranged hopping has some structure in real-space, but the physical picture is unchanged.

This is exactly what is usually referred to as a mean-field model in which (unrealistically) all the microscopic constituents interact with

each other. From a physical point of view, the infinite range of the hopping can be seen as related to the presence of the condensate and of the long-range order.

It is interesting to stress two consequences of this simple properties:

1. Our BCS Hamiltonian can be obtained as a mean-field approximation of models with short-ranged interaction like the t-J model. This shows explicitly that the mean-field approximation actually amounts to start with a finite-range interaction (in this specific case an extremely short-range one) and transform it into an infinite-range interaction.

2. The Hamiltonian is therefore not local in real space. This can have important consequences on the relaxation dynamics. Indeed, it has been shown that local observables necessarily relax at long times in models with local Hamiltonian. From this point of view, the persistent oscillations of the s-wave system presented in CHAPTER 3 may seem mysterious. However, the apparent contradiction is resolved once one realizes that indeed the real-space representation of the BCS Hamiltonian is non local. On the other hand, we will see that the gap of a d-wave superconductor always relaxes. However, the cause of this relaxation is due to its anisotropy and to the resulting nodal lines – not to the different range of the interaction.

We now turn to the collisionless approximation. The arguments we discuss in the following are indeed independent on the symmetry of the interaction. First a rather general consideration is that the entire Hilbert space, or more precisely the Fock space of the model can be expressed as the product of the following kind:

$$\mathbb{H} = \prod_k \mathbb{H}_k, \tag{15}$$

$$\mathbb{H}_k = \{|0\rangle\,,\ |k\uparrow\rangle\,,\ |{-k}\downarrow\rangle\,,\ |k\uparrow,{-k}\downarrow\rangle\}, \tag{16}$$

that is the product of Hilbert spaces "local" in reciprocal space. For each momentum $k$, these include one state in which only an electron with momentum $k$ and spin up is present, one in which the only electron present is with opposite momentum and spin, one in which both are present and one in which neither are present. The mean-field, or "collisionless" condition is therefore expressed as:

- The subspaces $\mathbb{H}_k$ and $\mathbb{H}_p$ for different momenta are coupled only through the mean-field $\Delta$ and
- For each $\mathbb{H}_k$ the sub-subspaces $\{|0\rangle\,,\ |k\uparrow,{-k}\downarrow\rangle\}$ and $\{|k\uparrow\rangle\,,|{-k}\downarrow\rangle\}$ are decoupled.

In particular this means that if at some time the state of the system is in the subspace $\{|0\rangle\,,\ |\uparrow\downarrow\rangle\}$, then it will remain in this subspace at all

the following times. This is important for it clearly holds also if the system is out of equilibrium, as long as the Hamiltonian has the same functional form of Eq. (7) or (8).

Since the different $\mathbb{H}_k$ are coupled only through the mean field, it makes sense for a moment just to analyze one given $k$. For a given $k$ we can rename the space with the substitution $|k\uparrow\rangle \to |\uparrow\rangle$, $|-k\downarrow\rangle \to |\downarrow\rangle$ and $|k\uparrow, -k\downarrow\rangle \to |\uparrow\downarrow\rangle$ or in other words let us consider only the spin. The most general state in this Hilbert space is:

$$|\Psi\rangle = \alpha|0\rangle + \beta|\uparrow\rangle + \gamma|\downarrow\rangle + \delta|\uparrow\downarrow\rangle, \tag{17}$$

$$|\alpha|^2 + |\beta|^2 + |\gamma|^2 + |\delta|^2 + = 1. \tag{18}$$

Now, the average occupancy of the spin up state is $|\beta|^2 + |\delta|^2$ and is maximum for $\alpha = \gamma = 0$. The anomalous term is given by $\alpha^*\delta$ and has its maximum for $\beta = \gamma = 0$ and $|\alpha| = |\delta| = \frac{1}{\sqrt{2}}$. This is the reason why the dimensionless superconducting order parameter $\frac{\Delta}{\lambda}$ has a maximum value of $\frac{1}{2}$.

At this point, it is rather natural to introduce a set of operators originally introduced by Anderson [64] which define what is usually called an Anderson's pseudospin:

$$s_{kx} = \frac{c^\dagger_{k\uparrow}c^\dagger_{-k\downarrow} + c_{-k\downarrow}c_{k\uparrow}}{2}, \tag{19a}$$

$$s_{ky} = \frac{c^\dagger_{k\uparrow}c^\dagger_{-k\downarrow} - c_{-k\downarrow}c_{k\uparrow}}{2i}, \tag{19b}$$

$$s_{kz} = \frac{c^\dagger_{k\uparrow}c_{k\uparrow} - c_{-k\downarrow}c^\dagger_{-k\downarrow}}{2}, \tag{19c}$$

$$s^\pm_k = s_{kx} \pm i s_{ky}. \tag{19d}$$

The fundamental property and the reason for the name comes from the fact that, as it is easily confirmed, these operators have the same commutation rules of the angular momentum, which is, the same of a physical spin:

$$[s_{ka}, s_{k'b}] = i\delta_{kk'}\epsilon_{abs}s_{kc} \qquad a, b, c = x, y, z. \tag{20}$$

With these operators our BCS model EQUATION 7 can be cast in this way:

$$\mathcal{H} = 2\sum_k \epsilon_k s_{kz} - \lambda \sum_{kp} \gamma_k \gamma^*_p s^+_k s^-_p, \tag{21a}$$

$$\mathcal{H}_{MF} = 2\sum_k \epsilon_k s_{kz} - \sum_{kp} (\Delta_k s^+_k + \Delta^*_k s^-_k), \tag{21b}$$

$$\Delta_k = \gamma_k \sum_p \gamma^*_p \langle s^-_p \rangle. \tag{21c}$$

It is also easy to verify that the mean-field Hamiltonian Eq. (21) commutes with the sum of the squares of the pseudospin operators $\langle|\vec{s}_k|^2\rangle =$

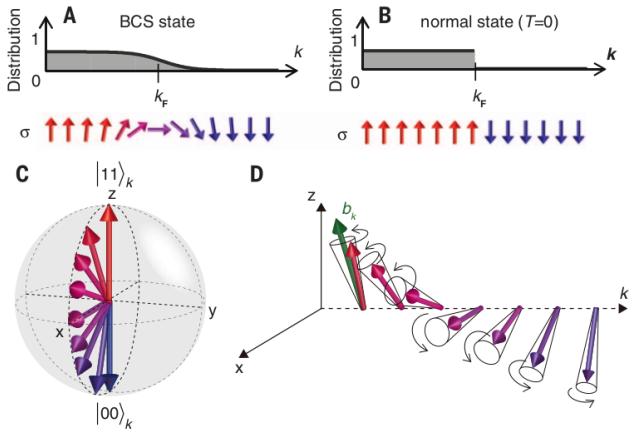


Figure 19: (A and B) Schematics of the electron distribution represented by Anderson's pseudospins for the normal state at $T = 0$ and for the BCS state, respectively. (C) The pseudospins mapped on the Bloch sphere. (D) A schematic picture of the pseudospin precession. (From Ref. [46]

$\langle s_{kx}^2 \rangle + \langle s_{ky}^2 \rangle + \langle s_{kz}^2 \rangle = \text{const.}$, which obviously implies that in the collisionless approximation the norm of the Anderson's pseudospin is a conserved quantity.

Within the pseudospin representation, a Fermi-liquid is characterized by an "up" pseudospin for all momenta below the Fermi momentum, and a "down" momentum above it. Therefore a sharp edge separates two ferromagnetic regions with opposite momenta. For a superconductor instead the states around the Fermi level are modified in such a way that the magnetization smoothly evolves from up to down. This is clearly the translation in the pseudospin language of the opening of the gap (see FIGURE 19).

Finally, it is also very convenient to introduce the so-called Nambu spinor:

$$\gamma_k = \begin{pmatrix} c_{k\uparrow} \\ c^\dagger_{-k\downarrow} \end{pmatrix}, \qquad s_{k\alpha} = \gamma^\dagger_k \frac{\vec{\sigma}}{2} \gamma_k, \tag{22}$$

in terms of which the Hamiltonian Eq. (8) reads:

$$\mathcal{H}_{MF} = \sum_k \gamma^\dagger_k \hat{H}_k \gamma_k, \tag{23a}$$

$$\hat{H}_k = \begin{pmatrix} \epsilon_k & -\Delta_k \\ -\Delta^*_k & -\epsilon_k \end{pmatrix} = \epsilon_k \hat{\sigma}_3 - \Delta'_k \hat{\sigma}_1 + \Delta''_k \hat{\sigma}_2, \tag{23b}$$

this form is very useful because it is somehow explicitely quadratic in the operators $\gamma_k$. This, together with the special properties of the Pauli matrices, provide very powerful means to handle the properties of the Hamiltonian, as we describe in detail in APPENDIX A.

## 4.3 BLOCH EQUATIONS OF MOTION

We now briefly introduce the equations of motion for the mean-field amplitudes, which are known as Bloch equations. Once again, these equations do not depend on the symmetry of the potential (and therefore of the gap).

We return to the Hamiltonian (7):

$$\mathcal{H} = \sum_{k\sigma} \epsilon_k c^\dagger_{k\sigma} c_{k\sigma}, -\lambda \sum_{kp} \gamma_k \gamma^*_p c^\dagger_{k\uparrow} c^\dagger_{-k\downarrow} c_{-p\downarrow} c_{p\uparrow}, \tag{24}$$

which has to be solved satisfying the self-consistency condition:

$$\Delta_k = \lambda \gamma_k \sum_p \gamma^*_p \left\langle c_{-p\downarrow} c_{p\uparrow} \right\rangle, \tag{25}$$

which expresses the fact that the mean-field experienced by the pairs is the effect of the same electrons and it can therefore be determined self consistently. The result can be readily obtained based on the static mean-field equations:

$$G^{(0)}_k = \langle c^\dagger_{k\sigma} c_{k\sigma} \rangle = \frac{1}{2}\left(1 - \frac{\epsilon_k}{E_k}\right), \tag{26a}$$

$$F^{(0)}_k = \langle c_{-k\downarrow} c_{k\uparrow} \rangle = \frac{\Delta_k}{2E_k}, \tag{26b}$$

where $E_k = \sqrt{\epsilon_k^2 + \Delta_k^2}$.

Clearly $G_k$ is real because it is the expectation value of of a Hermitian operator while $F_k$ is *a priori* complex but in the present case it can be taken to be also real without loss of generality. The equations of motion of these quantities are easily calculated as the average of the Heisenberg equations of motion of the operators $c^\dagger_{k\sigma} c_{k\sigma}$ and $c_{-k\downarrow} c_{k\uparrow}$:

$$i\dot{G}_k = \Delta^*_k F_k - \Delta_k F^*_k, \tag{27a}$$

$$i\dot{F}_k = 2\epsilon_k F_k + \Delta_k (2G_k - 1), \tag{27b}$$

$$\Delta_k = \gamma_k \sum_p \gamma^*_p F_p, \tag{27c}$$

where also the quantity $\Delta_k$ depends on time and it has to be calculated at each time while the system evolves. The form of $\Delta_k$ implies therefore that all the different momenta are coupled in their time evolution.

It appears immediately that if we start from the static (equilibrium) solution with a self consistent $\Delta_k$ the right-hand side of the above equations of motion vanishes, leading to a conservation of this quantities. Interesting phenomena can occur if the dynamics does not start from equilibrium conditions. A simple and popular protocol to drive

the system out of equilibrium is to prepare the system in the equilibrium conditions for a different vallue of the interaction with respect to the physical value which will control the unitary time evolution.

We want also to stress that, as we pointed out in CHAPTER 3, for the s wave case there is an exact solution for the dynamics due to the integrability of the corresponging model [54]. Without entering the mathematical details, the integrability of the mean-field model is a consequence of the collisionless approximation *plus* the fact that in the s wave case *both* the energy dispersion and the interaction depends only on the modulus of $|k|$ and therefore the problem can be recast into a one-dimensional problem for which powerful techniques such as the Bethe ansatz can be used [60–62].

Of course this is no longer possible for the d-wave symmetry, but it has been extended to other exotic order parameters. This is in particular the case of the topological $p + ip$-wave order parameter, with $\gamma_k = k_x + ik_y = |k|e^{i\phi_k}$. Here the excitation spectrum may vanish at most in one point [57], and it turns out that the Hamiltonian can be recast in a one-dimensional Richardson-Gaudin form with the transformation $c_{k\sigma} \to e^{i\phi_k} c_{k\sigma}$. The same idea can be used for the time-reversal breaking order parameter $d + id$-wave for which $\gamma_k = k_x^2 - k_y^2 + 2ik_x k_y = |k|^2 e^{2i\phi_k}$ and a spectrum which, again, can vanish at most in one point of the two-dimensional momentum space [58].

For the standard d-wave case we cannot map the model onto a one-dimensional system and we are not aware of similar ideas to simplify the calculations and to avoid the numerical solution of the equations of motion. In the next section we present these results as well as some approximate analytical calculations that we used to interpret and understand our results.

# 5

# DYNAMICS OF A GAP WITH NODAL LINES

In this chapter we present the results on the dynamics of the gap in a BCS d-wave superconductor after a quantum quench of the interaction [65]. We consider the mean-field Hamiltonian:

$$\mathcal{H}_{MF} = \sum_{k\sigma} \epsilon_k c^\dagger_{k\sigma} c_{k\sigma} - \sum_k (\Delta_k(t) c^\dagger_{k\uparrow} c^\dagger_{-k\downarrow} + \Delta^*_k c_{-k\downarrow} c_{k\uparrow}), \quad (28a)$$

$$\Delta_k = \lambda \gamma_k \sum_p \gamma^*_p \langle c_{-p\downarrow} c_{p\uparrow} \rangle , \quad (28b)$$

and the following configuration for the quantities $G_k(t) = \langle c^\dagger_{k\sigma}(t) c_{k\sigma}(t) \rangle$ and $F_k(t) = \langle c_{-k\downarrow}(t) c_{k\uparrow}(t) \rangle$ that define a superconducting state within mean-field theory:

$$G_k(0) = \frac{1}{2}\left(1 - \frac{\epsilon_k}{E^i_k}\right), \quad (29a)$$

$$F_k(0) = \frac{\Delta_i \gamma_k}{2E^i_k}, \quad (29b)$$

$$\Delta_i = \lambda^i \sum_p \gamma^*_p F_k(0), \quad (29c)$$

$$E^i_k = \sqrt{\epsilon^2_K + \Delta^2_i \gamma^2_k}. \quad (29d)$$

Then, we solve the Bloch equations of motion which follow from the Hamiltonian (28) with $\lambda^f \neq \lambda^i$:

$$i\dot{G}_k(t) = \gamma_k (\Delta(t))^* F_k(t) - \gamma_k \Delta(t) (F_k(t))^*, \quad (30a)$$

$$i\dot{F}_k(t) = 2\epsilon_k F_k(t) + \gamma_k \Delta(t)(2G_k(t) - 1), \quad (30b)$$

$$\Delta(t) = \lambda^f \sum_p \gamma^*_p F_p(t). \quad (30c)$$

The system of Eqs. (30) is a first-order nonlinear system of differential equations for the $2N_s$ quantities $\{G_k(t), F_k(t)\}$ with $N_s$ the number of points in our mesh of the reciprocal space. These equations have to be solved at the same time because they are all coupled to each other via the mean-field $\Delta(t)$. As discussed previously, for anisotropic models such as ours there is no analytical solution of the problem. That is why we resort to numerical integration of the Eqs. (30) using a Runge-Kutta algorithm at 4th order.

In the following we present the results of this calculation for the cases $\gamma_k = 1$ (*s*-wave) and $\gamma_k = \cos 2\phi_k$ (d-wave).

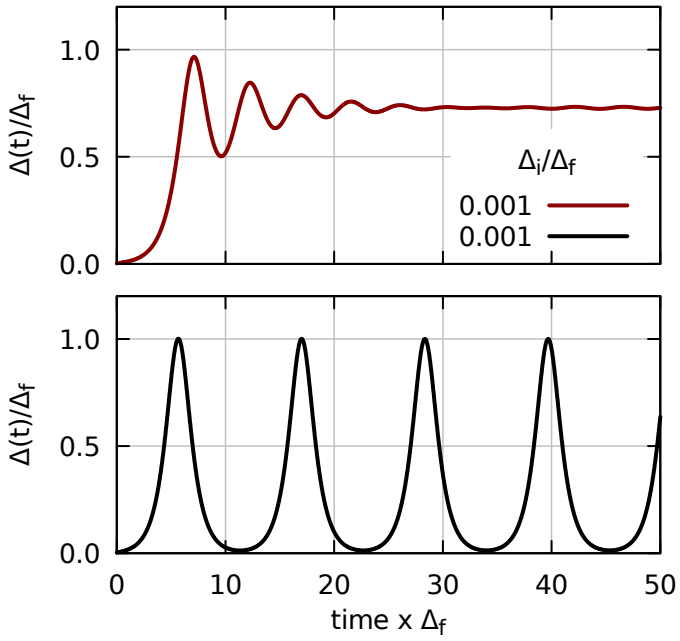


Figure 20: Gap dynamics following a quench from weak to strong interaction $\frac{\Delta_i}{\Delta_f} = 0.001$. In the d-wave superconductor (red) the gap is subject to a fast dephasing after a few oscillations. On the other hand, the s-wave superconductor (black) is in the regime of persistent oscillations.

## 5.1 DYNAMICS AFTER A SUDDEN EXCITATION

In this section we focus our attention on the dynamics of the quantity $\Delta(t) = \sum_k \gamma_k^* F_k(t)$ to which we refer to as the "gap" with a slight abuse of notation, since in the d-wave system the proper gap function is $\gamma_k \Delta(t)$. It is convenient to discuss the results in terms of a "quench parameter" given by the ratio $\frac{\Delta_i}{\Delta_f}$ which are the equilibrium gap values corresponding to the interactions $\lambda_i$ and $\lambda_f$.

The first observation is the *disappearance* of the solitonic regime of persistent oscillations characteristic of the s-wave model. This is shown in FIGURE 20 for a quench from weak to strong interaction. In this case the s-wave model is deep into the regime of undamped oscillations, whereas we find that the d-wave gap completes only a few oscillations before going to a stationary value different from zero.

Beside the physical effect of the nodal lines which give a fast dephasing, and which we discuss in deep in the following, we can identify the disappearance of the persistent oscillations as a characteristic features of anisotropic models. From the mathematical point of view, as we discussed in CHAPTER 3, the exact solution of the s-wave dynamics, from which one can find the solitonic solution, heavily relies on the isotropic gap. It is therefore at least reasonable to infer that the disappearance of the regime of persistent oscillations is related to the absence of an analytical solution of the anisotropic problem. From the

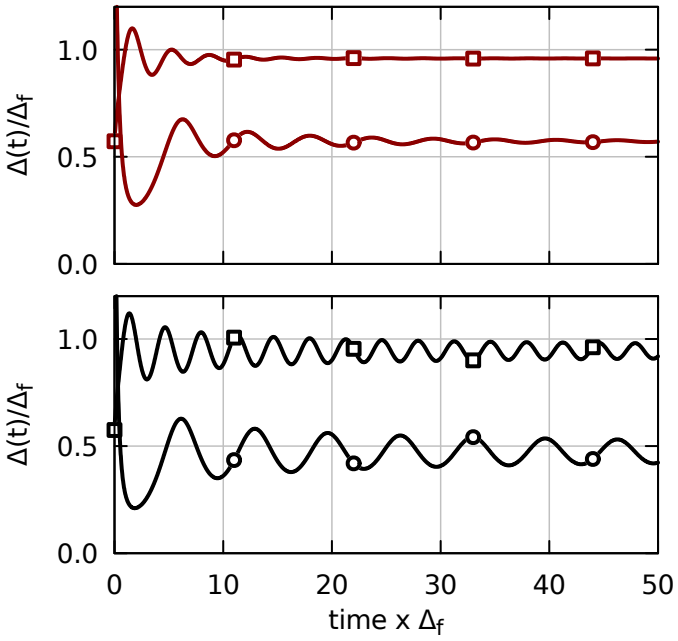


Figure 21: Comparison between d-wave (red) and s-wave (black) dynamics, for quenches of medium strenght: $\frac{\Delta_i}{\Delta_f} = 0.5$ (squares) and $\frac{\Delta_i}{\Delta_f} = 3.5$ (circles).

physical point of view, this means that there is not a regime with an effective reduction of the number of dynamical degrees of freedom and therefore that the dynamics can not be fully described in terms of just a few collective dynamical variables which lock in phase as in the soliton solution of the s-wave model.

In FIGURE 21 we plot the dynamics following two different quenches with quench parameter greater or less than one. For these parameters both the d- and the s-wave superconductors are in the regime of damped oscillations which asymptote to a non-zero stationary value. The important observation is that the d-wave gap (red) goes to the stationary value in shorter times with respect to the s-wave gap (black). Indeed, the s-wave gap has numerous coherent oscillations similarly to the previous regime also in this case. On the contrary, we can count only a few oscillations of the d-wave gap. In the following we give a precise characterization of this faster dynamics in terms of the exponent of the power-law associated to the decay of the oscillations.

It is important to emphasize that in the absence of pair-breaking scattering terms, the so-called "collisionless approximation" treated in CHAPTER 4, and of any real dissipation mechanism, the system persists in a nonequilibrium state even if the gap reaches a stationary value. In particular, for each momentum $k$ the functions $G_k(t)$ and $F_k(t)$ do not come to a steady state. The stationary value of the gap is reached only as a result of destructive interference, or dephasing, of different momentum sectors. From this point of view, the faster dynamics of the d-wave gap towards a stationary value is a clear

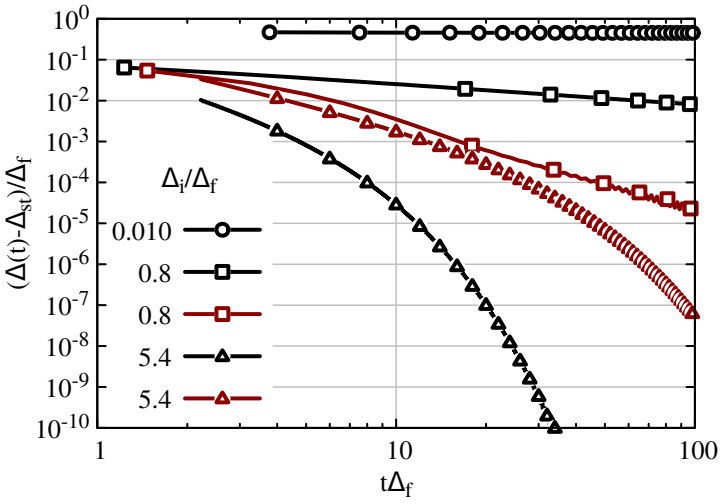


Figure 22: Different dynamical regimes. For selected values of $\frac{\Delta_i}{\Delta_f}$ shown in key, and for s (black) and d (red) symmetries, we plot in logarithmic scale the maxima of the absolute value of the deviation from the stationary gap, as a function of time. In the solitionic regime of the s-wave model (upper curve) we plot the maxima relative to the average of the oscillations.

evidence of the enhanced effectivness of this dephasing mechanism, which can be ascribed to the presence of the zero-energy modes along the nodal lines.

A clear way to visualize the various dynamical regimes and the difference between d-wave and s-wave is to plot in logarithmic scale the maxima and minima of the oscillations, relative to the stationary value reached at long times (FIGURE 22).

In the s-wave case we have three different behaviors related to the three dynamical regimes. The persistent oscillations give maxima which do not decay in time. The damped oscillations on the other hand have a characteristic power-law decay $\frac{1}{t^\alpha}$ which result in a linear behavior in the logarithmic plot. It is easy to extract the exponents associated to this decay. In the s-wave case we find the well-known exponent $\alpha = \frac{1}{2}$, whereas the d-wave case is found to exhibit an exponent $\alpha = 2$.

Finally, for quenches to very weak interactions, both models show an exponentially damped dynamics of the gap to a vanishing value. Indeed, in the limit of vanishing interaction we expect that the dynamics is not influenced by $\gamma_k$. Notice however that also in this limit the dynamics is slightly different as we still start from states with different symmetries.

The limit of zero final interaction is indeed interesting also because it allows an exact calculation of the gap dynamics. In particular this contributes to the physical understanding of the dephasing mechanism behind the decay of the gap oscillations. If we take $\lambda^f = 0$ then during the evolution the Hamiltonian has only the kinetic part and

we have the trivial solution for the evolution of the field operators $c_{k\sigma}(t) = e^{-i\epsilon_k t} c_{k\sigma}(0)$. We can plug this equation into the expression of what we can define as the "dimensionless" order parameter $\Phi = \frac{\Delta}{\lambda}$. Since the result is similar regardless the initial symmetry, here we report the easier calculation in the s-wave case:

$$\phi(t) = \sum_k \langle c_{-k\downarrow}(t) c_{k\uparrow}(t) \rangle = \Delta \rho_0 \int_0^{\frac{W}{\Delta}} dx \frac{e^{-2ix\Delta t}}{\sqrt{x^2+1}} \propto \frac{e^{-2t\Delta}}{\sqrt{t\Delta}}, \quad (31)$$

where the last relation holds in the limit of long times.

In the next section we will see how this picture is modified when we analyze the dephasing mechanism for small quenches. This will give us a clear picture of the enhanced effectiveness of the dephasing mechanism in d-wave superconductors because its distinctive nodal lines.

## 5.2 DYNAMICS AFTER A SMALL PERTURBATION

The increased damping of the d-wave gap dynamics is a signature of the existence of low-energy excitations, as it can be understood at least in the case of small quenches for which we can calculate the linear response theory variation $\delta\Delta(t)$.

Indeed, in this case we can think the quench as being a small perturbation proportional to $\delta\lambda = \lambda_f - \lambda_i$ and having the same form of the interaction term of the original Hamiltonian:

$$\delta\mathcal{H} = \delta\lambda \sum_{kp} \gamma_k \gamma_p^* c_{k\uparrow}^\dagger c_{-k\downarrow}^\dagger c_{-p\downarrow} c_{p\uparrow}. \quad (32)$$

Then, with the Kubo formula we can calculate the deviation of the gap from the initial value in linear order in such a perturbation:

$$\delta\Delta(t) = -i \sum_p \gamma_p^* \int_0^t dt' \, \langle [c_{-p\downarrow}(t) c_{p\uparrow}(t), \delta\mathcal{H}(t')] \rangle \, . \quad (33)$$

It turns out the commutator in Eq. (33) can be calculated most simply if we first consider a decoupling of Eq. (32) in both particle-particle and particle-hole channels:

$$\delta\mathcal{H}_{MF} = \delta\lambda \sum_p \Big[ \frac{\Delta_p}{\lambda^i} (c_{p\uparrow}^\dagger c_{-p\downarrow}^\dagger + c_{-p\downarrow} c_{p\uparrow}) + \gamma_p^2 n_p (c_{p\uparrow}^\dagger c_{p\uparrow} + c_{-p\downarrow}^\dagger c_{-p\downarrow}) \Big], \quad (34)$$

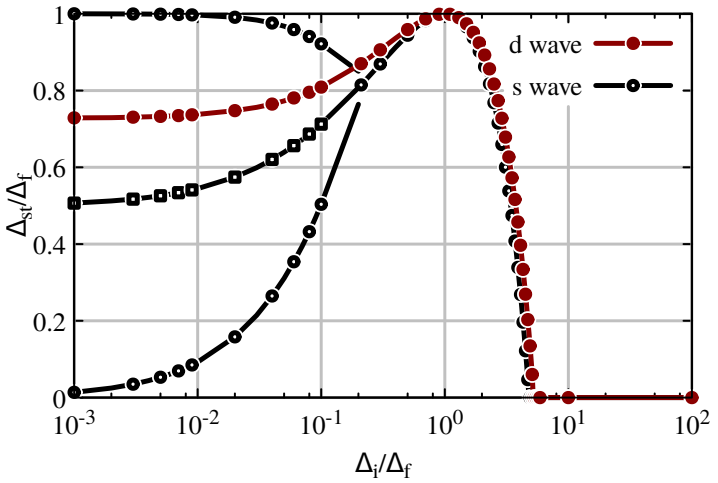


Figure 23: Plot of the stationary gap $\Delta_{st}/\Delta_f$ as a function of the quench parameter $\Delta_i/\Delta_f$ for the d-wave (full red line with full circles) and s-wave (black line with empty circles) symmetries. For $\Delta_i/\Delta_f \lesssim 0.2$ the s-wave gap exhibits undamped oscillations around the value indicated with a square, in this case the circles indicate the extrema of the oscillations.

where $n_k$ and $\Delta_k$ are the unperturbed values. The details of the derivation are given in the appendix. Here we state the result which reads:

$$\delta\Delta(t) = \delta\lambda\Big[\frac{\Delta_k}{\lambda^i}\left((G^<(t))^2 - (G^>(t))^2 - (F^<(t))^2 + (F^>(t))^2\right) + 2\gamma_k^2 n_k (G^>(t)F^>(t) - G^<(t)F^<(t))\Big] \propto \sum_k \frac{\gamma_k^2\epsilon_k^2}{(E_k^i)^3}\left(1-\cos 2E_k t\right). \tag{35}$$

Eq. (35) describes damped oscillations around a finite value. At long times the sum is dominated by the lowest $E_k^i$ and by the singular points in the density of states. For the s-wave superconductor the density of states has a sharp edge at $\Delta_i$ where it has a squared-root divergence. This leads to power-law damped oscillations with frequency $2\Delta_i$. The d-wave symmetry introduces a qualitative difference in the density of states, which diverges only logarithmically at $\Delta_i$ and has finite value for energies down to zero. This results in oscillations which damp much faster.

## 5.3 LONG-TIME STATIONARY VALUE

Also the d-wave model, as the s-wave, presents different dynamical regimes. which are related to the the value of the "quench parameter" $\frac{\Delta_i}{\Delta_f}$, that is the ratio of the *equilibrium values* of the gap for the two interactions $\lambda^i$ and $\lambda^f$. It is interesting to note that these two values

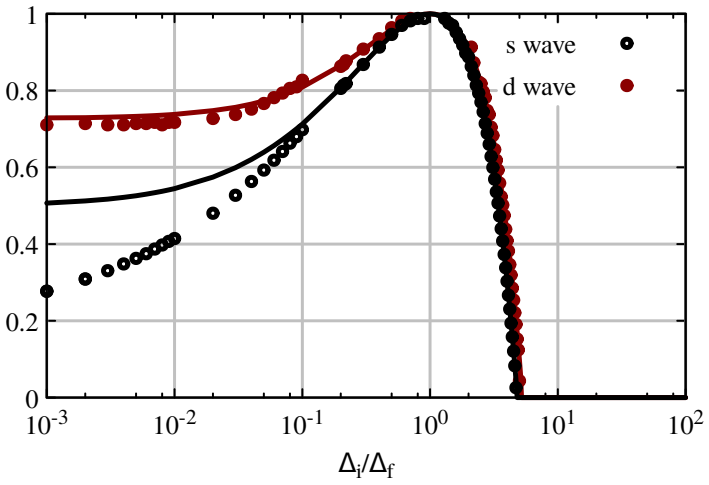


Figure 24: Half the frequency of the oscillations $\frac{\omega}{2}$ (symbols) compared to the stationary $\Delta^{st}$ (lines).

of the gap are in practice never attained in the calculation. Indeed, at the initial time the gap is $\frac{\lambda^f}{\lambda^i}\Delta_i$ and during the following dynamics we always have $\Delta(t) < \Delta_f$ (apart for some quenches and some very short times). Indeed, being the system in an excited, nonequilibrium, state, its gap is always lower than the equilibrium, zero temperature gap.

However, in this case we find only *two* regimes:

1. Damped oscillations to an asymptotic stationary value different from zero,

2. Exponentially overdamped decay to a vanishing gap.

The different dynamical regimes and the long-time gap values for s- and d-wave symmetries are summarized in Fig. 23 where we plot the long-time stationary value of the gap as a function of the quench parameter. For any value of $\frac{\Delta_i}{\Delta_f}$ we find that at long times the quench leads to a reduction of the gap with respect to the zero temperature equilibrium value $\Delta_f$. One remarkable difference is, as we discussed above, the diasppearance of the regime of persistent oscillations. On the other hand, for $\frac{\Delta_i}{\Delta_f} \gtrsim e^{-\frac{\pi}{2}}$ the gap reaches essentially the same asymptotic value, despite the much faster decay of the d-wave gap. It is important to emphasize that even though the stationary value is the same, the way the d-wave model and the s-wave model go to the stationary value is much different, namely the d-wave model relaxes much faster.

In FIGURE 24 we plot the frequency of the oscillations at long times and compare it to the stationary value of the gap. We find that the these two quantities match exactly for the d-wave superconductor $\omega = 2\Delta_{st}$. This result has a simple physical interpretation. Indeed, at long times, when the gap has reached a stationary value, the mean-field Hamiltonian is no more time dependent. It follows that the re-

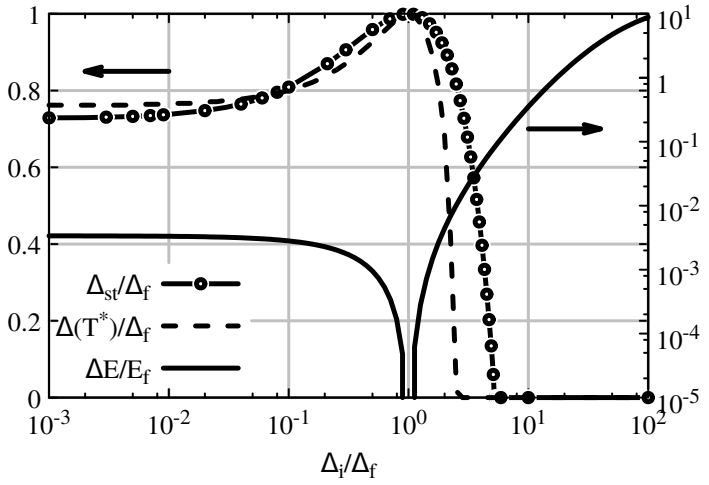


Figure 25: Comparison of the nonequilibrium stationary gap $\Delta_{st}$ with the thermal gap $\Delta(T^*)$ that the system would reach if thermalization took place.

tarded Green's function, and therefore the spectral function, are exactly the ones of the system at equilibrium with $\Delta_{st}$. Indeed, contrary to the lesser component of the Green's function, the retarded component has no memory effect, being determined by the differential equation $\partial_t \hat{G}^R(t,t') = \delta(t-t') + \hat{H}(t)\hat{G}^R(t,t')$ with initial condition $\hat{G}^R(t,t) = -i\mathbb{I}$. It follows that, when the stationary value of the gap is reached, the various components oscillate with frequencies related $2E_k = 2\sqrt{\epsilon_k^2 + \gamma_k^2 \Delta_{st}^2}$ and ultimately at long times only the oscillations in $2\Delta_{st}$ survive.

For completeness, in Fig. 25 we also plot $\Delta(T^*)$ which is the gap for a system in equilibrium at the effective temperature $T^*$ corresponding to the energy pumped into the system through the quench. The system could eventually reach this thermal value if we include scattering processes not contained in the Hamiltonian Eq. (28). While the overall behavior of $\Delta(T^*)$ is qualitatively similar to $\Delta_{st}$, the quantitative difference is substantial confirming the nonthermal character of the asymptotic stationary state.

# 6

# SPECTRAL FEATURES

In this chapter we establish a connection between the experiments and the time-resolved single-particle photoemission spectrum of the transient state of our model of d-wave superconductor.

Before doing this, it is however important to discuss the physical interpretation of our calculation, in particular for what concerns the relevance of the quantum quench protocol to the experiments, where the system is excited out of equilibrium by the pump laser. After this general discussion we come to our theoretical description. Motivated by the numerical evidence of a very fast relaxation dynamics and by the experimental observation, we introduce a simple approximation on the gap dynamics which allows us to analytically compute the spectral function making the comparison with experiments more solid and insightful.

## 6.1 INTERPRETATION OF THE QUENCH PROTOCOL

At this point, it is important to discuss the interpretation of the quench protocol in the framework of the pump-probe experiments. Indeed, one can draw at least two distinct correspondences between the parameters of the calculation and the ones of the experimental set up. Previously, we were interested in the comparison of the anisotropic d-wave model with the isotropic s-wave model. This comparison is not affected by the interpretation of the quench protocol, since the practical calculations are the same in both cases. Now, however, we are interested in making a connection with experiments, and it is of primary importance to discuss this issue.

In the standard picture, one considers the explicit dependence of the Hamiltonian upon some parameter $\lambda$. Then, the quench is used to describe the change of the parameter from some initial value to some final value as a result of an external perturbation. As we discussed in CHAPTER 3 this scenario can be realized in cold atoms by the means of the Feshbach resonance.

In contrast, the Hamiltonian of a solid state system can be considered largely independent of the excitation process. In this context, the quench is a theoretical tool to study the evolution of some nonequilibrium state, which results from an impulsive excitation.

These two different interpretations are sketched in FIGURE 26. While in the former picture one regards $\mathcal{H}(\lambda^i)$ as the "unperturbed" Hamiltonian which is modified by the quench, in the latter interpretation one should think to $\lambda^i$ simply as a parameter describing the initial

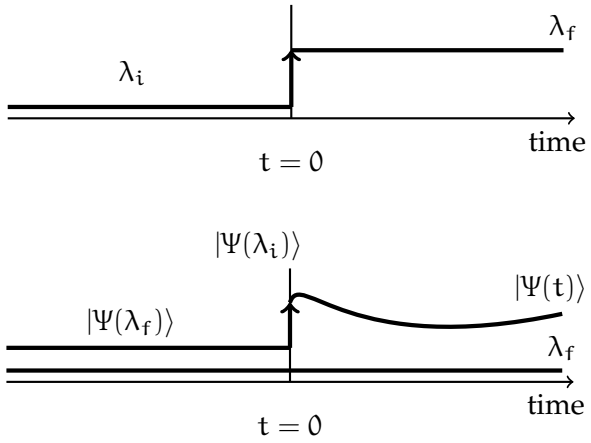


Figure 26: Sketch of two different interpretations of the quench protocol. In the field of cold atoms (top) one can actually vary the interaction. In the solid state context it is more appropriate to think of a constant interaction and a suddenly quenched state (bottom).

excited state $|\Psi(\lambda^i)\rangle$ which evolves according to $\mathcal{H}(\lambda^f)$. In this case $\lambda^f$, which controls the time evolution, has to coincide with the actual interaction that characterizes the material.

Since we are now interested in the solid state context, we are going to adopt the second point of view. Therefore, in our approach the quench protocol does not depict a real change of the interaction of the material, but rather the answer to the general question: "what is, given the time-independent Hamiltonian $\mathcal{H}(\lambda^f)$ corresponding to the material, the evolution of the out-of-equilibrium state $|\Psi(\lambda^i)\rangle$?". Of course $|\Psi(\lambda^i)\rangle$ is a very particular excited state which we choose for mere theoretical convenience, and it can not describe accurately the real excited state in the pump-probe experiment. However, we will see how taking this approach may be fruitful as long as the details of the experimental excitation process are not crucial and the main effect of the pump is to change the superconducting gap.

## 6.2 PHOTOEMISSION SPECTRUM OF SUPERCONDUCTORS

In CHAPTER 2 we have discussed how the ARPES, especially in layerd materials such as the cuprates, provides an intensity signal $I_k(\omega)$ as a function of momentum $k$ and energy $\omega$ that can be directly related to the spectral function of the material through:

$$I_k(\omega) = \mathrm{Im}G^<_k(\omega) = A_k(\omega)f(\omega), \tag{36}$$

where $f(\omega) = (1 + e^{\beta\omega})^{-1}$ is the Fermi-Dirac distribution with inverse temperature $\beta$, $A_k(\omega)$ is the spectral function and $G^<_k(\omega)$ the Fourier transform of the lesser Green's function $G^<_k(t, t')$ which at equilibrium depends only on the difference of the two times.

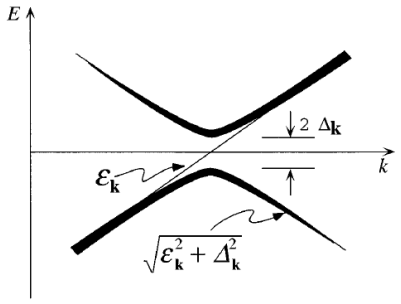


Figure 27: Schematic dispersion in the normal (thin line) and superconducting (thick lines) states following the BCS theory. The thickness of the superconducting state lines indicate the spectral weight given by the BCS coherence factors $v_k^2 = \frac{1}{2}(1 - \frac{\epsilon_k}{E_k})$ below $E_F$ and $u_k^2 = \frac{1}{2}(1 + \frac{\epsilon_k}{E_k})$ above $E_F$. The lesser Green's function, related to the ARPES signal, is obtained if we multiply for the occupation of these states $f(-E_k)$ and $f(E_k)$. Thus, at $T = 0$ only the states below $E_F$ are observable. Notice that, in contrast with the normal phase, in the superconducting phase there is signal for $k > k_F$ also at $T = 0$ because of the particle-hole mixing (Figure from Ref. [66]).

The spectral function can also be related to the Fourier transform of the retarded Green's functions through $A_k(\omega) = \frac{1}{\pi}\mathrm{Im}G_k^R(\omega)$. Therefore Eq. (36) expresses the relation which we have at equilibrium between the lesser Green's function and the retarded Green's function. In physical terms, this relation holds because at equilibrium we know that the available states will be occupied according to the Fermi-Dirac distribution. For a BCS superconductors the ARPES signal is given by two peaks:

$$I_k(\omega) = Z_k^- \delta(\omega + E_k) + Z_k^+ \delta(\omega - E_k), \tag{37a}$$

$$Z_k^\pm = \frac{1}{2}(1 \pm \frac{\epsilon_k}{E_k}) f(\pm E_k), \tag{37b}$$

reflecting the particle-hole mixing characteristic of this state of matter (see FIGURE 27).

As we have seen in CHAPTER 2, when considering a trARPES experiments there are a number of complications arising. First, the various components of the Green's function now depend on two different times, since out of equilibrium there is no time-translational invariance, unless a stationary state *of the whole system* is reached. Second, out of equilibrium the lesser and retarded components of the Green's function are not dependent one on the other. The physical reason behind this is that in this case the occupation of the energy levels is in general not given by the Fermi-Dirac distribution. Therefore in principle one has to keep track of both retarded and lesser components.

As shown in Ref. [41], and already discussed in some detail in CHAPTER 2, the analysis of these issues leads to the following generalization of Eq. (36) to the trARPES signal:

$$I_k(\omega, t_0) = \mathrm{Im} \int dt \int dt' \, s_{t_0}(t) s_{t_0}(t') e^{i\omega(t-t')} G^<_k(t, t'), \tag{38}$$

where $s_{t_0}(t)$ describes the time envelope of the probe pulse which excite the photoelectrons. This is centred around some time $t_0$ at which the acquisition is done (time of the probe) and has some finite width. For example it can be taken as a gaussian centred in $t_0$ and with some width $\sigma_p$.

In the following we will give the result in the approximation $s_{t_0} = 1$ which can be also expressed as the Fourier tranform of the lesser Green's function with respect to the difference of the two times followed by an average:

$$\hat{G}^<_k(\omega, t') = \int d\tau \, \hat{G}^<_k(t' + \tau, t'), \tag{39}$$

$$I_k(\omega) = \frac{1}{T} \int_t^{t+T} dt' \, \hat{G}^<_k(\omega, t'). \tag{40}$$

Indeed, we have found that (see APPENDIX A), at the mean-field level, the proper inclusion of the finite-width pulses merely leads to a smearing of the delta peaks which will appear in our approximate derivation.

## 6.3 SUDDEN APPROXIMATION

Motivated by the fast dynamics of the d-wave gap found in the previous chapter, we now introduce a simplification which consists in considering the abrupt change of the order parameter while the system is not relaxed (see FIGURE 28). Within this approximation we can compute analytically the time-resolved spectrum. In the limit of a very fast order parameter dynamics, we can assume the quasiparticle Hamiltonian to experience an almost sudden change of the pairing field:

$$\Delta_k(t) = \Delta_i \gamma_k \theta(-t) + \Delta_{st} \gamma_k \theta(t). \tag{41}$$

This approximation is also based on some experimental results. In particular Refs. [38, 67] have highlighted two clearly distinct time scales for the gap dynamics following the pump pulse: on a short interval of approximately 0.3 ps the gap reaches a value smaller than at equilibrium ($\Delta_{st}$ in our model) and on a longer time it relaxes to the equilibrium value, typically attained after $10 - 20$ ps. Our sudden approximation for the gap dynamics should therefore be reasonable for times of a few picoseconds after the pump pulse. It is interesting to notice that on these time scales an effective temperature picture of

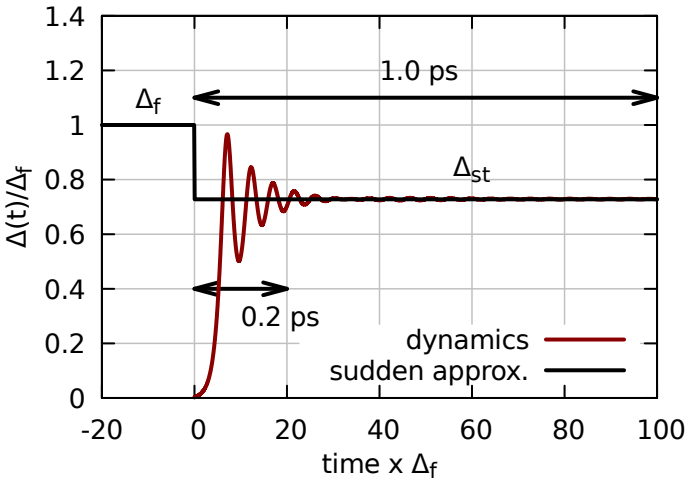


Figure 28: Schematic of the sudden approximation to the gap dynamics related to the experimental observation and to the numerical evidence of a fast dynamics of the gap.

the ARPES spectra is not adequate, as firmly pointed out in Ref. [67]. Finally, if we consider the maximum gap value at equilibrium for Bi2212 $\Delta_f = 60$meV we can estimate a time scale of about 0.01ps for FIGURE 28.

Within this sudden approximation for the gap dynamics we can calculate the lesser Green's function $\hat{G}(t,t')$ and after a Fourier transform with respect to the difference $t-t'$ and averaging with respect to $t'$ we find:

$$I_{kneq}(\omega) = Z^{-}_{kneq}\delta(\omega + E^{st}_k) + Z^{+}_{kneq}\delta(\omega - E^{st}_k), \tag{42a}$$

$$Z^{-}_{kneq} = \frac{1}{2}(1 - \frac{\epsilon_k}{E^{st}_k})\left[\frac{1}{2} + \frac{\epsilon^2_k + \gamma^2_k\Delta_{st}\Delta_i}{2E^{st}_k E^{i}_k}\right], \tag{42b}$$

$$Z^{+}_{kneq} = \frac{1}{2}(1 + \frac{\epsilon_k}{E^{st}_k})\left[\frac{1}{2} - \frac{\epsilon^2_k + \gamma^2_k\Delta_{st}\Delta_i}{2E^{st}_k E^{i}_k}\right]. \tag{42c}$$

which is the same as for a superconductor with gap $\Delta_{st}$ but with the *thermal* factor $f(\pm E^{st}_k)$ substituted by the *non-thermal* term in square brackets on the right hand side of Eqs. (42B) and (42C).

This takes a particularly clear and interesting form if we expand it in the neighborhood of the nodal lines for $\frac{\gamma_k}{\epsilon_k} \ll 1$ since in this limit we can approximate:

$$1 - \frac{\epsilon_k}{E_k} \simeq 1 - \frac{\epsilon_k}{|\epsilon_k|}(1 - \frac{\Delta^2\gamma^2_k}{2\epsilon^2_k}) = \begin{cases} \frac{\Delta^2\gamma^2_k}{2\epsilon^2_k} & \epsilon_k > 0, \\ 2 - \frac{\Delta^2\gamma^2_k}{2\epsilon^2_k} & \epsilon_k < 0, \end{cases} \tag{43}$$

$$\frac{1}{2} + \frac{\epsilon^2_k + \Delta_i\Delta_{st}}{2E^{st}_k 2E^{i}_k} \simeq 1 - \frac{(\Delta_{st} - \Delta_i)^2\gamma^2_k}{4\epsilon^2_k}, \tag{44}$$

We can now look at the spectral weight associated to the negative frequency peak and compare it with the one at equilibrium. For what

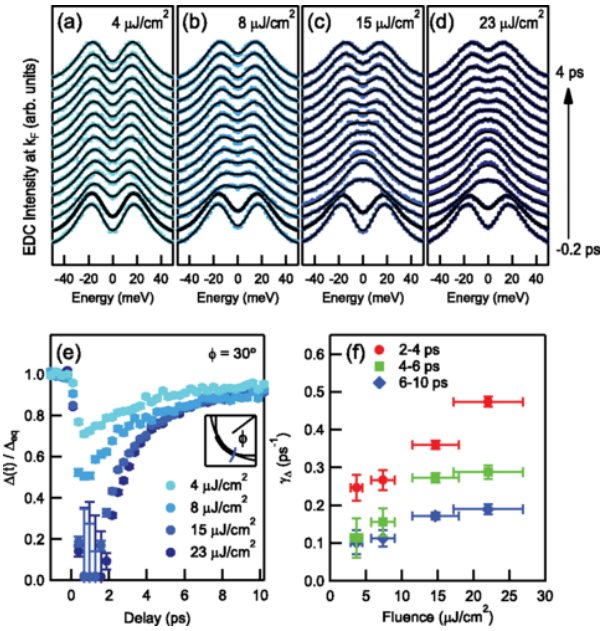


Figure 29: Experimental evidence for a fast dynamics of the gap, which closes in a window of a fraction of picosecond to recover only after several picoseconds [38].

we have discussed above regarding the interpretation of the quench, it is now appropriate to compare the out-of-equilibrium spectral weight with the one at equilibriu for $\Delta_f$:

$$\frac{Z^-_{kneq}}{Z^-_{keq}} = \frac{1-\frac{\epsilon_k}{E^{st}_k}}{1-\frac{\epsilon_k}{E^f_k}}, \left(\frac{1}{2}+\frac{\epsilon_k^2+\Delta_{st}\Delta_i\gamma_k^2}{2E^{st}_k E^i_k}\right). \tag{45}$$

Therefore in this limit:

$$\frac{Z^-_{kneq}}{Z^-_{keq}} = \begin{cases} \frac{\Delta^2_{st}}{\Delta^2_f} & \epsilon_k > 0, \\ 1-\frac{\alpha\gamma_k^2}{4\epsilon_k^2} & \epsilon_k < 0, \end{cases} \tag{46}$$

where $\alpha = \Delta_i^2 - \Delta_f^2 + 2\Delta_{st}^2 - 2\Delta_{st}\Delta_i > 0$. Therefore the spectral weight at the node is reduced in both cases $\epsilon_k \lesseqgtr 0$ except possibly in a small region close to the Fermi surface where the condition $\frac{\gamma_k^2}{\epsilon_k^2} \ll 1$ does not hold. This reduction is clearly a nonthermal effect since finite temperature excitations of quasiparticle would lead to a reduction proportional to the Fermi function.

# 7

# CONCLUSIONS

In this part we have discussed the distinctive features of the dynamics of a d-wave superconductor after a quantum quench of the interaction. As a consequence of the low-energy excitations, the oscillations of the superconducting gap are subject to a fast decay which we have characterized both qualitatively and quantitatively. In particular, on the qualitative level we have found that the d-wave superconductor does not display a regime with persistent oscillations of the gap, contrary to the conventional *s*-wave superconductor. This result may be ascribed to the inherent anisotropy of the $d_{x^2-y^2}$ and on the mathematical level is reflected in the lack of an exact expression for its dynamics, again contrary to the case of isotropic gaps.

An important finding is that, in the large range of parameters for which both anisotropic d-wave and isotropic *s*-wave display damped oscillations of the gap, the power-law decay of the oscillations of the d-wave gap is $\frac{1}{t^2}$, in contrast with the well-known power-law $\frac{1}{\sqrt{t}}$ typical of fully-gapped isotropic superconductors. On a general ground, this fact is interesting in its own and may be taken as a "dynamical" manifestation of a d-wave gap in the same spirit as the power-law temperature dependence of the penetration depth discussed in CHAPTER 1 is a "thermodynamic" signature. Morevoer, this power-law exponent may be observable in future experiments on the Higgs mode, or amplitude mode, on d-wave superconductors.

Finally, we have derived an analytical expression for the transient trARPES signal, showing a non-thermal loss of spectral weight, in particular in proximity of the nodal lines.

# Part III

# SUPERCONDUCTIVITY BEYOND MEAN-FIELD

# 8

# EQUILIBRIUM DYNAMICAL MEAN-FIELD THEORY

The Dynamical Mean-Field Theory (DMFT) is emerging in the last decades as one of the reference methods to treat strongly interacting systems beyond any perturbative limit. As the name implies, DMFT can be seen as a quantum (or dynamical) generalization of the usual mean-field theory, where the spatial fluctuations are frozen assuming that all the lattice sites are completely equivalent, but the local quantum dynamics is fully taken into account. DMFT becomes indeed exact in the limit of infinite dimensionality or lattice coordination [68], where every lattice site actually interacts with an average of the infinite neighbors.

In practice DMFT is based on the mapping of a lattice Hamiltonian into an impurity Hamiltonian [69], where an interacting site (the impurity) is hybridized with a non-interacting bath, which represents the effect of the rest of the lattice on the impurity site. The mean-field condition determines a self-consistency condition, conceptually similar to the Curie-Weiss equation, which now requires that the frequency-dependent Green's function of the impurity site coincides with the local component of the lattice Green's function, thereby enforcing the equivalence between every lattice site.

This means that a DMFT solution requires the iterative solution of an impurity model enforcing recursively the self-consistency condition. Importantly, the impurity model is clearly a much simpler problem with respect to the original lattice model because only one site is interacting, but is is highly non-trivial, which leads to a rich physics which made the method so successful.

It is also worth to mention that DMFT becomes exact, also in finite dimensions, both in the non-interacting limit $U = 0$ and in the atomic limit $t = 0$ and it is able to describe accurately the evolution between these two regimes, both for the repulsive Model and for the attractive one.

## 8.1 ATTRACTIVE HUBBARD MODEL

Here, we are interested in the attractive ($U < 0$) Hubbard model

$$\mathcal{H} = -t \sum_{\langle ij \rangle} c^{\dagger}_{i\sigma} c_{j\sigma} + U \sum_{i} n_{i\uparrow} n_{i\downarrow} - \mu \sum_{i} n_{i}, \tag{47}$$

where $t$ is a hopping matrix element between neighboring lattice sites (the symbol $\langle \dots \rangle$ denotes a sum over nearest-neighbor sites of lattice), $U$ is the strength of the attractive interaction between two electrons

on the same lattice site, and $\mu$ is the chemical potential. We work in the grandcanonical ensemble, where the fermionic density is fixed by a proper choice of the chemical potential.

The corresponding impurity Hamiltonian reads:

$$\begin{aligned}\mathcal{H} =& -\mu(d_\uparrow^\dagger d_\uparrow + d_\downarrow^\dagger d_\downarrow) + U d_\uparrow^\dagger d_\uparrow d_\downarrow^\dagger d_\downarrow \\ &+ \sum_{k\sigma}(V_k f_{k\sigma}^\dagger d_\sigma + V_k^* d_\sigma^\dagger f_{k\sigma}) \\ &+ \sum_{k\sigma}\epsilon_k f_{k\sigma}^\dagger f_{k\sigma} - \sum_k(\Delta_k f_{k\uparrow}^\dagger f_{-k\downarrow}^\dagger + \Delta_k^* f_{-k\downarrow} f_{k\uparrow}).\end{aligned} \tag{48}$$

In this work we limit ourselves to half-filling ($n = 1$). Since the dispersion is symmetric around zero, the half-filling condition can be implemented by imposing the particle-hole symmetry of the problem, which is realized assuming $\mu = \frac{U}{2}$ in both Eqs. (47) and (48). The coefficients $\epsilon_k$, $\Delta_k$ and $V_k$ describe a BCS superconductor which is hybridized with the impurity and acts as a bath. The choice of a superconducting bath is crucial to obtain explicit superconducting solutions, as expected for the attractive Hubbard model.

The DMFT condition is enforced imposing the equality of the local component of lattice Green's function with the impurity Green's function. In the superconducting phase we have to take into account both a *normal* component – the usual electron propagator – and an *anomalous* component, which is related to the particle-hole hybridization typical of superconductors. It is therefore convenient to use the notation of the Nambu spinors. The impurity Green's function is therefore:

$$\hat{G}(\tau) = -\langle T_\tau \gamma(\tau)\gamma^\dagger\rangle = \begin{pmatrix} G(\tau) & F(\tau) \\ \bar{F}(\tau) & \bar{G}(\tau)\end{pmatrix}, \qquad \gamma = \begin{pmatrix} d_\uparrow \\ d_\downarrow^\dagger\end{pmatrix}. \tag{49}$$

In this section we will use the Matsubara – or thermal – Green's function. The four components of the Green's function are not independent but they satisfy the following relations:

$$\bar{G}(\tau) = -G(-\tau), \tag{50a}$$
$$\bar{G}(i\omega) = -G^*(i\omega), \tag{50b}$$
$$\bar{F}(\tau) = F^*(\tau), \tag{50c}$$
$$\bar{F}(i\omega) = F(i\omega). \tag{50d}$$

The local component of thelattice Green's function is defined as the sum over all momenta of the lattice Green's function:

$$\hat{G}(\tau) = \sum_k -\langle T_\tau \Phi_k(\tau)\Phi_k^\dagger\rangle, \qquad \Phi_k = \begin{pmatrix} c_{k\uparrow} \\ c_{-k\downarrow}^\dagger\end{pmatrix}. \tag{51}$$

Within DMFT one can show that the self-energy becomes momentum-independent and it coincides with the impurity self-energy which enters the Dyson equation for the impurity model :

$$\hat{G}^{-1}(i\omega) = \hat{\mathcal{G}}_0^{-1}(i\omega) - \hat{\Sigma}(i\omega), \tag{52}$$

where $\hat{\mathcal{G}}_0$ is the non-interacting Green's function of the impurity – the so-called *Weiss field* in the DMFT context. The name derives from the analogy with static mean-field theory. $\hat{\mathcal{G}}_0$ is indeed the effective dynamical field which the impurity electrons experience because of the presence of the rest of the lattice.

Therefore the local lattice Green's function can be written as:

$$\hat{G}_k^{-1}(i\omega) = i\omega\mathbb{I} + (\mu - \epsilon_k)\hat{\sigma}_3 - \hat{\Sigma}(i\omega), \tag{53}$$

where $\mathbb{I}$ and $\hat{\sigma}_3$ are respectively the identity and the third Pauli matrix in the space of the Nambu spinors and $\epsilon_k$ is the bare lattice dispersion. The self-consistency requires that its sum over all momenta of this quantity coincides with the impurity Green's function above.

The Weiss field is determined by the quadratic (in the fermionic operators) terms of the Hamiltonian Eq. (48) and therefore it satisfies:

$$\hat{\mathcal{G}}_0^{-1}(i\omega) = i\omega\mathbb{I} + \mu\hat{\sigma}_3 - \hat{\Delta}(i\omega), \tag{54}$$

where $\hat{\Delta}(i\omega)$ describes the hybridization with the superconducting bath.

In the following we are going to consider the Hubbard model on the so-called Bethe lattice, an infinite-coordination tree which is an infinite-coordination lattice whose density of states has a compact support, therefore mimicking effectively a finite-dimensionality system. The density of states is actually semicircular and it leads to an important simplification of the self-consistency condition.

In this case the hybridization has a simple relation with the local lattice Green's function:

$$\hat{\Delta}(i\omega) = \frac{D^2}{4}\hat{\sigma}_3\hat{G}(i\omega)\hat{\sigma}_3, \tag{55}$$

where D is the half of the bandwidth (i.e. the dispersion ranges from $-D$ to D). Therefore we can write the self-consistency condition as:

$$\hat{\mathcal{G}}_0^{-1}(i\omega) = i\omega\mathbb{I} + \mu\hat{\sigma}_3 + \frac{D^2}{4}\hat{\sigma}_3\hat{G}(i\omega)\hat{\sigma}_3, \tag{56}$$

where we can view $\hat{G}$ as a functional of the Weiss field.

Eqs. (52), (54) and (55) are a complete set of conditions which however cannot be reduce to a closed form, in contrast to what happens in the case of the usual mean-field theory. Therefore, one has to solve them iteratively with an algorithm that is typically as follows. Starting from a guess for one quantity, say the Weiss field $\hat{\mathcal{G}}_0$, we have to:

1. solve the impurity problem: calculate $\hat{\Sigma}$ and from this $\hat{G}$ (Eq. (52)) (unless the impurity solver direcly provides $\hat{G}$),

Figure 30: The first and second order skeleton diagrams.

2. calculate a *new* Weiss field $(\hat{\mathcal{G}}_0)_n$ from the *self-consistency* relation Eq. (54),
3. if $(\hat{\mathcal{G}}_0)_n = \hat{\mathcal{G}}_0$ then the set $\{\hat{G}, \hat{\mathcal{G}}_0, \hat{\Sigma}\}$ is our DMFT solution. If not, we set $\hat{\mathcal{G}}_0 = (\hat{\mathcal{G}}_0)_n$ and start the *loop* again from 1.

This is based on considering the skeleton diagrams of the many-body perturbation theory (MBPT) up to second order. However, in standard MBPT these diagrams are usually calculated in terms of the "dressed" propagator which in this case would be the interacting $\hat{G}$. In iterated pertubration theory (IPT) only the first order diagrams are calculated in this way. The result is the Hartree-Fock self energy $\hat{\Sigma}_{HF}$. Then, the second order diagrams are calculated in terms of a "corrected" Weiss field $\hat{\tilde{\mathcal{G}}}_0$:

$$\hat{\tilde{\mathcal{G}}}_0^{-1}(i\omega) = \hat{\mathcal{G}}_0^{-1}(i\omega) - \hat{\Sigma}_{HF}. \tag{57}$$

Since $\hat{\Sigma}_{HF}$ does not depend on frequency, this can be thought of as a redefinition of the free part of the impurity Hamiltonian.

It is convenient to use the notation of Nambu spinors also in calculating these diagrams (FIGURE 30). The propagators are Nambu Green's functions, at each vertex there is an interaction $\hat{\sigma}_3 U \hat{\sigma}_3$, as usual the sign of a diagram is given by $(-1)^{n+l}$ where $n$ is the order of the diagram and $l$ is the number of fermionic loops, and finally for every loop we have to perform a trace over the Nambu indices.

The first order diagrams are therefore:

$$U\delta(\tau)\hat{\sigma}_3 \mathrm{Tr}\left(\hat{G}(0^-)\hat{\sigma}_3\right) \qquad \text{"tadpole"}, \tag{58}$$

$$-U\delta(\tau)\hat{\sigma}_3 \hat{G}(0^-)\hat{\sigma}_3 \qquad \text{"sunrise"}. \tag{59}$$

The *tadpole* contribution vanishes at half-filling, while the *sunrise* diagram gives:

$$\hat{\Sigma}_{HF} = U\delta(\tau)\begin{pmatrix} \frac{n}{2} & \phi \\ \phi & 1-\frac{n}{2} \end{pmatrix}, \tag{60}$$

$\frac{n}{2} = G(0^-) = 1$ is the density – or filling – while $\phi = F(0^-)$ is the dimensionless superconducting order parameter. In general $\phi$ is a complex number but here, without loss of generality, we take it to be real. The superconducting parameter is $\Delta = U\phi$.

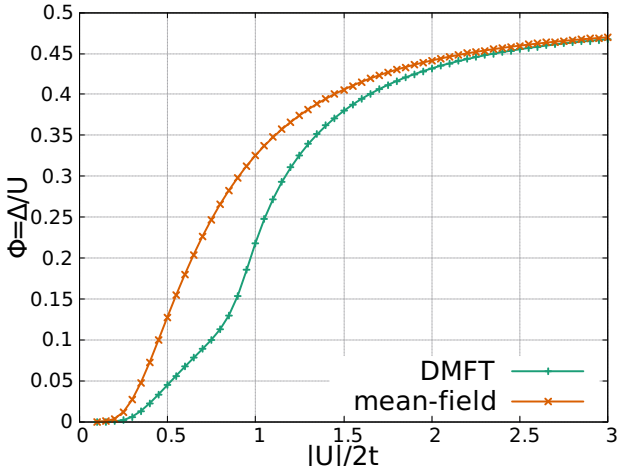


Figure 31: Dimensionless superconducting order parameter $\phi = \frac{\Delta}{U}$ as a function of the interaction strenght $\frac{|U|}{2t}$ at half filling. The system parameters are $\beta = 100$ and $W = 2t = 1$. For comparison, we report the result of mean-field theory.

The second order skeleton diagrams are:

$$-U^2 \hat{\sigma}_3 \hat{\tilde{\mathcal{G}}}_0(\tau) \hat{\sigma}_3 \mathrm{Tr}\left(\hat{\tilde{\mathcal{G}}}_0(-\tau) \hat{\sigma}_3 \hat{\tilde{\mathcal{G}}}_0(\tau) \hat{\sigma}_3\right), \tag{61a}$$

$$U^2 \hat{\sigma}_3 \hat{\tilde{\mathcal{G}}}_0(\tau) \hat{\sigma}_3 \hat{\tilde{\mathcal{G}}}_0(-\tau) \hat{\sigma}_3 \hat{\tilde{\mathcal{G}}}_0(\tau) \hat{\sigma}_3, \tag{61b}$$

which result in

$$\Sigma_r(\tau) = U^2 \tilde{\mathcal{G}}_0(\tau)\left[\tilde{\mathcal{G}}_0(\tau)\tilde{\mathcal{G}}_0(\beta-\tau) - \tilde{\mathcal{F}}_0^2(\tau)\right], \tag{62a}$$

$$S_r(\tau) = U^2 \tilde{\mathcal{F}}_0(\tau)\left[\tilde{\mathcal{G}}_0(\tau)\tilde{\mathcal{G}}_0(\beta-\tau) - \tilde{\mathcal{F}}_0^2(\tau)\right], \tag{62b}$$

the subscript "r" stands for "regular" as opposed to the Hartree-Fock self energy which is singular, being proportional to the delta function $\delta(\tau)$. The total self energy is therefore:

$$\hat{\Sigma}(i\omega) = \hat{\Sigma}_{HF} + \hat{\Sigma}_r(i\omega). \tag{63}$$

In FIGURE 31 we report the result of the calculation for the superconducting order parameter and compare it with the result of static mean-field theory. As expected, the largest deviations are for intermediate strength of the interaction. Intrestingly, the weak-coupling regime, where DMFT and mean-field provide similar results appears limited to very small interaction values suggesting an important role of quantum fluctuations already for very small values of $U$ of the order of a few tenths of the bandwidth. The two methods also tend to coincide in strong coupling, where the superconducting order parameter saturates to its maximum possible value at zero temperature. This clearly demonstrates that the IPT results are accurate well beyond the perturbative regime because of the self-consistency condition.

*Additional details*

In the calculation we actually start the iterative process by taking a lattice Green's function of the BCS type:

$$\hat{G}_\epsilon(i\omega) = -\frac{i\omega\mathbb{I} + \hat{H}_\epsilon}{\omega^2 + E_\epsilon^2}, \tag{64}$$

$$\hat{G}_\epsilon(\tau) = -\frac{e^{(\tau-\frac{\beta}{2})\hat{H}_\epsilon}}{2\cosh\frac{\beta E_\epsilon}{2}}. \tag{65}$$

The expression in terms of Matsubara frequencies is more easily integrated over the density of states of the Bethe lattice, the result is the initial guess for the local Green's function:

$$\hat{G}(i\omega) = \int \rho(\epsilon)\hat{G}_\epsilon(i\omega) = -\frac{i\omega\mathbb{I} + \Delta\hat{\sigma}_1}{\frac{W^2}{2}}\left[\sqrt{\frac{\omega^2 + W^2 + \Delta^2}{\omega^2 + \Delta^2}} - 1\right]. \tag{66}$$

The initial guess for the self energy is $\hat{\Sigma} = \hat{\Sigma}_{\mathrm{HF}}$ and therefore the initial Hartree-corrected Weiss field coincides with the initial guess for the local Green's function.

Written in terms of Nambu components, also exploiting the relationships of Eqs. (50), the Dyson equation (52) reads:

$$G(i\omega) = \frac{\frac{\tilde{\mathcal{G}}_0(i\omega)}{d_1(i\omega)} - \Sigma^*(i\omega)}{d_2(i\omega)}, \tag{67a}$$

$$F(i\omega) = \frac{\frac{\tilde{\mathcal{F}}_0(i\omega)}{d_1(i\omega)} - S(i\omega)}{d_2(i\omega)}, \tag{67b}$$

$$d_1(i\omega) = |\tilde{\mathcal{G}}_0(i\omega)|^2 + |\tilde{\mathcal{F}}_0(i\omega)|^2, \tag{67c}$$

$$d_2(i\omega) = |\frac{\tilde{\mathcal{G}}_0(i\omega)}{d_1(i\omega)} - \Sigma^*(i\omega)|^2 + |\frac{\tilde{\mathcal{F}}_0(i\omega)}{d_1(i\omega)} - S(i\omega)|^2. \tag{67d}$$

Actually the Weiss field $\hat{\mathcal{G}}_0$ disappears from the equations in favor of the Hartree-corrected $\hat{\tilde{\mathcal{G}}}_0$. Then the self-consistency relation (56) becomes:

$$\hat{\tilde{\mathcal{G}}}_0^{-1}(i\omega) = i\omega\mathbb{I} - \hat{\Sigma}_{\mathrm{HF}} - t^2\hat{\sigma}_3\hat{G}\hat{\sigma}_3, \tag{68}$$

which written in the two independent Nambu components reads ($\hat{\Sigma}_{\mathrm{HF}} = \Delta\hat{\sigma}_1$):

$$\tilde{\mathcal{G}}_0(i\omega) = \frac{(i\omega - G(i\omega))^*}{|i\omega - G(i\omega)|^2 + |F(i\omega) - \Delta|^2}, \tag{69a}$$

$$\tilde{\mathcal{F}}_0(i\omega) = \frac{F(i\omega) - \Delta}{|i\omega - G(i\omega)|^2 + |F(i\omega) - \Delta|^2}. \tag{69b}$$

# 9

# NONEQUILIBRIUM DYNAMICAL MEAN-FIELD THEORY

In this chapter we describe the method of nonequilibrium dynamical mean-field theory (NDMFT) focusing on the application to superconductivity. This method represents the natural and direct extension of dynamical mean-field theory (DMFT) to the study of quantum systems out of equilibrium. Indeed the whole DMFT construction, where the spatial fluctuations are frozen while the full local dynamics is taken into account, is intrinsically and directly extended out of equilibrium retaining essentially all the relevant features of its equilibrium counterpart. In recent years NDMFT has been applied to several problems of correlated lattice systems out of equilibrium [70] even if, as we shall see, its development is still far from the level we reached in equilibrium. This chapter is mainly dedicated to the description of its implementation in the superconducting phase and to some preliminary results obtained for the quantum dynamics following a quantum quench in the attractive Hubbard model.

## 9.1 FROM EQUILIBRIUM TO OUT OF EQUILIBRIUM

DMFT is based upon the fact that, for models with local interactions, one can replace all the diagrams in the skeleton expansion of MBPT with their local versions and as a consequnce the self-energy become local in space, i. e. independent on momentum. This allows an *exact* mapping of the lattice problem into an impurity problem, whose diagrams are local by definition, as long as a self-consistency condition relating the local problem with the original lattice holds.

Out of equilibrium the MBPT formalism is extended by considering a Green's function on the so-called "Keldysh contour" shown in FIGURE 32 [71–73]. Then, exploiting the same property of DMFT in this formalism, one can extend the method to out-of-equilibrium problems. However, despite the derivation and the formal structure are essentially identical to DMFT, an actual calculation of NDMFT is much more demanding in several respects. Indeed, while the main object of MBPT at equilibrium is the Matsubara Green's function in imaginary time $\hat{G}^M(\tau)$ or in Matsubara frequency $\hat{G}^M(i\omega)$, out of equilibrium it is appropriate to consider a Green's function $\hat{G}(z, z')$ whose variables live on the Keldysh contour depicted in FIGURE 32. Therefore one has to define different functions labeled by the branches to which the two arguments $z$ and $z'$ belong. Since both arguments can belong to $\mathcal{C}_1$, $\mathcal{C}_2$ and $\mathcal{C}_3$, in principle we have to deal with nine Green's functions.

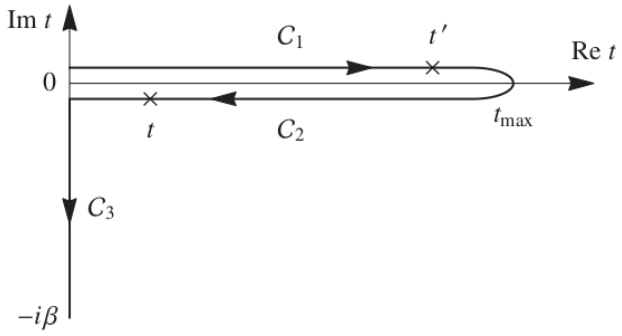


Figure 32: The Keldysh contour.

A second important source of difficulty is the lack of invariance for time translation typical of systems out of equilibrium, unless they reach a stationary state. The consequence is that we cannot make use of Fourier transformations. These are crucial in the equilibrium MBPT since they allow to transform derivatives and convolutions into products and therefore integro- and integro-differential equations, which would hold into the time domain, into much simpler *algebraic* equations in the frequency domain.

The final, and highest, hurdle is the solution of the impurity model. As a matter of fact, all the impurity solvers who work smoothly with a moderate computational cost in equilibrium have problems out of equilibrium. For this reason the development of the field is rather slow, and the search for "cheap" and accurate solvers for the non-equilibrium impurity models is one of the most important challenges in the field.

We now turn back to the formalism and discuss what are the consequences of the lack of translational invariance. The main consequence is that instead of $\hat{G}^{-1}(i\omega) = \hat{\mathcal{G}}_0^{-1}(i\omega) - \hat{\Sigma}(i\omega)$ the Dyson equation now reads:

$$\hat{G}(z,z') = \hat{\mathcal{G}}_0(z,z') + \int_{\mathcal{C}} dz'' \int_{\mathcal{C}} dz''' \hat{\mathcal{G}}_0(z,z'')\hat{\Sigma}(z'',z''')\hat{G}(z''',z'), \quad (70)$$

where $\int_{\mathcal{C}} dz$ denotes an integral over the Kadanoff-Baym contour. On the other hand, the self-consistent condition which at equilibrium reads $\hat{\mathcal{G}}_0^{-1}(i\omega) = i\omega\mathbb{I} + \mu\hat{\sigma}_3 - \hat{\Delta}(i\omega)$ becomes:

$$i\partial_z \hat{\mathcal{G}}_0(z,z') = \delta(z,z')\mathbb{I} - \mu\hat{\mathcal{G}}_0(z,z') + \int_{\mathcal{C}} dz''\hat{\Delta}(z,z'')\hat{\mathcal{G}}_0(z'',z'), \quad (71)$$

where $\partial_z$ denotes a derivative with respect to the contour variable and $\delta(z,z')$ is the Dirac delta function defined on the contour.

Fortunately, a few observations lead to some important simplifications in the formalism. First, the nine components of the Kadanoff-Baym Green's functions are not actually independent. It is customary to choose as independent the *lesser* component $\hat{G}^<(t,t')$, the *retarded*

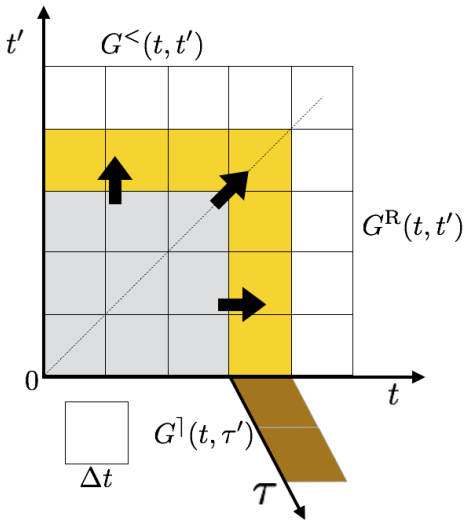


Figure 33: Time propagation scheme.

component $\hat{G}^R(t,t')$, the *mixed* component $\hat{G}^\urcorner(t,\tau)$ and the Matsubara component $\hat{G}^M(\tau)$. Again, at equilibrium there is a definite relation among these components. For example the retarded and lesser components are related by the fluctuation-dissipation theorem and this essentially comes from the fact that the occupancy of the density of states in thermal equilibrium has to follow the Fermi-Dirac distribution. Out of equilibrium this is not the case and so the two components are independent.

The second simplification is that we can easily decompose the equations (70) and (71) into equations on the real and imaginary axes through a set of so-called Langreth rules. In the following we discuss the details of the implementation in the superconducting phase.

## 9.2 IMPLEMENTATION IN THE SUPERCONDUCTING PHASE

*Discretization of the contour*

Similar to the equilibrium DMFT, the goal of NDMFT is to find a set of self-consistent $\{\hat{G}, \hat{\mathcal{G}}_0, \hat{\Sigma}\}$. The difference is that now these functions are defined on the Keldysh contour. It is found that the best strategy is to first determine these functions up to some time $t = T$, and then *propagate* the solution in time. This propagation is done on the "perimeter" along which the first variable is held fixed at the "present" real time $z = T$ and the second variable runs over the past times $z' \leqslant T$ as well as along the imaginary-time interval $[-i\beta, 0]$ (see FIGURE 33).

The algorithm, which has been discussed for example in Ref. [70], is based on a discretization of the real and imaginary axes:

$$t = m\Delta t \qquad m = 1, \ldots \tag{72}$$

$$\tau = m\Delta\tau \qquad m = 1, \ldots, N_\tau \qquad (N_\tau \Delta\tau = \beta). \tag{73}$$

When dealing with broken symmetry phases, the matrix structure of the Green's function leads to matricial Volterra integral equations (VIEs) and Volterra integro-differential equations (VIDEs). The extension was discussed in Ref. [74] in the context of the antiferromagnetic phase. In this regard, an important remark is in order. In the antiferromagnetic phase the "anomalous" component of the Green's function is of the form $\langle c_{i_a} c^\dagger_{j_b} \rangle$ with $i_a$ and $j_b$ denoting two sites on two different sublattices. These quantities are non-local and, as a consequence, the associated self-energy vanishes within DMFT. This leads to a matricial self-energy $\hat{\Sigma}$ which is actually diagonal. In this case, it is effective to decouple the matricial VIEs and VIDEs through new auxiliary functions and to solve the resulting set of "scalar" – as opposed to matricial – equations.

On the other hand, the superconducting Green's function have normal and anomalous components which are *both* local. In this case the self-energy is not diagonal and the above mentioned decoupling is not very effective. Therefore, we have to take a different approach, solving directly the VIE and the VIDE in a matricial form. In the following we discuss first the convolution of two matricial quantities on contour, then the algorithm for the VIE and finally for the VIDE.

*Contour convolutions in Nambu space*

The convolution of two functions of two variables living on the Keldysh contour is defined as:

$$\hat{A}(z, z') = \int_{\mathcal{C}} dz'' \, \hat{B}(z, z'') \hat{C}(z'', z'), \tag{74}$$

where in particular we are interested in the case in which $\hat{B}$ and $\hat{C}$ are either a Green's function, or a self- energy, or a convolution of a Green's function with a self-energy. In any case out of the four components $B_{11}$, $B_{12}$, $B_{21}$ and $B_{22}$ only two are independent. The following relations hold for Green's functions and self energies:

$$B^R_{22}(t, t') = -(B^R_{11}(t, t'))^* \tag{75a}$$

$$B^R_{12}(t, t') = \phantom{-}(B^R_{21}(t, t'))^* \tag{75b}$$

$$B^\urcorner_{22}(t, \tau) = -(B^\urcorner_{11}(t, \beta - \tau))^* \tag{75c}$$

$$B^\urcorner_{12}(t, \tau) = \phantom{-}(B^\urcorner_{21}(t, \beta - \tau))^* \tag{75d}$$

$$B^<_{12}(t, t') = -(B^<_{21}(t', t))^* \tag{75e}$$

$$B^M_{22}(\tau) = B^M_{11}(\beta - \tau) \tag{75f}$$

$$B^M_{12}(\tau) = (B^M_{21}(\tau))^* \tag{75g}$$

and for the lesser component:

$$B^{<}_{22}(t,t') = \begin{cases} -B^{<}_{11}(t',t) - B^{R}_{11}(t',t) & t < t', \\ (B^{<}_{11}(t,t'))^* + (B^{R}_{11}(t,t'))^* & t > t'. \end{cases} \tag{76}$$

The above relations are derived in such a way to involve only the retarded, lesser and left-mixing Keldysh components, which are the ones we choose as independent. For example, this is why Eq. (76) is written like this and not simply as $B^{<}_{22}(t,t') = (B^{>}_{11}(t,t'))^*$ which is valid for every $t$ and $t'$.

As a further technical detail, let us comment on the choice of the 11 and 21 components as independent. Eq. (74) often appears in expressions where $\hat{C}$ is some quantity to be determined via an integral equation involving $\hat{A}$. In this context, it is convenient to chooce as independent the components 11 and 21 because then Eq. (74) do not mix the other components of $\hat{A}$ and $\hat{C}$:

$$A_{11} = B_{11}C_{11} + B_{12}C_{21}, \tag{77}$$
$$A_{21} = B_{21}C_{11} + B_{22}C_{21}, \tag{78}$$

as opposed to other choices which would involve all the four components of $\hat{C}$.

Another very important point is that if, for example $\hat{B}$ is a Green's function and $\hat{C}$ a self-energy, then $\hat{A}$ is *neither* a Green's function *nor* a self-energy. As a consequence, the relations between its components are slightly but importantly different from Eqs. (75) and (76).

The relations between the Keldysh components ($A \leftrightarrow R$) and ($\urcorner \leftrightarrow \ulcorner$) are:

$$B^{A}_{11}(t,t') = (B^{R}_{11}(t',t))^* \tag{79a}$$
$$B^{A}_{21}(t,t') = B^{R}_{21}(t',t) \tag{79b}$$
$$B^{\ulcorner}_{11}(\tau,t) = (B^{\urcorner}_{11}(t,\beta-\tau))^* \tag{79c}$$
$$B^{\ulcorner}_{21}(\tau,t) = B^{\urcorner}_{21}(t,\tau). \tag{79d}$$

Finally, we can use the so-called Langreth rule to decompose the *contour* convolution in a set of three equations involving *real-time* and *imaginary-time* convolutions:

$$\hat{A}^{R}(t,t') = \int_{t'}^{t} dt''\, \hat{B}^{R}(t,t'')\hat{C}^{R}(t'',t') \tag{80}$$

$$\hat{A}^{\urcorner}(t,\tau) = \int_{0}^{t} dt''\, \hat{B}^{R}(t,t'')\hat{C}^{\urcorner}(t'',\tau) + \int_{0}^{\beta} d\tau'\, \hat{B}^{\urcorner}(t,\tau')\hat{C}^{M}(\tau'-\tau) \tag{81}$$

$$\hat{A}^{<}(t,t') = \int_{0}^{t} dt''\, \hat{B}^{R}(t,t'')\hat{C}^{<}(t'',t') + \int_{0}^{t'} dt''\, \hat{B}^{<}(t,t'')\hat{C}^{A}(t'',t') - i\int_{0}^{\beta} d\tau\, \hat{B}^{\urcorner}(t,\tau)\hat{C}^{\ulcorner}(\tau,t'). \tag{82}$$

Then we have to expand the matrix product and use the symmetry relations Eqs. (75), (76) and (79) and calculate explicitely the integrals. In practice, this is done on the discretized axes with some discrete approximation such as the trapezoid approximation, which is shown in the next section, as this is directly connected on how we solve the VIEs and VIDEs.

A final remark which is evident in Eqs. (80) is that if $\hat{C}$ was to be determined in an integral equation involving $\hat{A}$, then for a given Keldysh component, the role of the *kernel* of the integral equation is always taken by $\hat{B}^R$. In the following section we see how all this remarks are put in practice in the calculation of the VIE.

*Volterra integral equation in Nambu space*

For definitess, let us consider the Volterra integral equation we have to solve in the NDMFT algorithm in order to calculate the local Green's function $\hat{G}(z,z')$ starting from the knowledge of the Weiss field $\hat{\mathcal{G}}_0(z,z')$ and of the self-energy $\hat{\Sigma}(z,z')$:

$$\hat{G}(z,z') = \hat{\mathcal{G}}_0(z,z') + \int_{\mathcal{C}} dz''\, \hat{K}(z,z'')\hat{G}(z'',z') \tag{83}$$

$$\hat{K}(z,z') = \int_{\mathcal{C}} dz''\, \hat{\mathcal{G}}_0(z,z'')\hat{\Sigma}(z'',z') \tag{84}$$

We find here two examples of situations described in the previous section. First, it is important that since $\hat{K}$ is a convolution of a Green's function with a self energy, the relations among its matricial components are not the same as for Green's functions and self-energies. This has to be taken in particular care when computing the convolution of $\hat{K}$ with $\hat{G}$. Second, the first equation of the set shows how convenient is to take the 11 and 21 components of $\hat{G}$ as independent.

Having calculated $\hat{K}$ with the convolution showed in the previous section, to solve now the VIE we first use the Langreth rules to decompose Eq. (83) in the various Keldysh components $\hat{G}^X$ where the label X may stand for "retarded" (R), "left-mixing" ($\ulcorner$) or "lesser" ($<$):

$$\hat{G}^X(t,z') = \hat{Q}^X(t,z) + \int_{\mathcal{C}} dt''\, \hat{K}^R(t,t'')\hat{G}^X(t'',z'), \tag{85}$$

where:

$$\hat{Q}^R(t,t') = \hat{\mathcal{G}}_0^R(t,t') \tag{86a}$$

$$\hat{Q}^{\ulcorner}(t,\tau) = \hat{\mathcal{G}}_0^{\ulcorner}(t,\tau) + \int_0^\beta d\tau'\, \hat{K}^{\ulcorner}(t,\tau')\hat{G}^M(\tau'-\tau) \tag{86b}$$

$$\hat{Q}^<(t,t') = \hat{\mathcal{G}}_0^<(t,t') + \int_0^{t'} dt''\, \hat{K}^<(t,t'')\hat{G}^A(t'',t'), - i\int_0^\beta \hat{K}^{\ulcorner}(t,\tau)\hat{G}^{\urcorner}(\tau,t'). \tag{86c}$$

We have therefore gone from Eq. (83), which is a VIE with variables on contour, to Eqs. (85) which is a set of three VIEs on real-time axis.

The three VIEs are not independent but neither they are coupled (they do not have to be solved simultaneously). The equation for the lesser components involves also the retarded component (through the advanced component) and the left-mixing component (through the right-mixing component). Therefore we have to solve first the equations for the retarded and the left-mixing. These are actually independent from each other and from the other components (except for the Matsubara components which is known from the beginning of the calculation).

The next step is to discretize Eq. (85):

$$\hat{G}^{X}_{mn} = \hat{Q}^{X}_{mn} + \Delta t \sum_{i=1}^{m} w_i \hat{K}^{R}_{mi} \hat{G}^{X}_{in}. \tag{87}$$

According to the trapezoid approximation to integrals, $w_i = \frac{1}{2}$ on the edge of the interval of integration ($i = 1$ or $i = m$) and $w = 1$ otherwise. Eqs. (86) are discretized in the same way:

$$\hat{Q}^{R}_{mn} = (\hat{\mathcal{G}}^{R}_{0})_{mn} \tag{88}$$

$$\hat{Q}^{\urcorner}_{mn} = (\hat{\mathcal{G}}^{R}_{0})_{mn} + \Delta t \sum_{i=1} w_i \hat{K}^{\urcorner}_{m,i} \hat{G}^{M}_{in} \tag{89}$$

$$\hat{Q}^{<}_{mn} = (\hat{\mathcal{G}}^{R}_{0})_{mn} + \Delta\tau \sum_{i=1} w_i \hat{K}^{<}_{m,i} \hat{G}^{A}_{in} - i\Delta\tau \sum_{i=1}^{N_\tau+1} w_i \hat{K}^{\urcorner}_{mi} \hat{G}^{\ulcorner}_{in}. \tag{90}$$

Now we can single out the uknown term in the sum on the right hand side of Eq. (87) and take it to the left side to solve the equation. In other words, by discretizing, we have clearly reduced the integral equation to an algebraic equation:

$$(\mathbb{I} - \frac{\Delta t}{2} \hat{K}^{R}_{mm}) \hat{G}^{X}_{mn} = \hat{Q}^{X}_{mn} + \Delta t \sum_{i=1}^{m-1} w_i \hat{K}^{R}_{mi} \hat{G}^{X}_{in} \tag{91}$$

It is important to stress that this procedure does not imply any inversion of big matrices. The inversion is done in Nambu space and is merely a $2 \times 2$ matrix inversion which can be also done analytically.

*Volterra integro differential equation in Nambu space*

In our implementation we need to solve the following Volterra integro-differential equation to propagate the Weiss field $\hat{\mathcal{G}}_0(z, z')$:

$$i\partial_z \hat{\mathcal{G}}_0(z, z') = \mathbb{I}\delta(z, z') + \hat{\Sigma}_{HF}(z)\hat{\mathcal{G}}_0(z, z') + \int_{\mathcal{C}} dz''\, \hat{K}(z, z'')\hat{\mathcal{G}}_0(z'', z'), \tag{92}$$

where in our case the "kernel" $\hat{K}(z,z')$ is determined by the local Green's function $\hat{K}(z,z') = t^2\hat{\sigma}_3\hat{G}(z,z')\hat{\sigma}_3$. The algorithm is based on the following equation:

$$\hat{\mathcal{G}}_0(t,z') = \hat{\mathcal{G}}_0(t-\Delta t,z') + \int_{t-\Delta t}^{t} dt''\,\partial_{t''}\hat{\mathcal{G}}_0(t'',z'), \tag{93}$$

where the integral has to be discretized using for example the trapezoid rule:

$$(\hat{\mathcal{G}}_0^X)_{mn} = (\hat{\mathcal{G}}_0^X)_{m-1,n} + \frac{\Delta t}{2}\big((\partial_t\hat{\mathcal{G}}_0^X)_{m-1,n} + (\partial_t\hat{\mathcal{G}}_0^X)_{mn}\big), \tag{94}$$

where now clearly "$\partial_t$" is merely a simbol.

Analogously to what discussed above in the case of the VIE, we consider Eq. (92) for each Keldysh components separately:

$$i\partial_t\hat{\mathcal{G}}_0^X(t,z) = \hat{Q}^X(t,z) + \hat{\Sigma}(t)\hat{\mathcal{G}}_0^X(t,z) + \int_0^t dt'\,\hat{K}^R(t,t')\hat{\mathcal{G}}_0^X(t',z), \tag{95}$$

where:

$$\hat{Q}^R(t,t') = 0 \tag{96a}$$

$$\hat{Q}^{\rceil}(t,\tau) = \int_0^\beta d\tau'\,\hat{K}^{\rceil}(t,\tau')\hat{\mathcal{G}}_0^M(\tau'-\tau) \tag{96b}$$

$$\hat{Q}^{<}(t,t') = \int_0^{t'} dt''\,\hat{K}^{<}(t,t'')\hat{\mathcal{G}}_0^A(t'',t') - i\int_0^\beta \hat{K}^{\rceil}(t,\tau)\hat{\mathcal{G}}_0^{\lceil}(\tau,t'), \tag{96c}$$

and discretizing also this equation reads:

$$i(\partial_t\hat{\mathcal{G}}_0^X)_{mn} = \hat{Q}^X_{mn} + \hat{\Sigma}_m(\hat{\mathcal{G}}_0^X)_{mn} + \Delta t\sum_{i=1}^{m} w_i\hat{K}^R_{mi}(\hat{\mathcal{G}}_0^X)_{in}, \tag{97}$$

where, according to the trapezoid approximation to integrals, $w_i = \frac{1}{2}$ on the edge of the interval of integration ($i = 1$ or $i = m$) and $w = 1$ otherwise.

Analogously, Eqs. (96) are discretized:

$$\hat{Q}^{\rceil}_{mn} = \Delta t\sum_{i=1} w_i\hat{K}^{\rceil}_{m,i}(\hat{\mathcal{G}}_0^M)_{in}, \tag{98}$$

$$\hat{Q}^{<}_{mn} = \Delta\tau\sum_{i=1} w_i\hat{K}^{<}_{m,i}(\hat{\mathcal{G}}_0^A)_{in} - i\Delta\tau\sum_{i=1}^{N_\tau+1} w_i\hat{K}^{\rceil}_{mi}(\hat{\mathcal{G}}_0^{\lceil})_{in}, \tag{99}$$

so that plugging Eq. (97) into Eq. (94) we finally obtain:

$$\begin{aligned}(\hat{\mathcal{G}}_0^X)_{mn} = {}& \frac{\Delta t}{2}(\partial_t\hat{\mathcal{G}}_0^X)_{m-1,n} + (\hat{\mathcal{G}}_0^X)_{m-1,n} \\ & - i\frac{\Delta t}{2}(\hat{Q}^X_{mn} + \hat{\Sigma}_{HF}(\hat{\mathcal{G}}_0^X)_{mn} + \Delta t\sum_{i=1}^{m} w_i\hat{K}^R_{mi}(\hat{\mathcal{G}}_0^X)_{in}).\end{aligned} \tag{100}$$

At this point, analogously to the case of the VIE, we have a matricial algebraic equation and we can simply single out the uknown term $(\hat{\mathcal{G}}_0^{\mathrm{X}})_{mn}$ in the right hand side and take it on the left hand side to obtain:

$$\begin{aligned}(\mathbb{I} + i\frac{\Delta t}{2}\hat{\Sigma}_m + i\frac{\Delta t^2}{4}\hat{K}_{mm})(\hat{\mathcal{G}}_0^{\mathrm{X}})_{mn} = \\ = \frac{\Delta t}{2}(\partial_t \hat{\mathcal{G}}_0^{\mathrm{X}})_{m-1,n} + (\hat{\mathcal{G}}_0^{\mathrm{X}})_{m-1,n} - i\frac{\Delta t}{2}(\hat{Q}^{\mathrm{X}}_{mn} + \Delta t \sum_{i=1}^{m-1} w_i \hat{K}^{\mathrm{R}}_{mi}(\hat{\mathcal{G}}_0^{\mathrm{X}})_{in}).\end{aligned} \tag{101}$$

Finally, we can now invert the matrix on the left hand side and get the result. As a final passage, we may now go back to Eq; (97) and update the derivative.

# 10 QUENCH IN THE ATTRACTIVE HUBBARD MODEL

As a first application, we study a quantum quench of the interaction in the attractive Hubbard model and compare the result with a mean-field calculation on Bethe lattice at half-filling.

In FIGURE 34 we plot the order parameter following two different quenches. In the first case we increase the interaction strength from 2.2 to 3.0, in the second we decrease it from 2.0 to 1.9. The DMFT results are remarkably different from the static mean-field. In the two examples we show, we observe a rather large difference in the overall size of the superconducting order parameter. This can be at least qualitatively interpreted in terms of the equilibrium results discussed in the previous chapter, where the DMFT gives a smaller order parameter than mean-field because of the inclusion of quantum fluctuations, with the effect being largest in the intermediate region. For this reason we see large deviations especially in the second case of a quench where both the initial and the final interaction strengths lie in the intermediate range. In both cases we observe a change of the period of oscillation. Again, while in the first case the period is enhanced by a relatively small factor, in the second example of a quench, the period is increased by a factor of 4, signaling that a completely different energy scale controls the relaxation dynamics.

Similar trends are seen in the time evolution of the double occupancy shown in FIGURE 35. This is the main parameter measuring the effect of the quantum quench and the way the system relaxes – or not – to the equilibrium configuration. Moreover, we plot the total energy of the system. In principle, IPT is a non-conserving scheme in the sense that it does not guarantee that the conserved quantities of the original problem are actually conserved during the dyanmics.

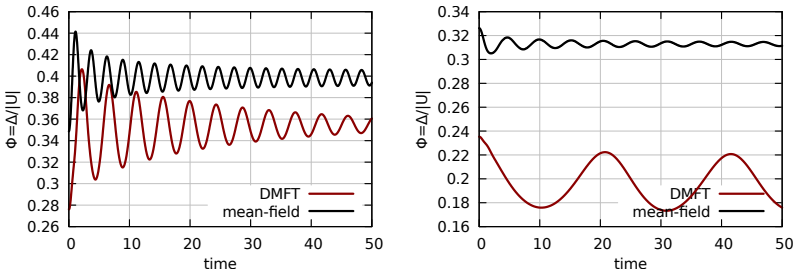


Figure 34: Superconducting order parameter after a quantum quench in the attractive Hubbard model from $U_i = -2.2$ to $U_f = -3.0$ (left) and from $U_i = -2.0$ to $U_f = -1.9$ (right). Time is in unit of $\frac{\hbar}{t}$ with $t$ the hopping.

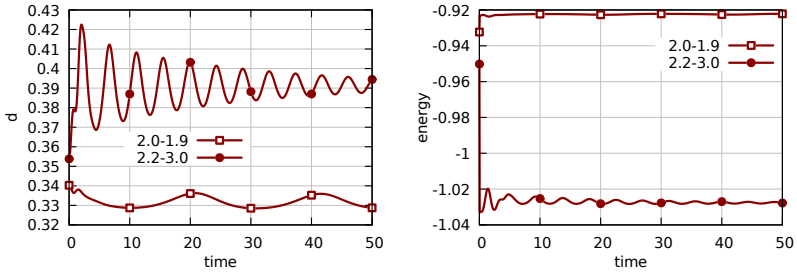


Figure 35: Double occupancy for the quenches in Figs. 34. Energy is in unit of t and time is in unit of $\frac{\hbar}{t}$ with t the hopping.

However, as shown in FIGURE 35, the energy after the quench is approximately conserved during the dynamics.

# Part IV

# APPENDIX

# A

# PROPERTIES OF d-WAVE SUPERCONDUCTORS

In this appendix we give the proofs of some relations used in the main text. In paricular, we derive the density of states of the quasiparticle excitations in the d-wave superconductor and the BCS Green's function in Matsubara time and frequency and in real time at equilibrium and out of equilibrium. Finally, we give the derivation of the results on the photoemission spectrum of an out-of-equilibrium superconductor in the approximation of a sudden change of the gap discussed in the main text.

## A.1 DENSITY OF STATES

The density of states is the integral in momentum space of the energy of excitations or quasi particle energy. As we have seen, it is convenient to describe this anisotropic superconductor in terms of the variables $\epsilon$ and $\phi$. Indeed The density of states in the normal phase is constant and equals $\rho_0$. Therefore we find:

$$\begin{aligned}\rho(E) &= \rho_0 \frac{2}{\pi}\int_0^{\frac{\pi}{2}} d\phi \int_0^{\infty} d\epsilon\, \delta(E-\sqrt{\epsilon^2+\Delta^2\cos^2\phi}) \\ &= \rho_0 \frac{2}{\pi} E \begin{cases} \int_0^{\frac{\pi}{2}} \frac{d\phi}{\sqrt{E^2-\Delta^2\cos^2\phi}} = \frac{1}{E}K(\frac{\Delta}{E}) & \text{if } E \geqslant \Delta \\ \int_{\arccos\frac{E}{\Delta}}^{\frac{\pi}{2}} \frac{d\phi}{\sqrt{E^2-\Delta^2\cos^2\phi}} = \frac{1}{\Delta}K(\frac{E}{\Delta}) & \text{if } E < \Delta, \end{cases}\end{aligned} \tag{102}$$

where $K(x) = \int_0^{2\pi} d\theta \frac{1}{\sqrt{1-x^2\sin^2\phi}}$ is the complete elliptic integral of the first kind.

In particular the important properties of the density of states are its singular behavior at the maximum value of the gap $\Delta$ where it diverges as:

$$\rho(E) \sim \frac{\rho_0}{\pi}\log\frac{\Delta}{|E-\Delta|} \text{for } E \sim \Delta^{\pm}, \tag{103}$$

and therefore it has a weaker divergence than in the conventional s-wave superconductor. Furthermore, the density of states is finite for every finite energy and goes to zero to zero energy linearly.

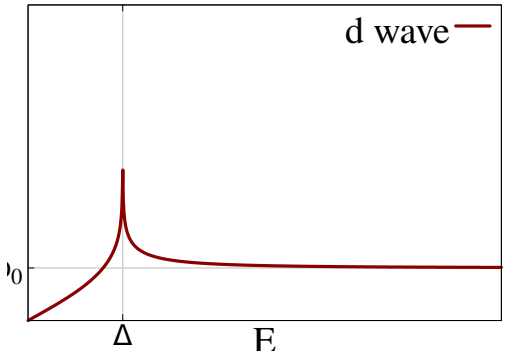


Figure 36: Density of states of the d-wave superconductor.

## A.2 MEAN-FIELD GREEN'S FUNCTIONS

*Properties of the Nambu Hamiltonian*

Let us take the mean-field Hamiltonian written in terms of the Nanbu spinors introduced in CHAPTER 4. Since in the following we will consider a given momentum $k$, we can omit this index:

$$\begin{aligned}\mathcal{H} &= \epsilon(c_\uparrow^\dagger c_\uparrow + c_\downarrow^\dagger c_\downarrow) - \Delta(c_\downarrow c_\uparrow + c_\uparrow^\dagger c_\downarrow^\dagger) \\ &= \begin{pmatrix} c_\uparrow^\dagger & c_\downarrow \end{pmatrix} \begin{pmatrix} \epsilon & -\Delta \\ -\Delta & -\epsilon \end{pmatrix} \begin{pmatrix} c_\uparrow \\ c_\downarrow^\dagger \end{pmatrix} \\ &= \gamma_\alpha^\dagger H_{\alpha\beta}\gamma_\beta = \gamma^\dagger \hat{H}\gamma\end{aligned} \tag{104}$$

The greek indeces denote the components in the space of Nambu and a sum is implicit when they compare in pairs. The matrix $\hat{H}$ is a matrix in the space of Nambu which can be expressed in terms of the Pauli matrices:

$$\hat{H} = \epsilon\hat{\sigma}_3 - \Delta\hat{\sigma}_1. \tag{105}$$

A part from being, together with the identity, a basis for the space of the complex $2 \times 2$ matrices, the Pauli matrices have very important and handy properties which are all consequences of:

$$\hat{\sigma}_i\hat{\sigma}_j = \delta_{ij}\mathbb{I} + i\varepsilon_{ijk}\hat{\sigma}_k \tag{106}$$

The matrix $\hat{H}$ satisfies analogous properties, which can be either checked by direct substitution or by noticing that:

$$\frac{\hat{H}}{E} = \cos 2\theta\hat{\sigma}_3 - \sin 2\theta\hat{\sigma}_1 = e^{i\theta\hat{\sigma}_2}\hat{\sigma}_3 e^{-i\theta\hat{\sigma}_2} \tag{107}$$

$$E^2 = \epsilon^2 + \Delta^2 = \hat{H}^2 = -\det\hat{H} \tag{108}$$

$$\cos 2\theta = \frac{\epsilon}{E} \quad \sin 2\theta = \frac{\Delta}{E}. \tag{109}$$

Therefore the matrix $\frac{\hat{H}}{E}$ satisfies all the properties of the Pauli matrices:

$$\left(\frac{\hat{H}}{E}\right)^2 = \mathbb{I} \tag{110}$$

$$(\mathbb{I} \pm \frac{\hat{H}}{E})(\mathbb{I} \pm \frac{\hat{H}}{E}) = (\mathbb{I} \pm \frac{\hat{H}}{E})^2 = 2(\mathbb{I} \pm \frac{\hat{H}}{E}) \tag{111}$$

$$(\mathbb{I} \pm \frac{\hat{H}}{E})(\mathbb{I} \mp \frac{\hat{H}}{E}) = 0 \tag{112}$$

$$e^{-i\hat{H}t} = \cos(Et)\mathbb{I} - i\sin(Et)\frac{\hat{H}}{E} = \frac{e^{iEt}(\mathbb{I} - \frac{\hat{H}}{E})}{2} + \frac{e^{-iEt}(\mathbb{I} + \frac{\hat{H}}{E})}{2} \tag{113}$$

$$e^{-\hat{H}\tau} = \cosh(E\tau)\mathbb{I} - \sinh(E\tau)\frac{\hat{H}}{E} = \frac{e^{E\tau}(\mathbb{I} - \frac{\hat{H}}{E})}{2} + \frac{e^{-E\tau}(\mathbb{I} + \frac{\hat{H}}{E})}{2} \tag{114}$$

$$\frac{e^{-\frac{\beta\hat{H}}{2}}}{\cosh\beta\frac{E}{2}} = \mathbb{I} - \tanh(\frac{\beta E}{2})\frac{\hat{H}}{E} = \frac{f(-E)(\mathbb{I} - \frac{\hat{H}}{E})}{2} + \frac{f(E)(\mathbb{I} + \frac{\hat{H}}{E})}{2}, \tag{115}$$

where $f(E)$ is the Fermi distribution and we have added Eq. (115) because it follows directly from Eq. (114) and because it is the well known result for the Matsubara Green's function of the superconductor in $\tau = 0^-$.

*Mean-field evolution of Nambu spinors*

The components of the Nambu spinors clearly satisfy the usual fermionic anticommutation rules

$$\{\gamma_\alpha, \gamma_\beta^\dagger\} = \delta_{\alpha\beta} \tag{116}$$

$$\{\gamma_\alpha, \gamma_\beta\} = 0 \tag{117}$$

When there is no risk to be confused, one can write Eq. (116) directly as $\{\gamma, \gamma^\dagger\} = \mathbb{I}$. The equations of evolution in imaginary and real time naturally follow

$$\gamma_\alpha(\tau) = e^{\mathcal{H}\tau}\gamma_\alpha e^{-\mathcal{H}\tau} \tag{118a}$$

$$-\partial_\tau\gamma_\alpha(\tau) = [\gamma_\alpha, \mathcal{H}] = H_{\alpha\beta}\gamma_\beta \tag{118b}$$

$$\gamma_\alpha(\tau) = e^{-\hat{H}\tau}\gamma_\alpha \tag{118c}$$

and analogously *if* $\hat{H}$ *is constant*

$$\gamma(t) = e^{i\mathcal{H}t}\gamma e^{-i\mathcal{H}t} = e^{-i\hat{H}t}\gamma \tag{119}$$

where as we announced previously we omit the Nambu index because no confusion can arise.

*Matsubara Green's function*

From Eqs. (118) it follows also

$$e^{-\beta\mathcal{H}}\gamma = e^{\beta\hat{H}}\gamma e^{-\beta\mathcal{H}} \tag{120}$$

from which

$$\begin{aligned}\langle\gamma\gamma^\dagger\rangle =& \frac{\mathrm{Tr}\left(e^{-\beta\mathcal{H}}\gamma\gamma^\dagger\right)}{\mathcal{Z}} \\ =& \frac{e^{\beta\hat{H}}\mathrm{Tr}\left(\gamma e^{-\beta\mathcal{H}}\gamma^\dagger\right)}{\mathcal{Z}} \\ =& e^{\beta\hat{H}}(1-\langle\gamma\gamma^\dagger\rangle)\end{aligned} \tag{121}$$

therefore

$$\langle\gamma\gamma^\dagger\rangle = e^{\beta\hat{H}}(1+e^{\beta\hat{H}})^{-1} = \frac{e^{\frac{\beta\hat{H}}{2}}}{2\cosh\frac{\beta E}{2}} \tag{122}$$

and

$$\langle\gamma^\dagger\gamma\rangle = \mathbb{I} - \langle\gamma\gamma^\dagger\rangle = \frac{e^{-\frac{\beta\hat{H}}{2}}}{2\cosh\frac{\beta E}{2}} \tag{123}$$

which naturally coincides, through Eq. (115) with the very well known results from the BCS theory at finite temperature. Finally, we obtain the Matsubara Green's function through Eq. (118)

$$\hat{G}(\tau) = -\langle T_\tau\gamma(\tau)\gamma^\dagger\rangle = \begin{cases} \frac{e^{-(\tau-\frac{\beta\hat{H}}{2})}}{2\cosh\frac{\beta E}{2}} & \tau > 0 \\ \frac{e^{-(\tau+\frac{\beta\hat{H}}{2})}}{2\cosh\frac{\beta E}{2}} & \tau < 0 \end{cases} \tag{124}$$

*Equilibrium real-time Green's function*

From Eq. (119) we obtain

$$\hat{G}^<(t,t') = e^{-i\hat{H}t}\hat{G}^<(0,0)e^{i\hat{H}t'} \tag{125}$$

which is valid if $\hat{H}$ and therefore $\mathcal{H}$ are constant. At equilibrium, moreover, we will have that $\hat{G}^<(0,0) = i\hat{G}(\tau = 0^-)$ and as derived in the previous section this commutes with $e^{i\hat{H}t}$ therefore in this case

$$\hat{G}^<(t,t') = e^{-i\hat{H}(t-t')}\hat{G}^<(0,0) \tag{126}$$

and using

$$\frac{1}{2\pi}\int e^{i\omega t}e^{-i\hat{H}t}\,dt = \frac{\delta(\omega+E)(\mathbb{I}-\frac{\hat{H}}{E})}{2} + \frac{\delta(\omega-E)(\mathbb{I}+\frac{\hat{H}}{E})}{2} \tag{127}$$

and

$$-i\hat{G}^{<}(\omega) = \frac{1}{2\pi}\int e^{i\omega t}e^{-i\hat{H}t}\hat{G}^{<}(0,0)$$
$$= \frac{f(-E)\delta(\omega+E)(\mathbb{I}-\frac{\hat{H}}{E})}{2} + \frac{f(E)\delta(\omega-E)(\mathbb{I}+\frac{\hat{H}}{E})}{2} \quad (128)$$

where we have used the properties of the matrix $\frac{\hat{H}}{E}$.

Therefore at equilibrium

$$Z^{\pm} = f(\pm E)(\mathbb{I}\pm\frac{\hat{H}}{E}) \quad (129)$$

*Out-of-equilibrium real-time Green's function with $\Delta = const.$*

$$\hat{G}^{<}(\omega,t') = \frac{1}{2\pi}\int d\tau\, e^{i\omega\tau}\hat{G}^{<}(\tau+t',t')$$
$$= \frac{e^{-i\omega t'}}{2\pi}\int d\tau\, e^{i\omega\tau}e^{-i\hat{H}\tau}\hat{G}^{<}(0,0)e^{i\hat{H}t'}$$
$$= [\frac{e^{iEt'}\delta(\omega+E)(\mathbb{I}-\frac{\hat{H}}{E})}{2} + \frac{e^{-iEt'}\delta(\omega-E)(\mathbb{I}+\frac{\hat{H}}{E})}{2}]\times$$
$$\frac{i}{2}(\mathbb{I}-\tanh\frac{\beta E_0}{2}\frac{\hat{H}_0}{E_0})\times$$
$$[\frac{e^{-iEt'}(\mathbb{I}-\frac{\hat{H}}{E})}{2} + \frac{e^{iEt'}(\mathbb{I}+\frac{\hat{H}}{E})}{2}] \quad (130)$$

In the previous expression there are terms which are constant and terms which oscillates with frequency $\omega = 2E$. These terms obviously average to zero over one period. Let us concentrate therefore on the constant terms. In other words, we may define a $\hat{G}^{<}(\omega)_{neq} = \frac{1}{T}\int_t^{t+T}\hat{G}^{<}(\omega,t')\,dt'$ where we have added the subscript "neq" to distinguish ti from the equilibrium expression to which, as we will see in a moment, it reduces when $\Delta_0 = \Delta$

$$\hat{G}^{<}_{neq}(\omega) = \frac{i}{8}\delta(\omega+E)(\mathbb{I}-\frac{\hat{H}}{E})(\mathbb{I}-\tanh\frac{\beta E_0}{2}\frac{\hat{H}_0}{E_0})(\mathbb{I}-\frac{\hat{H}}{E})$$
$$+\frac{i}{8}\delta(\omega-E)(\mathbb{I}+\frac{\hat{H}}{E})(\mathbb{I}-\tanh\frac{\beta E_0}{2}\frac{\hat{H}_0}{E_0})(\mathbb{I}+\frac{\hat{H}}{E})$$
$$= \frac{i}{2}\delta(\omega+E)(\mathbb{I}-\frac{\hat{H}}{E})(\frac{1}{2}+\tanh\frac{\beta E_0}{2}\frac{\epsilon^2+\Delta_0\Delta}{2EE_0})$$
$$+\frac{i}{2}\delta(\omega-E)(\mathbb{I}+\frac{\hat{H}}{E})(\frac{1}{2}-\tanh\frac{\beta E_0}{2}\frac{\epsilon^2+\Delta_0\Delta}{2EE_0}) \quad (131)$$

In the previous derivation we have used a few relations

$$\hat{H}\hat{H}_0 = \epsilon^2 + \Delta\Delta_0 + i\epsilon\hat{\sigma}_2(\Delta - \Delta_0) \tag{132}$$

$$[\hat{H}, \hat{H}_0] = 2i\epsilon\hat{\sigma}_2(\Delta - \Delta_0) \tag{133}$$

$$\{\hat{H}, \hat{H}_0\} = 2(\epsilon^2 + \Delta\Delta_0) \tag{134}$$

$$\hat{H}\hat{H}_0\hat{H} = [\hat{H}, \hat{H}_0]\hat{H} + \hat{H}_0\hat{H}^2 = [\hat{H}, \hat{H}_0]\hat{H} + \hat{H}_0 E^2 \tag{135}$$

$$= \{\hat{H}, \hat{H}_0\}\hat{H} - \hat{H}_0\hat{H}^2 = \{\hat{H}, \hat{H}_0\}\hat{H} - \hat{H}_0 E^2 \tag{136}$$

Therefore we obtain the result discussed in the main text

$$\hat{Z}^{\pm}_{neq} = (\mathbb{I} \pm \frac{\hat{H}}{E})(\frac{1}{2} \mp \tanh\frac{\beta E_0}{2}\frac{\epsilon^2 + \Delta_0\Delta}{2EE_0}) \tag{137}$$

## A.3 EFFECT OF THE FINITE WIDTH OF THE PROBE

To properly include the effects of the finite probe width we need to consider

$$\begin{aligned}\hat{I}(\omega, t_0) &= \mathrm{Im}\frac{1}{(2\pi)^2}\int dt \int dt'\, e^{i\omega(t-t')} s_{t_0}(t) s_{t_0}(t')\hat{G}^<(t,t') \\ &= \underbrace{\frac{1}{2\pi}\int dt\, s_{t_0}(t) e^{i\omega t} e^{-i\hat{H}t}}_{\hat{A}(\omega,t_0)}\, \hat{G}^<(0,0)\hat{A}^\dagger(\omega, t_0)\end{aligned} \tag{138}$$

and the photoemission spectrum will be clearly given by the 11 component of this expression. For example $s_{t_0}(t)$ can be taken as a gaussian centred in $t_0$ and with a width $t_0$. It is obtained

$$\hat{A}(\omega, t_0) = \tilde{s}_{t_0}(\omega + E)\frac{\mathbb{I} - \frac{\hat{H}}{E}}{2} + \tilde{s}_{t_0}(\omega - E)\frac{\mathbb{I} + \frac{\hat{H}}{E}}{2} \tag{139}$$

where $\tilde{s}_{t_0}(\omega)$ is the Fourier tranform of the probe pulse envelope. This expression clearly reduces to Eq. (127) in the limit of continuos probe, as it is suitable for the equilibrium photoemission, $s_{t_0}(t) = 1$, or in other words for infinite $t_0$, in the case $\tilde{s}_{t_0}(\omega) = \delta(\omega)$.

Then with similar algebraic passages as before, one obtains

$$\begin{aligned}\hat{I}(\omega, t_0) &= (\tilde{s}_{t_0}(\omega + E))^2\frac{\mathbb{I} - \frac{\hat{H}}{E}}{2}(\frac{1}{2} + \tanh\frac{\beta E_0}{2}\frac{\epsilon^2 + \Delta\Delta_0}{2EE_0}) \\ &(\tilde{s}_{t_0}(\omega - E))^2\frac{\mathbb{I} + \frac{\hat{H}}{E}}{2}(\frac{1}{2} - \tanh\frac{\beta E_0}{2}\frac{\epsilon^2 + \Delta\Delta_0}{2EE_0}) \\ &\quad - 4\tilde{s}_{t_0}(\omega - E)\tilde{s}_{t_0}(\omega + E)\tanh\beta E_0 2\frac{\epsilon(\Delta - \Delta_0)(\epsilon\hat{\sigma}_1 + \Delta\hat{\sigma}_3}{E^2 E_0})\end{aligned} \tag{140}$$

That is, the result is essentially unchanged with the change that the $\delta$-peaks turn into the $\tilde{s}_{t_0}(\omega)$ which are clearly gaussians. There is also the appareance of a term which goes to zero for infinitely narrow $\tilde{s}_{t_0}$ and is anyways very small because it is proportional to the product of two gaussians centered around different points.

# B

# DETAILS OF NONEQUILIBRIUM DYNAMICAL MEAN-FIELD THEORY

In this appendix we give a brief introduction to the idea of many-body perturbation theory (MBPT) on Keldysh contour and we give the derivation of the equations for the kinetic energy within NDMFT.

## B.1 THE IDEA OF THE CONTOUR

Suppose we are given a time-dependent Hamiltonian $\mathcal{H}(t)$ and want to calculate some observable as a function of time. Moreover, suppose that at some time $t = 0$ the system is in thermal equilibrium or, in other words, that the density matrix is the usual Gibbs ensemble. We may be interested for example in one-particle observables, and therefore want to calculate the lesser Green's function

$$\begin{aligned} i\hat{G}^{<}(t,t') &= \langle \gamma^{\dagger}(t')\gamma(t)\rangle = \\ &\mathrm{Tr}\left(e^{-\beta\mathcal{H}(0)}U_{\mathcal{H}}^{-1}(t',0)\gamma^{\dagger}U_{\mathcal{H}}(t',0)U_{\mathcal{H}}^{-1}(t,0)\gamma U_{\mathcal{H}}(t,0)\right) \end{aligned} \tag{141}$$

where $U_{\mathcal{H}}(t,t')$ is the unitary time-evolution operator. Eq. (141) already suggests the idea of a "contour". Indeed, read from right to left we have the propagation up to time $t$, the evaluation of $\gamma$, another evolution from $t$ to $t'$ and finally, after the evaluation of $\gamma^{\dagger}$, the evolution *back* to time zero.

Now, at equilibrium at $T = 0$ the workaround not to consider the contour is to say that actually the evolution back to time is equivalent to an evolution to infinite time, multiplied by a phase factor. In the Matsubara MBPT on the other hand, one consider the evolution on the imaginary-time axis.

Out of equilibrium we cannot use these workarounds and we have to deal with the contour. Moreover, this contour is "extended" to the imaginary-time interval $[0,-i\beta]$ to account for the term $e^{-\beta\mathcal{H}(0)}$.

Without entering into much details, if we now split the Hamiltonian into a free term and an interacting term $\mathcal{H}_0 + \mathcal{H}_i$ we can rewrite

$$U_{\mathcal{H}}(t,t') = U_{\mathcal{H}_0}(t,t')S_{\mathcal{H}\mathcal{H}_0}(t,t') \tag{142}$$

$$e^{-\beta\mathcal{H}(0)} = e^{-\beta\mathcal{H}_0(0)}\, S_{\mathcal{H}\mathcal{H}_0}(-i\beta,0) \tag{143}$$

where the operator $S_{\mathcal{H}\mathcal{H}_0}(t,t')$ is suitable for an expansion in powers of the interaction. Finally, Eq. (141) becomes

$$\begin{aligned}
&i\hat{G}^{<}(t,t') = \mathrm{Tr}\left(e^{-\beta\mathcal{H}_0(0)} S_{\mathcal{H}\mathcal{H}_0}(-i\beta,0)\times\right.\\
&\left. S^{-1}_{\mathcal{H}\mathcal{H}_0}(t',0)\gamma^{\dagger}_{\mathcal{H}_0}(t) S_{\mathcal{H}\mathcal{H}_0}(t',t)\gamma_{\mathcal{H}_0}(t) S_{\mathcal{H}\mathcal{H}_0}(t,0)\right)\\
&= \mathrm{Tr}\left(e^{-\beta\mathcal{H}_0(0)} \mathrm{T}_{\mathcal{C}}(S_{\mathcal{H}\mathcal{H}_0}(-i\beta,0)\gamma_{\mathcal{H}_0}(z)\gamma^{\dagger}_{\mathcal{H}_0}(z'))_{\substack{z=t\in\mathcal{C}_1\\ z=t'\in\mathcal{C}_2}}\right)\\
&= \hat{G}(z,z')|_{\substack{z=t\in\mathcal{C}_1\\ z=t\in\mathcal{C}_2}}
\end{aligned} \tag{144}$$

where $\gamma_{\mathcal{H}}$ denote the Heisenberg representation of the operator and the ordering operator on contour $\mathrm{T}_{\mathcal{C}}$ is introduced.

## B.2 KINETIC ENERGY

The kinetic energy of the original lattice problem is clearly defined as the average of the kinetic term of the latiice Hamiltonian

$$K = -t\sum_{ij\sigma}\langle c^{\dagger}_{i\sigma}c_{j\sigma}\rangle = \sum_{\sigma}\int_{-W}^{W} d\epsilon\,\rho(\epsilon)\,\langle c^{\dagger}_{\epsilon\sigma}c_{\epsilon\sigma}\rangle \tag{145}$$

$\rho(\epsilon) = \frac{2}{\pi W^2}\sqrt{W^2-\epsilon^2}$ is the density of states of the single particle kinetic energy. It is somewhat surprising that this quantity can be expressed in terms of the local Green's function only. To this scope, we have to make use of the following relations

$$\hat{G}^{-1}_{\epsilon}(i\omega) = i\omega\mathbb{I} - \epsilon\hat{\sigma}_3 - \hat{\Sigma}(i\omega) \tag{146}$$

$$\hat{\mathcal{G}}^{-1}_{0}(i\omega) = i\omega\mathbb{I} - \hat{\Delta}(i\omega) = \hat{G}(i\omega)^{-1} + \hat{\Sigma}(i\omega) \tag{147}$$

which imply

$$\epsilon\hat{\sigma}_3 = \hat{G}^{-1}(i\omega) + \hat{\Delta}(i\omega) - \hat{G}^{-1}_{\epsilon}(i\omega) \tag{148}$$

Therefore one can write

$$\begin{aligned}
K &= \int_{-W}^{W} d\epsilon\,\rho(\epsilon)\sum_{\sigma}\langle c^{\dagger}_{\epsilon\sigma}c_{\epsilon\sigma}\rangle = \int_{-W}^{W} d\epsilon\,\rho(\epsilon)\mathrm{Tr}\left(\epsilon\hat{\sigma}_3\hat{G}(\tau=0^-)\right)\\
&= \int_{-W}^{W} d\epsilon\,\rho(\epsilon)\frac{1}{\beta}\sum_{i\omega_n}\mathrm{Tr}\left(\epsilon\hat{\sigma}_3\hat{G}(i\omega_n)\right)\\
&= \int_{-W}^{W} d\epsilon\,\rho(\epsilon)\frac{1}{\beta}\sum_{i\omega_n}\mathrm{Tr}\left((\hat{G}^{-1}(i\omega)+\hat{\Delta}(i\omega)-\hat{G}^{-1}_{\epsilon}(i\omega))\hat{G}(i\omega_n)\right)\\
&= \frac{1}{\beta}\sum_{i\omega_n}\mathrm{Tr}\left(\hat{\Delta}(i\omega)\hat{G}(i\omega_n)\right) = \int_0^{\beta} d\tau\,\mathrm{Tr}\left(\hat{\Delta}(\tau)\hat{G}(-\tau)\right)\\
&= t^2\int_0^{\beta} d\tau\,\mathrm{Tr}\left(\hat{\sigma}_3\hat{G}(\tau)\hat{\sigma}_3\hat{G}(-\tau)\right) = -2t^2\int_0^{\beta} d\tau\,(G(\tau)G(\beta-\tau)+F^2(\tau))
\end{aligned}$$

(149)

Out of equilibrium the derivation is conceptually the same but is complicated by the impossibility of going to Fourier space transforming convolutions and derivatives in products. Therefore we have to make use of the differential version of Eqs. (146) and (147).

$$i\partial_z \hat{G}_\epsilon(z,z') = \delta(z,z')\mathbb{I} + \epsilon\hat{\sigma}_3\hat{G}_\epsilon(z,z') + \int_{\mathcal{C}} dz''\, \hat{\Sigma}(z,z'')\hat{G}_\epsilon(z'',z') \tag{150}$$

$$i\partial_z \hat{\mathcal{G}}_0(z,z') = \delta(z,z')\mathbb{I} + \int_{\mathcal{C}} dz''\, \hat{\Delta}(z,z'')\hat{\mathcal{G}}_0(z'',z') \tag{151}$$

$$\hat{\mathcal{G}}_0(z,z') = \hat{G}(z,z') - \int_{\mathcal{C}} dz'' \int_{\mathcal{C}} dz'''\, \hat{\mathcal{G}}_0(z,z'')\hat{\Sigma}(z'',z''')\hat{G}(z''',z') \tag{152}$$

Now we integrate Eq. (150)

$$i\partial_z \hat{G}(z,z') = \delta(z,z')\mathbb{I} + \int_{-W}^{W} d\epsilon\, \rho(\epsilon)\epsilon\hat{\sigma}_3\hat{G}_\epsilon + \int_{\mathcal{C}} dz''\, \hat{\Sigma}(z,z'')\hat{G}(z'',z') \tag{153}$$

then we take the derivative of Eq. (152) and plug it into Eq. (151) and finally obtain while taking the derivative of the third equation we get

$$\int_{-W}^{W} d\epsilon\, \rho(\epsilon)\epsilon\hat{\sigma}_3\hat{G}_\epsilon = \int_{\mathcal{C}} dz''\, \hat{\Delta}(z,z'')\hat{G}(z'',z') = t^2 \int_{\mathcal{C}} dz''\, \hat{\sigma}_3\hat{G}(z,z'')\hat{\sigma}_3\hat{G}(z'',z') \tag{154}$$

Therefore the kinetic energy reads

$$\begin{aligned}
K(t) &= -i\int_{-W}^{W} d\epsilon\, \rho(\epsilon)\mathrm{Tr}\left(\epsilon\hat{\sigma}_3\hat{G}^<_\epsilon(t,t)\right) \\
&= -it^2\Big[\int_{\mathcal{C}} dz''\, \mathrm{Tr}\left(\hat{\sigma}_3\hat{G}(z,z'')\hat{\sigma}_3\hat{G}(z'',z')\right)\Big]_{\substack{z=t\in\mathcal{C}_1 \\ z=t\in\mathcal{C}_2}} \\
&= -i\int \mathrm{Tr}\left(\hat{\Delta}^R(t,t')\hat{G}^<(t',t)\right)dt' - i\int \mathrm{Tr}\left(\hat{\Delta}^<(t,t')\hat{G}^A(t',t)\right)dt' \\
&\quad + \int d\tau\, \mathrm{Tr}\left(\hat{\Delta}^\urcorner(t,\tau)\hat{G}^\ulcorner(\tau,t)\right) \\
&= 2\int \mathrm{Im}\Big((\hat{\Delta}^R_{11}(t,t'))^*\hat{G}^<_{11}(t,t') + (\hat{\Delta}^R_{21}(t,t'))^*\hat{G}^<_{21}(t,t') \\
&\qquad + \hat{\Delta}^<_{11}(t,t')(\hat{G}^R_{11}(t,t'))^* + \hat{\Delta}^<_{21}(t,t')(\hat{G}^R_{21}(t,t'))^*\Big) \\
&\quad - 2\int_0^\beta \mathrm{Re}\Big(\hat{\Delta}^\urcorner_{11}(t,\tau)(\hat{G}^\urcorner_{11}(t,\beta-\tau))^* + \hat{\Delta}^\urcorner_{21}(t,\tau)(\hat{G}^<_{21}(t,\beta-\tau))^*\Big)
\end{aligned} \tag{155}$$

# BIBLIOGRAPHY


[1] J. R. Schrieffer, *Theory of superconductivity* (Advanced Book Program, Perseus Books, 1983), 354 pp.

[2] J. G. Bednorz and K. A. Müller, "Possible high $T_c$ superconductivity in the Ba-La-Cu-O system," Zeitschrift für Physik B Condensed Matter **64**, 189–193 (1986).

[3] J. Bardeen, L. N. Cooper, and J. R. Schrieffer, "Theory of superconductivity," Physical Review **108**, 1175–1204 (1957).

[4] L. N. Cooper, "Bound electron pairs in a degenerate fermi gas," Physical Review **104**, 1189–1190 (1956).

[5] B. Keimer, S. A. Kivelson, M. R. Norman, S. Uchida, and J. Zaanen, "From quantum matter to high-temperature superconductivity in copper oxides," Nature **518**, 179–186 (2015).

[6] A. B. Migdal, "Interaction between electrons and lattice vibrations in a normal metal," Sov. Phys. JETP **7**, 996–1001 (1958).

[7] G. M. Eliashberg, "Interactions between electrons and lattice vibrations in a superconductor," Sov. Phys. JETP **11** (1960).

[8] M. Capone, M. Fabrizio, C. Castellani, and E. Tosatti, "Strongly correlated superconductivity," Science **296**, 2364–2366 (2002).

[9] D. J. Scalapino, "A common thread: the pairing interaction for unconventional superconductors," Reviews of Modern Physics **84**, 1383–1417 (2012).

[10] P. Monthoux, D. Pines, and G. G. Lonzarich, "Superconductivity without phonons," Nature **450**, 1177–1183 (2007).

[11] P. A. Lee, N. Nagaosa, and X.-G. Wen, "Doping a mott insulator: physics of high-temperature superconductivity," Reviews of Modern Physics **78**, 17–85 (2006).

[12] P. W. Anderson, "The resonating valence bond state in $La_2CuO_4$ and superconductivity," Science **235**, 1196–1198 (1987).

[13] G. Kotliar, "Resonating valence bonds and d-wave superconductivity," Physical Review B **37**, 3664–3666 (1988).

[14] G. Kotliar and J. Liu, "Superexchange mechanism and d-wave superconductivity," Physical Review B **38**, 5142 (1988).

[15] F. Cilento et al., "Photo-enhanced antinodal conductivity in the pseudogap state of high-$T_c$ cuprates," Nature Communications **5**, 4353 (2014).

[16] C. C. Tsuei and J. R. Kirtley, "Pairing symmetry in cuprate superconductors," Reviews of Modern Physics **72**, 969–1016 (2000).

[17]W. S. Lee, I. M. Vishik, K. Tanaka, D. H. Lu, T. Sasagawa, N. Nagaosa, T. P. Devereaux, Z. Hussain, and Z.-X. Shen, "Abrupt onset of a second energy gap at the superconducting transition of underdoped Bi2212," Nature **450**, 81–84 (2007).

[18]J. Annett, N. Goldenfeld, and S. R. Renn, "Interpretation of the temperature dependence of the electromagnetic penetration depth in $YBa_2Cu_3O_{7-\delta}$," Physical Review B **43**, 2778–2782 (1991).

[19]W. N. Hardy, D. A. Bonn, D. C. Morgan, R. Liang, and K. Zhang, "Precision measurements of the temperature dependence of $\lambda$ in $YBa_2Cu_3O_{7-\delta}$: strong evidence for nodes in the gap function," Physical Review Letters **70**, 3999–4002 (1993).

[20]A. Damascelli, Z. Hussain, and Z.-X. Shen, "Angle-resolved photoemission studies of the cuprate superconductors," Reviews of modern physics **75**, 473 (2003).

[21]J. Mesot, M. R. Norman, H. Ding, M. Randeria, J. C. Campuzano, A. Paramekanti, H. M. Fretwell, A. Kaminski, T. Takeuchi, T. Yokoya, et al., "Superconducting gap anisotropy and quasiparticle interactions: a doping dependent photoemission study," Physical review letters **83**, 840 (1999).

[22]D. J. Van Harlingen, "Phase-sensitive tests of the symmetry of the pairing state in the high-temperature superconductors - evidence for $d_{x^2-y^2}$ symmetry," Reviews of Modern Physics **67**, 515–535 (1995).

[23]V. V. Kabanov, J. Demsar, B. Podobnik, and D. Mihailovic, "Quasiparticle relaxation dynamics in superconductors with different gap structures: theory and experiments on $YBa_2Cu_3O_{7-\delta}$," Physical Review B **59**, 1497–1506 (1999).

[24]M. Keller, W. Metzner, and U. Schollwöck, "Dynamical mean-field theory for pairing and spin gap in the attractive hubbard model," Physical Review Letters **86**, 4612–4615 (2001).

[25]M. Capone, C. Castellani, and M. Grilli, "First-order pairing transition and single-particle spectral function in the attractive hubbard model," Physical Review Letters **88**, 126403 (2002).

[26]A. Toschi, M. Capone, and C. Castellani, "Energetic balance of the superconducting transition across the BCS-bose einstein crossover in the attractive hubbard model," Physical Review B **72**, 235118 (2005).

[27]J. Zhang and R. D. Averitt, "Dynamics and control in complex transition metal oxides," Annual Review of Materials Research **44**, 19–43 (2014).

[28]S. Dal Conte et al., "Disentangling the electronic and phononic glue in a high-tc superconductor," Science **335**, 1600–1603 (2012).

[29]S. Dal Conte et al., "Snapshots of the retarded interaction of charge carriers with ultrafast fluctuations in cuprates," Nature Physics **11**, 421–426 (2015).

[30]R. D. Averitt and A. J. Taylor, "Ultrafast optical and far-infrared quasiparticle dynamics in correlated electron materials," Journal of Physics: Condensed Matter **14**, R1357 (2002).

[31]J. Orenstein, "Ultrafast spectroscopy of quantum materials," Physics Today **65**, 44 (2012).

[32]C. Giannetti, M. Capone, D. Fausti, M. Fabrizio, F. Parmigiani, and D. Mihailovic, "Ultrafast optical spectroscopy of strongly correlated materials and high-temperature superconductors: a non-equilibrium approach," Advances in Physics **65**, 58–238 (2016).

[33]G. Coslovich et al., "Competition between the pseudogap and superconducting states of $Bi_2Sr_2Ca_{0.92}\mathbf{Y}_{0.08}Cu_2\mathbf{O}_{8+\delta}$ single crystals revealed by ultrafast broadband optical reflectivity," Physical Review Letters **110**, 107003 (2013).

[34]A. Rothwarf and B. N. Taylor, "Measurement of recombination lifetimes in superconductors," Physical Review Letters **19**, 27 (1967).

[35]K. Matsuda, I. Hirabayashi, K. Kawamoto, T. Nabatame, T. Tokizaki, and A. Nakamura, "Femtosecond spectroscopic studies of the ultrafast relaxation process in the charge-transfer state of insulating cuprates," Physical Review B **50**, 4097–4101 (1994).

[36]F. Novelli et al., "Witnessing the formation and relaxation of dressed quasi-particles in a strongly correlated electron system," Nature Communications **5**, 5112 (2014).

[37]P. B. Allen, "Theory of thermal relaxation of electrons in metals," Physical Review Letters **59**, 1460–1463 (1987).

[38]C. L. Smallwood, J. P. Hinton, C. Jozwiak, W. Zhang, J. D. Koralek, H. Eisaki, D.-H. Lee, J. Orenstein, and A. Lanzara, "Tracking cooper pairs in a cuprate superconductor by ultrafast angle-resolved photoemission," Science **336**, 1137–1139 (2012).

[39]J. Graf, C. Jozwiak, C. L. Smallwood, H. Eisaki, R. A. Kaindl, D.-H. Lee, and A. Lanzara, "Nodal quasiparticle meltdown in ultrahigh-resolution pump-probe angle-resolved photoemission," Nature Physics **7**, 805–809 (2011).

[40]M. Sentef, A. F. Kemper, B. Moritz, J. K. Freericks, Z.-X. Shen, and T. P. Devereaux, "Examining electron-boson coupling using time-resolved spectroscopy," Physical Review X **3**, 041033 (2013).

[41]J. K. Freericks, H. R. Krishnamurthy, and T. Pruschke, "Theoretical description of time-resolved photoemission spectroscopy: application to pump-probe experiments," Physical Review Letters **102**, 136401 (2009).

[42]M. Eckstein and M. Kollar, "Theory of time-resolved optical spectroscopy on correlated electron systems," Physical Review B **78**, 205199 (2008).

[43]M. Eckstein and M. Kollar, "Measuring correlated electron dynamics with time-resolved photoemission spectroscopy," Physical Review B **78**, 245113 (2008).

[44]A. F. Kemper, M. A. Sentef, B. Moritz, T. P. Devereaux, and J. K. Freericks, "Review of the theoretical description of time-resolved angle-resolved photoemission spectroscopy in electron-phonon mediated superconductors," arXiv:1609.00087 [cond-mat] (2016).

[45]P. B. Littlewood and C. M. Varma, "Amplitude collective modes in superconductors and their coupling to charge-density waves," Physical Review B **26**, 4883–4893 (1982).

[46]R. Matsunaga, N. Tsuji, H. Fujita, A. Sugioka, K. Makise, Y. Uzawa, H. Terai, Z. Wang, H. Aoki, and R. Shimano, "Light-induced collective pseudospin precession resonating with higgs mode in a superconductor," Science **345**, 1145–1149 (2014).

[47]M.-A. Méasson, Y. Gallais, M. Cazayous, B. Clair, P. Rodière, L. Cario, and A. Sacuto, "Amplitude higgs mode in the $2H-NbSe_2$ superconductor," Physical Review B **89**, 060503 (2014).

[48]R. Matsunaga, Y. I. Hamada, K. Makise, Y. Uzawa, H. Terai, Z. Wang, and R. Shimano, "Higgs amplitude mode in the BCS superconductors $Nb_{1-x}Ti_xN$ induced by terahertz pulse excitation," Physical Review Letters **111** (2013) 10.1103/PhysRevLett.111.057002.

[49]I. Bloch, J. Dalibard, and W. Zwerger, "Many-body physics with ultracold gases," Reviews of Modern Physics **80**, 885–964 (2008).

[50]S. Giorgini, L. P. Pitaevskii, and S. Stringari, "Theory of ultracold atomic fermi gases," Reviews of Modern Physics **80**, 1215–1274 (2008).

[51]T. Langen, R. Geiger, and J. Schmiedmayer, "Ultracold atoms out of equilibrium," Annual Review of Condensed Matter Physics **6**, 201–217 (2015).

[52]A. F. Volkov and S. M. Kogan, "Collisionless relaxation of the energy gap in superconductors," Soviet Journal of Experimental and Theoretical Physics **38**, 1018 (1974).

[53]R. A. Barankov, L. S. Levitov, and B. Z. Spivak, "Collective rabi oscillations and solitons in a time-dependent BCS pairing problem," Physical Review Letters **93**, 160401 (2004).

[54]E. A. Yuzbashyan, B. L. Altshuler, V. B. Kuznetsov, and V. Z. Enolskii, "Nonequilibrium cooper pairing in the nonadiabatic regime," Physical Review B **72**, 220503 (2005).

[55]R. A. Barankov and L. S. Levitov, "Synchronization in the BCS pairing dynamics as a critical phenomenon," Physical Review Letters **96**, 230403 (2006).

[56]E. A. Yuzbashyan and M. Dzero, "Dynamical vanishing of the order parameter in a fermionic condensate," Physical Review Letters **96**, 230404 (2006).

[57]M. S. Foster, V. Gurarie, M. Dzero, and E. A. Yuzbashyan, "Quench-induced floquet topological p -wave superfluids," Physical Review Letters **113**, 076403 (2014).

[58]I. Marquette and J. Links, "Integrability of an extended -wave pairing hamiltonian," Nuclear Physics B **866**, 378–390 (2013).

[59]N. Tsuji, M. Eckstein, and P. Werner, "Nonthermal antiferromagnetic order and nonequilibrium criticality in the hubbard model," Physical Review Letters **110**, 136404 (2013).

[60]R. W. Richardson, "A restricted class of exact eigenstates of the pairing-force hamiltonian," physics letters **3**, 277–279 (1963).

[61]J. von Delft and R. Poghossian, "Algebraic bethe ansatz for a discrete-state BCS pairing model," Physical Review B **66**, 134502 (2002).

[62]A. Faribault, P. Calabrese, and J.-S. Caux, "Bethe ansatz approach to quench dynamics in the richardson model," Journal of Mathematical Physics **50**, 095212 (2009).

[63]M. Hashimoto, I. M. Vishik, R.-H. He, T. P. Devereaux, and Z.-X. Shen, "Energy gaps in high-transition-temperature cuprate superconductors," Nature Physics **10**, 483–495 (2014).

[64]P. W. Anderson, "Random-phase approximation in the theory of superconductivity," Physical Review **112**, 1900–1916 (1958).

[65]F. Peronaci, M. Schiró, and M. Capone, "Transient dynamics of d -wave superconductors after a sudden excitation," Physical Review Letters **115**, 257001 (2015).

[66]J. C. Campuzano, H. Ding, M. R. Norman, M. Randeira, A. F. Bellman, T. Yokoya, T. Takahashi, H. Katayama-Yoshida, T. Mochiku, and K. Kadowaki, "Direct observation of particle-hole mixing in the superconducting state by angle-resolved photoemission," Physical Review B **53**, R14737–R14740 (1996).

[67]C. L. Smallwood, W. Zhang, T. L. Miller, C. Jozwiak, H. Eisaki, D.-H. Lee, and A. Lanzara, "Time- and momentum-resolved gap dynamics in $Bi_2Sr_2CaCu_2O_{8+\delta}$," Physical Review B **89**, 115126 (2014).

[68]W. Metzner and D. Vollhardt, "Correlated lattice fermions in $d = \infty$ dimensions," Physical Review Letters **62**, 324–327 (1989).

[69]A. Georges, G. Kotliar, W. Krauth, and M. J. Rozenberg, "Dynamical mean-field theory of strongly correlated fermion systems and the limit of infinite dimensions," Reviews of Modern Physics **68**, 13 (1996).

[70]H. Aoki, N. Tsuji, M. Eckstein, M. Kollar, T. Oka, and P. Werner, "Nonequilibrium dynamical mean-field theory and its applications," Reviews of Modern Physics **86**, 779–837 (2014).

[71]L. V. Keldysh, "Diagram technique for nonequilibrium processes," Sov. Phys. JETP **20**, 1018–1026 (1965).

[72]J. Schwinger, "Brownian motion of a quantum oscillator," Journal of Mathematical Physics **2**, 407–432 (1961).

[73]G. Stefanucci and R. v. Leeuwen, *Nonequilibrium many-body theory of quantum systems: a modern introduction* (Cambridge University Press, Mar. 7, 2013), 620 pp.

[74]N. Tsuji and P. Werner, "Nonequilibrium dynamical mean-field theory based on weak-coupling perturbation expansions: application to dynamical symmetry breaking in the hubbard model," Physical Review B **88**, 165115 (2013).